Molecular Mapping of the Binding Sites of a $Na_v1.1$ Activator

Héctor Botella

AALBORG UNIVERSITY
DENMARK

Thesis submitted	07 - 09 - 2018
Internal Thesis supervisor	Prof. Dr. Meg Duroux, Aalborg University
External Thesis supervisor	Dr. Tau Benned-Jensen, Lundbeck A/S
Thesis committee	Prof. Dr. Sebastian Frische Prof. Dr. Meg Duroux, Aalborg University Dr. Tau Benned-Jensen, Lundbeck A/S
Thesis Series	Aalborg University 9220 Aalborg Ø, Aalborg, Denmark Faculty of Medicine, Aalborg University Niels Jernes Vej 10 | DK - 9220 Aalborg Ø Phone: +45 9940 9940 | sund@adm.aau.dk School of Medicine and Health Niels Jernes Vej 12, A5 | 9220 Aalborg Ø | Aalborg, Denmark Department of Health, Science and Technology Aalborg University | Fredrik Bajers Vej 7 D2 | DK-9220, Aalborg Ø
Published in	Aalborg University Publication Repository (vbn.aau.dk)

Printed in Aalborg, Denmark, 2018

Nº of pages 95

I. INDEX OF CONTENTS

II. PREFACE

This report represents the work completed during the Master's Thesis project in the *Medicine with Industrial Specialization in Biomedicine* programme by Aalborg University, and developed at the Signal Transduction research unit in Lundbeck A/S, Copenhagen, from August 2017 to September 2018.

Such Thesis culminates with a year of intense work through multiple disciplines spanning molecular genetics, cell biology, microscopy, bioinformatics and electrophysiology. It has been utterly interesting to experience by first-hand what first seemed to be individual techniques in diverse areas, ultimately converging to create a complete scientific framework that serves to explain and confirm the findings discovered.

The challenge posed by the ambitious project objectives has undoubtedly made me learn an incommensurable amount of knowledge, pushing me to strive to pursue answers and resolve issues, and provide me with the fruition necessary to venture further into the world of science for many years to come.

However, this work has only been possible thanks to the help and dedication of many people, with which the number of techniques employed, and the understanding required to utilize them, could not have been achieved by myself alone. The important aid in cloning by Lab. Tech. Annette Bjørn, evidences that calm and perseverance is fundamental for the simplest experiments which are prone to fail despite many attempts and previous successes. I want to thank technicians Anders C. Larssen and Kirsten Olesen for guiding me during my first steps into a real corporative laboratory, for helping me finding the materials needed and even finding myself around a mess. I thank the help of technicians Charlotte F. Hundahl and Claus Black in providing me with the best cells and advice for cultures at any time. The knowledge of postdocs Camilla S. Jensen and Anders Sonne that proved invaluable in critical moments facing intricate laboratory equipment. The temperance of Sr. Scient. Steffen Nyegaard, when introducing me to spinning disk confocal microscopy and his trust in letting me manipulate such valuable machinery. The curiosity of Sr. Bioinformatician Laurent David when dealing with new unseen molecular structures and his detailed insights about their analysis. The personal help of PhD and MSc students Maitane Caballero, Henrik Hertz, Yasmine Iacone, Ugne Sabaliauskaite and Christina Da Graça in moments of despair, angst, low confidence – and physical impairment. The mere presence of many other cheerful and dedicated scientists in Lundbeck, where mutual cooperation leads to the best workplace for research that I have ever been a part of. My utmost thanks to Sr. Tech. Charlotte Hougaard for bestowing me with the art of electrophysiology, a true invaluable gift for my future career, and for her full-time dedication. To my supervisor and Prof. Meg Duroux for her continued support and for making me realize of my best qualities – with still a long path for me to travel down. And finally, to my supervisor and Dr. Tau Benned-Jensen, to whom there are not enough words with which can I express my sincerest of gratitudes for awarding me with my long-awaited dream of reaching the big leagues in the pharmaceutical industry. No other supervisors, anywhere, could have supported me so thoroughly, and made me feel this useful and cherished. Thank you.

Héctor Botella
Copenhagen, September 7th, 2018

III. ABSTRACT

Schizophrenia constitutes one of the most complex psychiatric diseases whose environmental and genetic etiology make difficult to treat. The diverse pathologic targets implied, and an extreme genotypic variability in patients considerably reduce treatment efficacy. A continuous search for newer drugs is ongoing, as current pharmacological treatments fail to address broad cohorts of patients and, in the best of cases, only partly ameliorate the psychotic symptoms[1,2].

Latter research has set the focus on the role of interneurons in the regulation of neural networks and their significance in seizure episodes of several epilepsies[3,4]. The parvalbumin-positive (PV^+), GABAergic fast-spiking interneurons (FSINs) send inhibitory inputs to regulate the general excitatory output in a brain region [5,6]. Abundantly found on the axon initial segment (AIS) of these FSINs[7], the voltage-gated sodium channel (VGSC) $Na_v1.1$ has become an attractive target to use to potentiate their inhibitory effect over de-coordinated brain regions[8].

The newly discovered $Na_v1.1$-specific Lundbeck modulator AA43279[9] binds to a yet-to-be discovered region in said channel. This project attempted to trace its exact mode of action by exchanging entire structural domains between VGSCs, and examining whether its effects vary along with the presence or absence of said channel subunits in the resulting whole chimeric constructs. But despite the majority of split Na_v domains with tagged sfGFP were not functional, this strategy succeeded with simpler $K_v2.1$ monomers and may hold promising results when applied to other VGICs or LGICs, to allow their modification at a subunit-level and the analysis of their live functionalization *in situ*.

Keywords: schizophrenia, FSIN, PV, $Na_v1.1$, $Na_v1.4$, $K_v2.1$, chimera, split ion channel, sfGFP, domain dimers, modular approach

IV. LIST OF ABBREVIATIONS

A – Ampere
AAV – Adeno-associated virus
ACh – Acetylcholine
AIS – Axon initial segment
AmpR – Ampicillin-resistant
AP – Action potential
AUC – Area under the curve
APC – Automated patch-clamp
BBB -Blood-brain barrier
BLAST – Basic Local Alignment Search Tool
bp – Base pair
BSA - Bovine serum albumin
cDNA - coding Deoxyribonucleic acid
CD – Cluster of differentiation
CDS – Coding sequence
CNS – Central nervous system
CSF – Cerebrospinal fluid
C(t) – C-terminal end
D1-D4/DI-DIV – Domain (1-4)
Da - Dalton
DC – Dendritic cell
DIC – Differential interference contrast
DMEM – Dulbecco's Modified Eagle's medium
DMSO - Dimethyl sulfoxide
DNA – Deoxyribonucleic acid
dNTP – Deoxynucleotide triphosphate
DS – Dravet Syndrome
EC – Endogenous current
EDTA - Ethylenediaminetetraacetic acid
EEG – Electroencephalogram
eGFP – enhanced Green fluorescent protein
ER – Endoplasmic reticulum
F – Faraday
FBS – Fetal Bovine Serum
Fig. – Figure
FP – Fluorescent protein
FRET – Fluorescence Resonance Energy Transfer
FSIN – Fast-spiking interneuron
G_{xx} – $Conductance_{ion}$
GABA – Gamma-aminobutyric acid
GBO – Gamma band oscillation
gDNA - genomic Deoxyribonucleic acid
GFP - Green fluorescent protein
GHK – Goldman–Hodgkin–Katz
HEK – Human embryonic kidney cell
I_{xx} – $Intensity_{ion}$
IN – Interneuron
I/t – Intensity/time relation
I/V – Intensity/Voltage relation
KanR – Kanamycin-resistant
L - Liter
LGIC - Ligand-gated ion channel
M – Molar
mAChR – muscarinic acetylcholine receptor
MCS – Multiple cloning site
MPC – Manual patch-clamp
MPI - Maximum peak intensity
mRNA – messenger Ribonucleic acid
nAChR – nicotinic acetylcholine receptor
NMDAR – N-methyl D-aspartate receptor
nt – Nucleotide
N(t) – N-terminal end
P1-P4 – Pore (1-4)
PV^+ - Parvalbumin-positive
Pyr – Pyramidal neuron
PLL - Poly-L-Lysine
PBS – Phosphate buffer saline
PCR – Polymerase chain reaction
PFD – Pore-forming domain
PNS – Peripheral nervous system
P/S – Penicillin / Streptomycin
qPCR – quantitative Polymerase chain reaction
RFP - Red fluorescent protein
RNA - Ribonucleic acid
RT – Room temperature
RUs – Relative units
S1-S6 – Segment (1-6)
ScTx- Scorpion toxin
SD – Standard deviation
sfFP – superfolded Fluorescent protein
sfGFP – superfolded Green fluorescent protein
SSA – Steady-state activation
SSI – Steady-state inactivation
SST/SOM – Somatostatin
STX - Saxitoxin
SZ – Schizophrenia
TM – Transmembrane
TTX – Tetrodotoxin
V – Volt
VGIC - Voltage-gated ion channel
VGKC – Voltage-gated potassium channel
VGSC – Voltage-gated sodium channel
VIP – Vasointestinal peptide
VSD – Voltage-sensing domain
V/t – Voltage/time relation
Å – Ångstrom

h/m/r/ee/sp/w/co/ch **Na_v/K_v** – human/mouse/rat/eel/ split/whole/combinated/chimeric **Na_v/K_v** channel

1. INTRODUCTION

1.1. - The nervous system

The nervous system is comprised of the ensemble of organs, tissues and cells transmitting the electrical signals that coordinate the organism's actions, detect the body and environmental stimuli, and modulate the organism's responses and behavior. This system is divided into the Central Nervous System (CNS) and Peripheral Nervous System (PNS) in vertebrates. The first includes the brain and spinal cord, the two main organs implicated in integrating the whole organism's information in the form of these electrical signals it can receive from, modulate and send back to. The latter includes the body's set of ganglionic and nerve tissues, and motor neurons spanning through the rest of the body outside the CNS and serving as a connection between both parts for receiving sensatory information and performing motor actions (*fig. 1*).

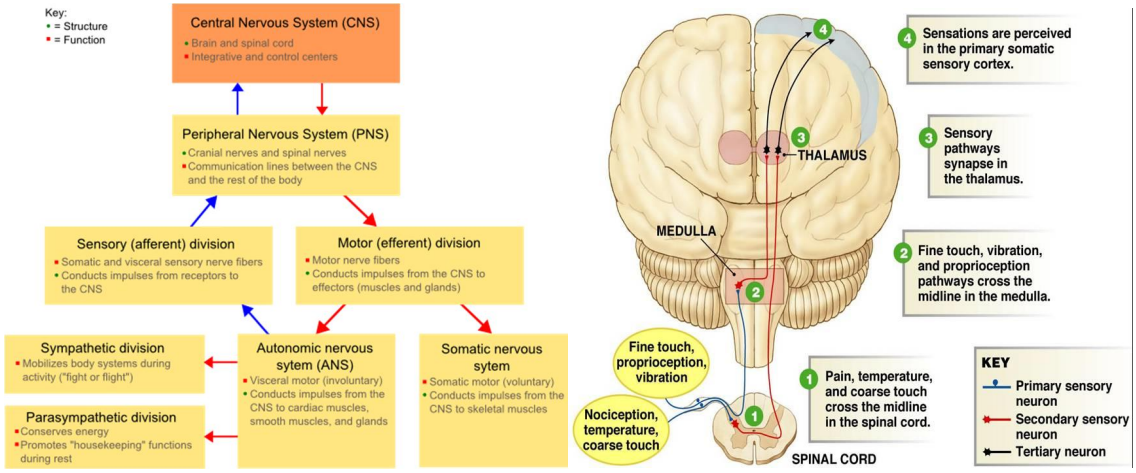

Fig. 1: divisions of the nervous system in vertebrates (left) and schematic of a somatosensory pathway (right) (© GNU)

At a cellular level, both CNS and PNS are mainly comprised of neurons and nerves, the latter being bundled axons from the neurons. The set of nerves and neurons receiving sensory information from the body and environment belong to the afferent division, and convey these signal inputs upstream to the brain and spinal cord. In turn, the efferent division drives electrical stimuli downstream from the brain and spinal cord into the rest of the body for it to perform its actions. A third, smaller division harbors just the interneurons, characteristic cells in their short axonal projections and in that they only intervene closely in the local aspects of a neural circuit, by acting as input relays of these stimuli and regulating their electrical output[4].

1.2. - The CNS

The cranial cavity and the spinal canal respectively house the brain and the spinal cord, with the 3-layer meninges engulfing both organs. At a histological level, two distinct components are observed within the CNS: the grey matter and the white matter. The grey matter is majorly comprised of the neurons' soma (the cell body), neuropil (unmyelinated axons and dendrites) and glial cells (where astrocytes, oligodendrocytes and microglia are found). Brain regions with grey

matter are frequently involved in memory, vision, audition, speech, and motion control among others, while the spinal cord's grey matter contains efferent motor neurons and sensory afferent neurons, respectively located in the anterior and posterior grey column. The white matter is formed of myelinated axons and its bundled structures, the nerve tracts. It has a defined function for the transmission of the electrical impulses across the CNS (*fig. 2*).

Fig. 2: grey matter areas of cells and white matter fibers in cross-sections of brain (left) and spinal cord (right)

1.3. - The brain

The brain is the principal integratory organ of the nervous system. It receives and interprets the ensemble of stimulatory signals from the body, generates the current patterns to control body actions, while also producing the hormones and neurotransmitters to modulate itself and the rest of organs and tissues. It is located in the head of vertebrates and many invertebrates, and protected by the cranium and the meninges layers. The brain is also responsible for learning, cognition, and the abilities of speech, reasoning and self-awareness in humans.

The parts of the brain are structurally divided, namely into the cerebrum, cerebellum and brainstem. An expanded 6-category classification includes the telencephalon or cerebrum (comprising both brain hemispheres), diencephalon (harboring the thalamus and hypothalamus), the cerebellum, pons, and the medulla oblongata (*fig. 3*).

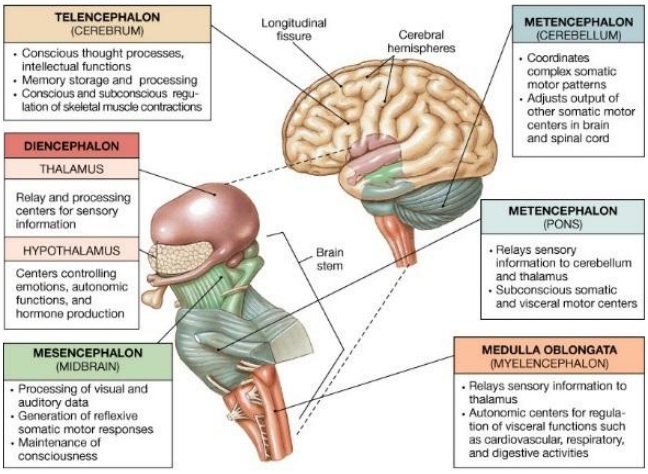

Fig. 3: subdivisions of the brain structure (© GNU)

Apart from neurons, the brain hosts other cell populations classified as glial cells, or (neuro)glia, where astrocytes, oligodendrocytes and microglia cell types are found (section *1.6. Other types of neural cells*).

1.4. - The neurons

Nerve cells, or neurons, are specialized excitable cells with ability to receive, send and modulate electrochemical impulses for intercellular signaling, excitation and inhibition of other cell types. They constitute the principal cell population in both the CNS and PNS, connecting each other via synapses and forming neural networks for triggering the initiation of further electrical impulses.

The cellular structure of a neuron features the soma – the main and central body of the cell – one or multiple dendrites, and a single axon, the latter two being able to branch into secondary or tertiary projections (*fig. 4*). The soma exclusively houses the neuron's nucleus, besides of sharing the rest of the expression machinery, lisosomes and vesicular trafficking system with the other cell parts. The dendrites and axons respectively drive the excitatory inputs and outputs through their membranes from presynaptic and to postsynaptic neurons, and share some of the subcellular organelles (cytoskeleton, ribosomes, mitochondria…) with the soma.

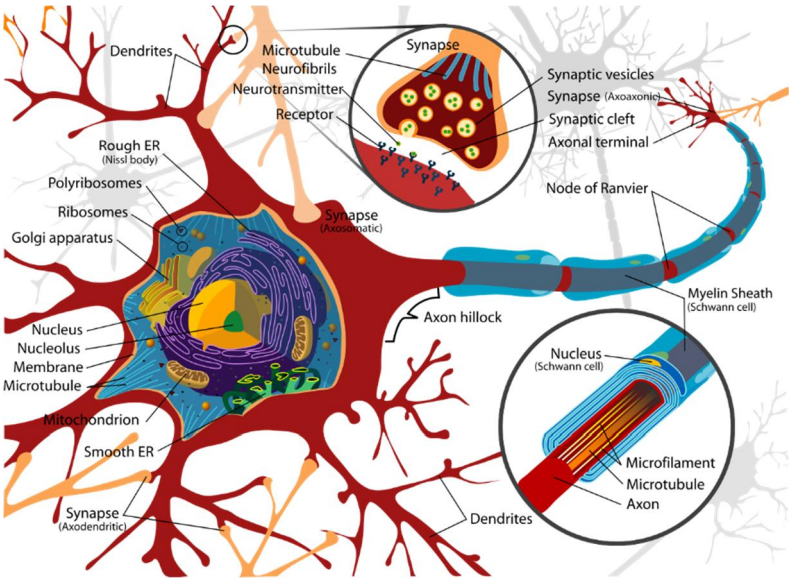

Fig. 4: diagram of a nerve cell and its subcellular components (© GNU)

Stimuli are first received in the dendrites and transduced into action potentials (section *1.8. Action potentials*) that will travel along the neuron's membranes towards the soma, where they will together converge and trigger the activation of further ion channels present. The magnitude of the joint electrical impulse can either be sufficient for the axon to produce a downstream stimulus into other neurons, or below the threshold for the axon initial segment (AIS) to trigger an action potential. Thus, neurons are sometimes referred to as "polarized" cells in this paradigm of unidirectional dendrites-soma-axon impulses.

Classification of neuron types is complex depending on the function and context they can be sorted into. Neurons can be classified based on their neurite extensions (bipolar, multipolar, unipolar…), the neurotransmitter type released from presynaptic terminals (glutamatergic, cholinergic, GABAergic…), their somatosensory division (primary, secondary and tertiary), location (cortical, thalamic…) or functionality (sensory and motor neurons, interneurons).

1.4.1. - Interneurons

Interneurons, or relay neurons, are a subtype of inhibitory neurons that project their short axon terminals onto nearby excitatory cells to regulate their excitability and action potential firing. They are characteristic in that they do not span over different brain areas but are limited to a single one, mainly integrative sensory centers (*fig. 5, left*). They utilize GABA as the principal inhibitory neurotransmitter, which is released from presynaptic vesicles and binds to postsynaptic ionotropic GABA channels permeable to chlorine. This Cl^- influx into the targeted neuron ultimately makes the membrane potential more hyperpolarized, thus dropping the threshold for action potential generation (section *1.8. Action potentials*) and resulting in a reduced neural activity[10]. In addition, spinal cord interneurons also release glycine as neurotransmitter, while the ones found in cortical and basal ganglia can secrete a wide variety of neuropeptides.

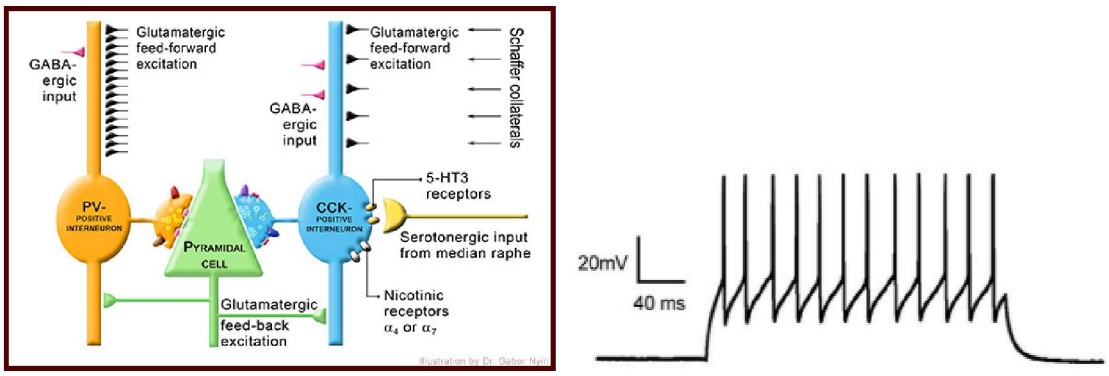

Fig. 5. Left: simplified interneuron connections in brain (orange and blue) (© GNU). Right: example of an action potential train fired by FSINs (from *von Schoubye et al. (2018)* [53])

Overall, the innervation from an interneuron towards a single excitatory neuron results in the regulation of larger cell clusters these neurons project to. Consequently, the functional characteristics of interneurons usually consist in coordinating gating inputs of excitatory cell populations, synchronizing their action potential firing, and generating rhythmic activity patterns in a brain area. It is not casual either that interneuron function is related to a correct synaptic efficiency, plasticity, and memory[11].

In turn, existing interneuron subclasses can be classified depending on their morphology and different cell markers expressed. Cortical, GABAergic interneurons comprise 3 types being positive for either parvalbumin (PV) – a membrane Ca^{2+}-binding protein –, somatostatin (SST/SOM) – a growth hormone inhibitor and neuropeptide – or the serotonin receptor (5HT3a)[12]. The PV^+ interneurons signature feature is the firing of fast-spiking, non-adapting trains of action potentials (*fig. 5, right*). They include basket and chandelier cells, and express certain molecular markers like calbindin, substance P, and ion channels $K_v3.2$, $K_{erg}1$, and $Na_v1.1$ in high

amount. SST^+ neurons show regular-adapting firing patterns, may or not express calretinin, and include Martinotti cells with their arborizing morphology. Finally, $5HT3a^+$ cells include neurons either positive and negative for vasointestinal peptide (VIP^+ and VIP^-) and are irregularly-spiking[13].

Hippocampal fast-spiking interneurons (FSINs), GABAergic, and positive for parvalbumin (PV^+) are an important cell subset of research for diverse neural diseases in which synaptic transmission is abnormal such as epilepsies, psychosis, convulsions, and schizophrenia (section *1.5.1. Schizophrenia*). In addition, these neurons are particularly enriched in the $Na_v1.1$ sodium channel[14, 15, 16] (*1.9.2.1. $Na_v1.1$*), which is the key target of this research project and for AA43279, a $Na_v1.1$-selective activator[9] (*1.9.2.bis Activators and inactivators*).

1.5. - Diseases of the CNS

1.5.1. - Schizophrenia

Schizophrenia is a psychiatric disease derived from a deregulation in the integrative signals between brain areas controlling cognition, emotions and thoughts. In this condition - under which other related mental illnesses like epilepsy and bipolar disorder fall - patients not only experience cognitive and negative behavioral symptoms but positive symptoms as well. The first kind may include lack of attention, concentration, emotional expression or motivation, and are considered as a loss of function in regards to healthy individuals. The second type comprises the overexpression of normal mental functions ending up in sensory hallucinations, delusions, and speech and thought disorder[1, 2].

The exact mechanisms underlying the pathophysiological events in SZ are not currently established but rather based on hypotheses. An overexpressed activity in dopaminergic neurons was first postulated upon the observation that antipsychotics inhibiting D2 receptors (haloperidol, aripiprazole) diminished the psychotic symptoms in schizophrenia[17, 18]. Oppositely, the pharmacological activation of underfunctional D1 receptors could improve the negative symptoms in SZ. However, further evidence is required to support this framework as the anti-psychotic efficacy is not consistent among all patients. The glutamatergic hypothesis postulates that a reduced NMDAR and GAD67 expression and subsequent lowered neuronal glutamate-mediated activity observed in SZ patients, is responsible for some cognitive deficits described, but current medications are unable to restore all symptoms either[19, 20, 21].

Among several other postulates[22], a newly emerged hypothesis is that of interneuron impairment – an area under intense investigation which also constitutes the basis for this project. The hyperactivity of excitatory pyramidal neurons (Pyr) in the hippocampal CA1 and CA3 brain layers among others, which has been linked to some of the psychotic symptoms in schizophrenia, can be modulated by the inhibitory interneurons they are innervated with[23, 24, 25]. Specifically, these parvalbumin-positive (PV^+), fast-spiking interneurons (FSINs) are enriched in $Na_v1.1$ sodium channels sending action potentials for axonal vesicular release of GABA, an inhibitory neurotransmitter ultimately binding to $GABA_A$ ionotropic receptors in the dendritic terminals of Pyr's and regulating their correct excitability. The need for an enhanced activation of $Na_v1.1$

channels and following augmented inhibitory activity of FSINs may be brought along with the application of AA43279[9], a recently discovered compound highly selective for this sodium channel (*see section 1.9.2.bis Activators and inhibitors*).

EEG analyses are often used to find abnormal band oscillations from brain layers that ultimately result in the de-synchronized communication processes leading to epilepsies. Schizophrenic patients manifest an increase in gamma band oscillations (GBOs) evoked without stimuli[26]. GBOs are the fraction of neural waves measured between the 30-100 Hz range, and hypothetically responsible for learning, cognitive development, self-consciousness and perception. Moreover, gamma waves play a fundamental integrative role in unifying and cohering communicative signals between brain regions. The correlation that GABAergic PV^+ FSINs fire accordingly to GBO production[27], suggests whether a specific therapy enhancing the interneuronal inhibition could restore the gamma patterns.

1.5.2. - Dravet Syndrome (SMEI)

Dravet Syndrome, formerly known as severe myoclonic epilepsy of infancy, is a type of epilepsy resulting from the loss of function in $Na_v1.1$, with sometimes $Na_v1.2$ also affected[28, 29, 30]. It is considered one of the most severe types of epilepsy known and it usually has its appearance between the first 6-12 months of life, spanning lifelong. Mortality rates account for almost 60% and surviving individuals are prone to suffer frequent diverse seizures, along with cognitive and psychomotor deteriorations causally derived from this encephalopathy[31]. Myoclonia and other convulsory statuses outside epileptic episodes are also common.

Up to 80% of cases of DS can be traced to *de novo* point mutations affecting the *SCN1A* gene in one allele copy, resulting in haploinsufficiency of $Na_v1.1$. Genotypical variability is elevated, accounting for a total of 338 different mutations distributed in exonic (291), intronic (29) and other genomic (18) locations. These mostly include missense (164), frameshift (64) and stop (56) mutations (*fig. 6*) that ultimately produce either a truncated or non-functional version of $Na_v1.1$ [30].

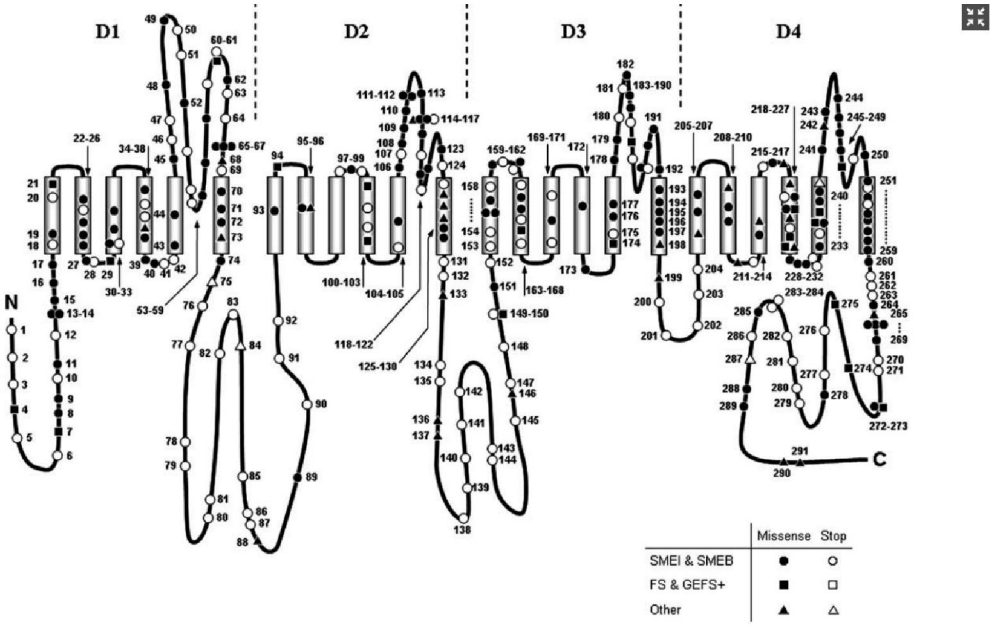

Fig. 6: a catalog of $Na_v1.1$ mutations arrayed over its secondary structure (from *Lossin, C. (2009)* [30])

The onset of this disease can be first triggered by high body temperature, and thereafter reappear without being further fever-induced. Despite the mechanistic characteristics may resemble of other epilepsies (as detected in EEGs), the pathophysiological cause resides more precisely on the lack of inhibitory stimuli in the GABAergic interneurons, responsible for the coordination of their innervated excitatory neurons. This directly correlates with $Na_v1.1$'s loss-of-function and has close ties with the interneuron hypothesis in schizophrenia (section *1.5.1.*).

Dravet Syndrome also constitutes one of the most pharmacologically-resisting types of epilepsy (or "refractory epilepsy"). The development of drugs to rescue this haploinsufficient phenotype includes the recently marketed stiripentol with GABAergic activity. Otherwise, the search for $Na_v1.1$-specific activators has recently discovered the Hm1a spider peptide provokes the delay of the fast-inactivation phase of $Na_v1.1$ thereby causing its enhanced activity and persistent current[32]. A pre-clinical assessment of the effects of AA43279 - which shares the same mode of action - in models of DS would be likewise interesting from a biomedical point of view.

1.6. - Other types of neural cells: the glia

As mentioned above, other cellular types form the CNS and can be found in a 3:1 proportion regarding neurons. The neuroglia has a fundamental supporting function for neurons, as of maintaining the homeostasis of the neuronal chemical environment they are in, scaffolding their neural projections, modulating the action potential propagation by dendritic and axonal contacts, regulating the neurotransmitter uptake at synapses, and aiding in neural recycling and injury[33].

Astrocytes support the blood-brain barrier (BBB) and maintain the ionic milieu around neurons, by physically establishing contact and engulfing all the neuron projections and synapses. Oligodendrocytes do likewise make contact with some neurons by wrapping their myelinated

membrane around axons to provide enhanced action potential transmission: these are called Schwann cells if found in the PNS. Microglia, with high similarities to macrophage cells, can secrete cytokines to promote survival, inflammation or apoptosis in cases of injury, and scavenge the neural debris (*fig. 7*). Ependymal cells form the neuroepithelial lining separating brain cavities and produce cerebrospinal fluid (CSF). Finally, the glial stem cells found can give rise to oligodendroglial and astrocyte precursors, the latter being of biomedical significance as of being able to differentiate into neurons.

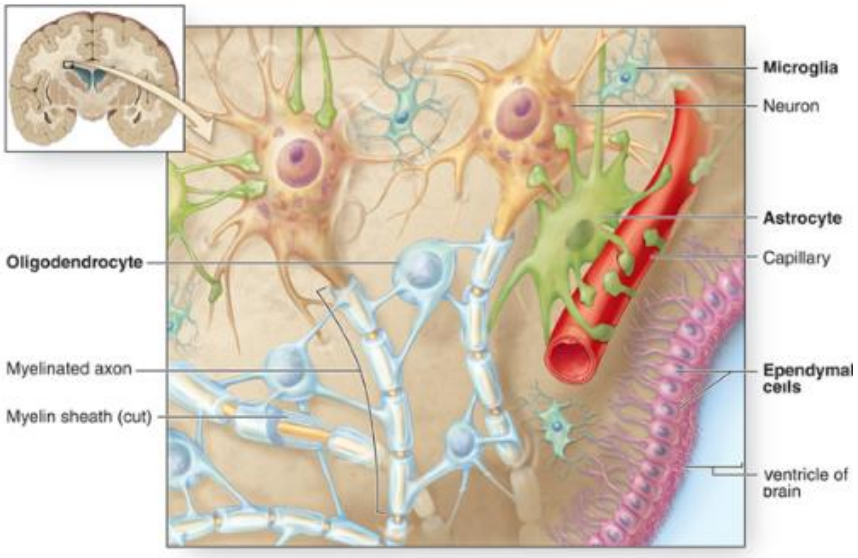

Fig. 7: depiction of the major types of glial cells found in the CNS (© McGraw-Hll)

1.7. - Neuronal synapses

A requirement for the communication between the different parts of the nervous system and body is a close contact that allows propagation of the action potentials between cells. A synapse can be defined as the physical and functional contact in between two neurons formed by the membrane buddings located in the axon of one cell – the presynaptic terminal – and the dendrites of the other – the postsynaptic terminal. Two different synapses are classified depending on the contact type. An electrical synapse has a continuous membrane union between both neuron terminals through gap-junction proteins, thus allowing an uninterrupted transmission of action potentials along them. Chemical synapses, however, present a synaptic cleft between the terminals with no membrane continuity, where neurotransmitters released from presynaptic vesicles in response to an action potential, bind to their cognate receptors on the postsynaptic terminal thus generating new ionic fluxes and electrical signals in the receiving cell (*fig. 8*).

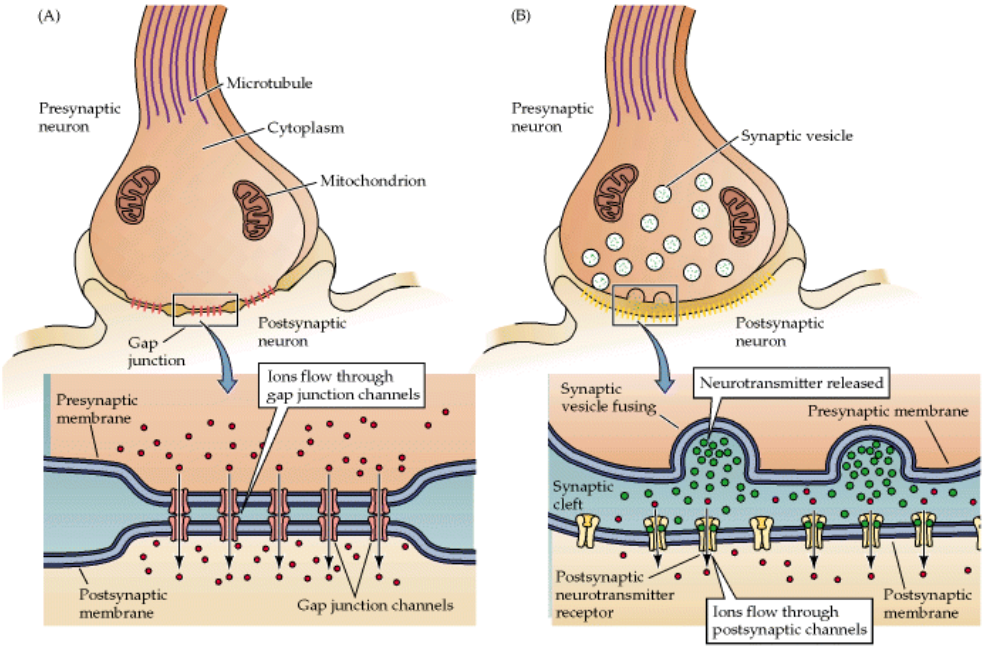

Fig. 8: diagram of an electrical synapse (left), chemical synapse (right), and close-up on the synaptic clefts (bottom) (© Neuroscience, 5th edition)

1.8. - Action potentials

The electrical impulses transmitted among neurons along their axonal extensions are called action potentials. They are created when, in response to a stimulus, ion channels embedded on the cell membrane open to let a selective flow of ions pass through them from the extracellular to the intracellular side (and vice-versa) in accordance with these ions' electrochemical gradient. The sudden change in membrane potential in that location generates an impulse that is transmitted across the axon membrane – the action potential – that is able to open further ion channels and making more currents of its kind (*fig. 9*).

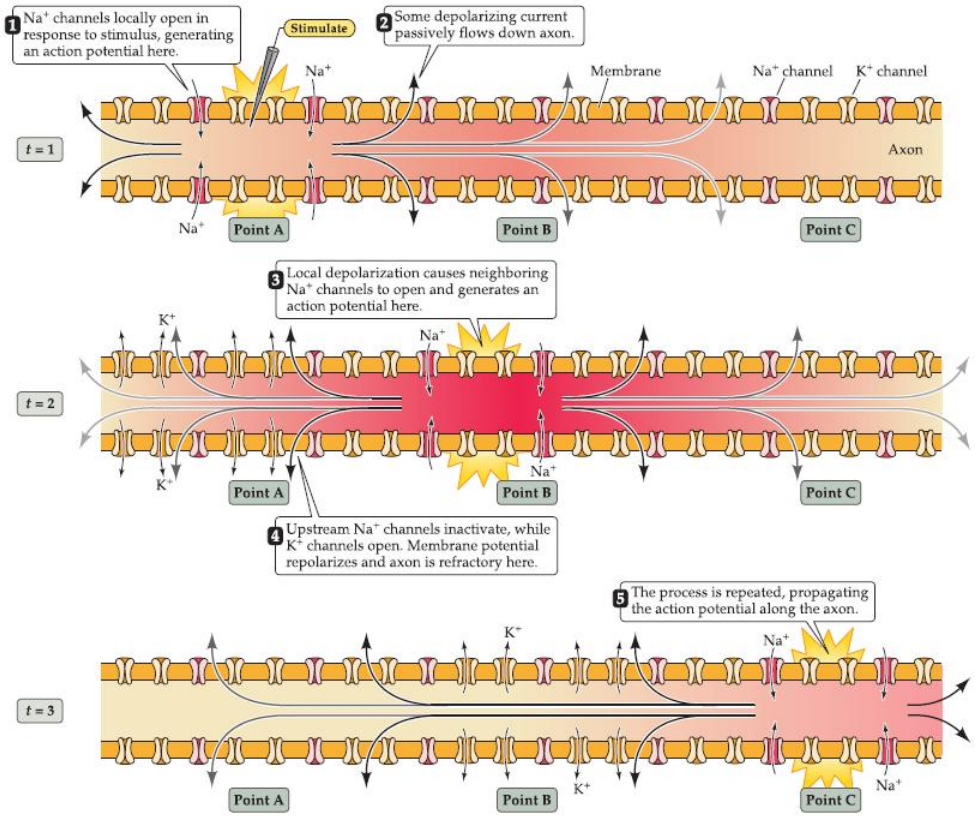

Fig. 9: representation of a continuous and directional action potential triggered in an axon (© Neuroscience, 5th edition)

Sequentially, the complex succession of events underlying the generation of action potentials starts with a stimulus that causes a membrane depolarization, that is, an increase from a negative voltage to positive. If this increase reaches the threshold potential for sodium-selective channels, a conformational change in them occurs whereby Na^+ ions will become permeable and cross the membrane through their open state (*fig. 10*). Na^+ ions follow an inward direction to the cell down the physiological sodium concentration gradient – around 150 mM extracellularly and 5-15 mM intracellularly - and further depolarize the membrane to more positive potentials[34]. This sudden rise in potential activates, in turn, the delayed opening of potassium-selective channels. When the peak of the action potential is reached, Na^+ channels inactivate and instead K^+ channels are fully opened thus allowing the flow of positively charged K^+ ions. These are driven outwards the cell down their concentration gradient likewise (approximately 4 mM outside and 140 mM inside), thereby promoting a decrease in the overall membrane potential known as repolarization. The also delayed inactivation of K^+ channels causes the membrane potential to fall lower than the resting potential in a phase known as hyperpolarization. The duration of this period is called the refractory period, which serves the cell not to initiate subsequent action potentials, thereby recovering the initial ionic concentrations across the membrane thanks to the action of Na^+/K^+ATPases and other ion co-transporter proteins. Once the resting potential is again achieved, the cell is ready to produce further APs.

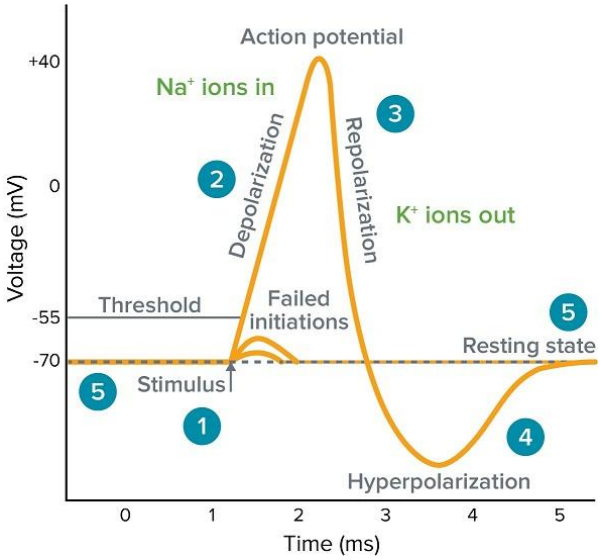

Fig. 10: voltage-time (V/t) representation of an action potential including depolarizing (Na^+-driven), repolarizing and hyperpolarizing (K^+-driven) phases

1.9. - Ion channels

Ion channels are integral transmembrane (TM) proteins whose function is to allow the flow of ions across the plasma membrane through open, polar pores on them. Two main types of ion channels exist: voltage-gated ion channels (VGICs) and ligand-gated ion channels (LGICs). VGICs have voltage-sensitive structures responding to changes in membrane potential for ion conductance, while LGICs depend over chemical ligands binding in the channel cavities (binding sites) to produce the ionic flow. Other identified classes of ion channels sensitive to mechanical stress, light, heat, coldness and pain (nociceptors) rely onto these stimuli for their activation.

The ensemble of a cell's ion channels is responsible for many cellular processes, but VGICs are fundamental in the generation of APs (section *1.8.* above). Other functions attributed to ion channels comprise the maintenance of the cellular volume by the concerted ion exchange between the extracellular space and the cytosol, or the triggering of intracellular signaling cascades mediated by Ca^{2+}.

1.9.1. - Architecture of ion channels

The signature feature of every existing ion channel is the formation of a hydrophilic pore across the membrane lipid bilayer to permit the flow of charged ions between cellular compartments. While nevertheless diverse in their functionality and selectivity for ions, a major common architecture can be identified in ion channels, where extracellular, integral transmembrane, and intracellular domains are noticed (*fig. 11*).

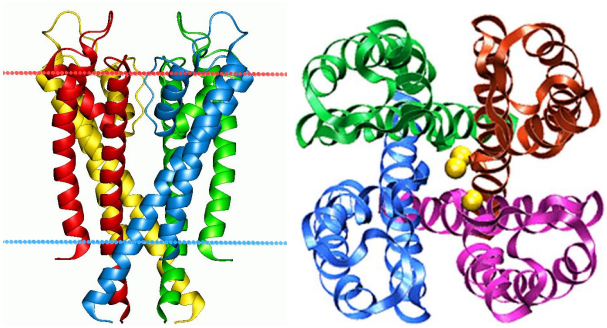

Fig. 11: cartoon representation of the 3D structure of the Kcsa bacterial channel from the side (left) and top (right). The red and blue horizontal lines represent the extent of the transmembrane domain

Predominant secondary structures of alpha-helical domains sterically interact with each other for the correct conformational changes between the closed, open and inactivated states upon stimulation. Residues in their primary structure are neither found randomly, with namely hydrophobic amino acids positioned outwards the channel structure to stabilize with the membrane, and hydrophilic residues pointing inwards forming the pore-forming domain (PFD), voltage-sensing domain (VSD), and the rest of the tertiary structure.

Besides, more complex ion channels can be formed by oligomerization of these homologous tertiary structures deemed as non-functional alpha-subunits *per se*, with the addition of other α-subunit monomers (section *1.9.3. The potassium ion channel family*), and the coupling of accessory, modulatory β-subunits, altogether giving the ion channels an enhanced function and mechanistic complexity.

1.9.2. - The sodium ion channel family

The Na_v family in humans is comprised of 10 alpha isoforms[1] with specific localization throughout human excitable tissues such as the CNS (namely isoforms 1.1, 1.2 and 1.6, also with 1.3 and 1.7), skeletal muscle ($Na_v1.4$), and heart ($Na_v1.5$). Moreover, their presence in non-excitable cell types (astrocytes, microglia, DCs, T-CD4+, macrophages…) has been reported as of contributing to several physiological functions like motility, migration, vesicle acidification, and modulation of other cellular targets[35].

Sodium channels from $Na_v1.1$ to $Na_v1.9$ are all VGICs responsible for the initiation of the action potentials, while the Na_x channel (sometimes referred to as $Na_v2.1$) is a $[Na]_{ext}$-dependent, voltage-sensitive channel implicated in sodium homeostasis[36, 37]. The Na_v subfamily members, while closely related, feature differences in residue sequence ranging from 4% to 25% (*fig. 12*).

[1] Despite this term designates the protein variants coming from alternative splicing of a single gene, authors frequently refer to the Na_v family members as "isoforms"

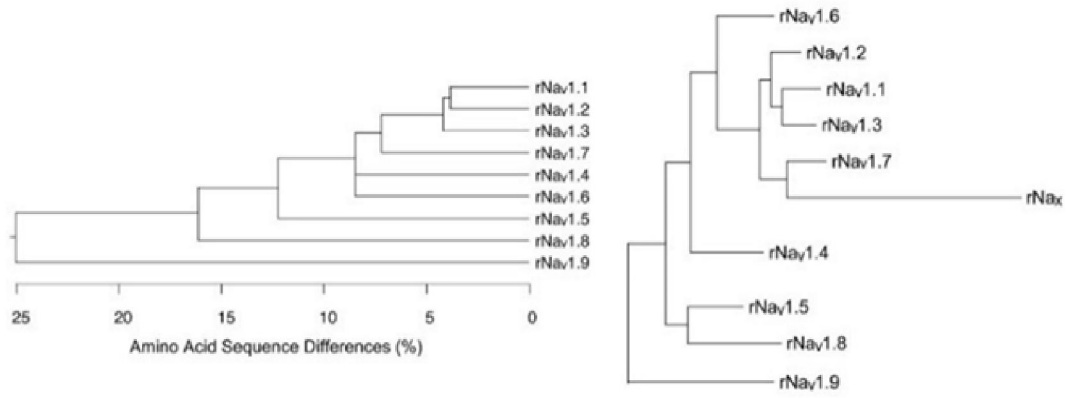

Fig. 12: phylogenetic trees of divergence between Na_v members in residue differences (left) and evolutionary drift in clades (right) (from *Catterall, W. a, Goldin, A. L., & Waxman, S. G. (2005)* [38])

The Na^+ family of VGICs in eukaryotes is characterized by a well-conserved structure of 4 homotetrameric domains (D1-D4), each formed by 6 alpha-helical TM segments (S1-S6), and connected by 3 intracellular loops (*fig. 13*). Common likewise is the location of the VSD in S1-S4, with key Lys and Arg residues in S4 repeatedly placed every 3 positions, and the PFD between segments S5 and S6.

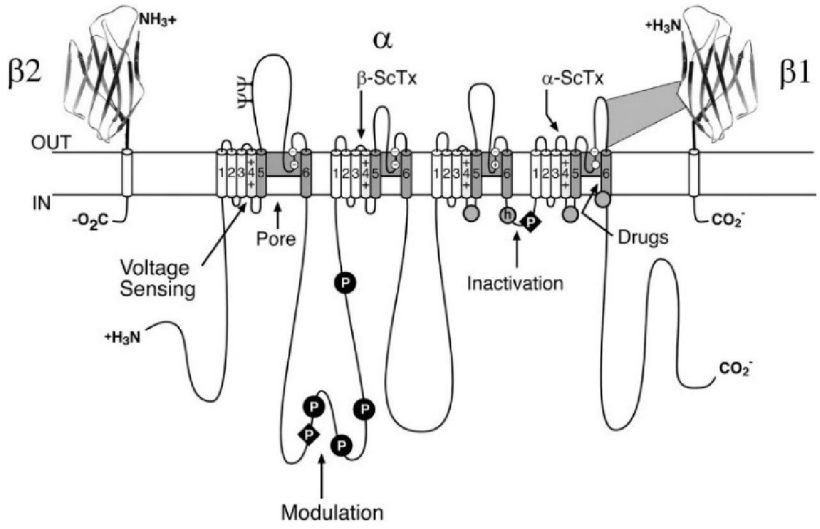

Fig. 13: secondary structure of Na_v channels with common modification and modulation sites, along with β-subunits (from *Catterall, W. a, Goldin, A. L., & Waxman, S. G. (2005)* [38])

Beta-subunits are accessory proteins modulating the voltage dependence and the kinetics between the channel's conformational states, despite they are not essential for channel activity itself[39, 40]. Up to 4 different β-subunits for sodium channels (Na_vβ1-β4), encoded by the *SCN1B* to *SCN4B* genes, are expressed in the CNS, featuring a prominent Ig-like domain in the extracellular space anchored to the cell membrane by an alpha-helical transmembrane domain (*fig. 14*). β-subunits 1 and 3 are non-covalently associated with the α-subunits, while β2 and β4 are bound by disulfide bridges to α[41, 42, 43]. Apart from said functions, beta-subunits serve for channel trafficking and localization, cell adhesion and migration, and may be associated to the onset of epilepsies, arrhythmias, and other excitability pathologies[40].

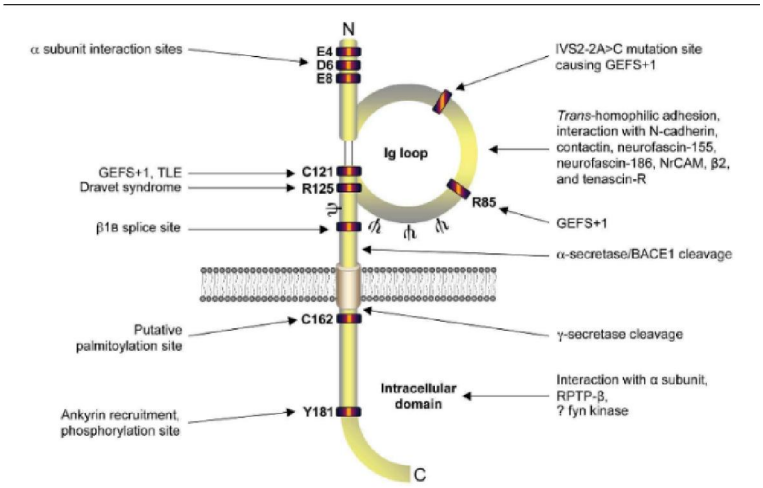

Fig. 14: out-of-scale schematic of a β-subunit of Na_v channels (from *Brackenbury, W. J., & Isom, L. L. (2011)* [40])

A classic sodium current generated by a Na_v VGIC is depicted in *figure 15 below*. If the intensity of the applied depolarizing stimulus is higher than the threshold potential for said channel (*see section 1.8. Action potentials*), a sudden conformational change leads to a shift from the closed to the open state. This fast activation feature is characteristic for VGSCs, where the fast rise in permeabilization to Na^+ further contributes to cell depolarization and is depicted in the first segment of the falling slope below. After this, a brief peak phase precedes the inactivation phase of the sodium current, where the channel undergoes another conformational change leading to the inactivated state. A fast inactivation, despite relatively slower than the activation phase, is also signature for VGSCs thanks to the Ile/Phe/Met motif (IFM)[44, 45], and shown as the rising slope in *fig. 15*. Finally, sodium channels suffer a last conformational change during the hyperpolarization phase of APs, from an inactivated to a closed state where they are ready to be activated again.

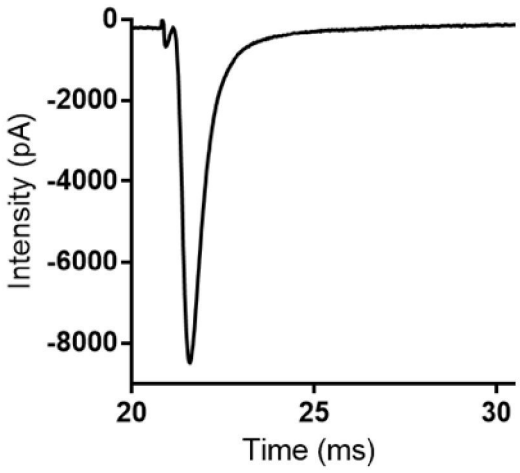

Fig. 15: I/t plot of a Nav1.4-elicited current. Phases from left to right: baseline, artificial transient capacitance, fast activation slope, peak, fast inactivation slope, and recovery to baseline

1.9.2.bis. - Activators and inactivators

Some compounds can act as modulators of ion channels and either enhance or impair their molecular function being classified as channel activators or inhibitors, respectively. Such compounds bind to a range of different sites in the channel which correlate with the pharmacological effect of the compound in question. Up to 6 different modulator sites can be found in the sodium channels' alpha subunit, harboring for compounds and toxins with activation or inactivation effects (*fig. 16*).

Neurotoxin receptor sites on voltage-gated sodium channels

Receptor site	Neurotoxin	Functional effect
Site 1	Tetrodotoxin Saxitoxin μ-Conotoxin	Pore block
Site 2	Batrachotoxin	Persistent activation enhanced activation, and block of activation
	Veratridine Grayanotoxin Aconitine	
Site 3	α-Scorpion toxins Sea anemone toxins Atrachotoxins	Slowed inactivation
Site 4	β-Scorpion toxins	Enhanced activation
Site 5	Brevetoxins	Enhanced activation and block of inactivation
	Ciguatoxin	
Site 6	δ-Conotoxin	Slowed inactivation

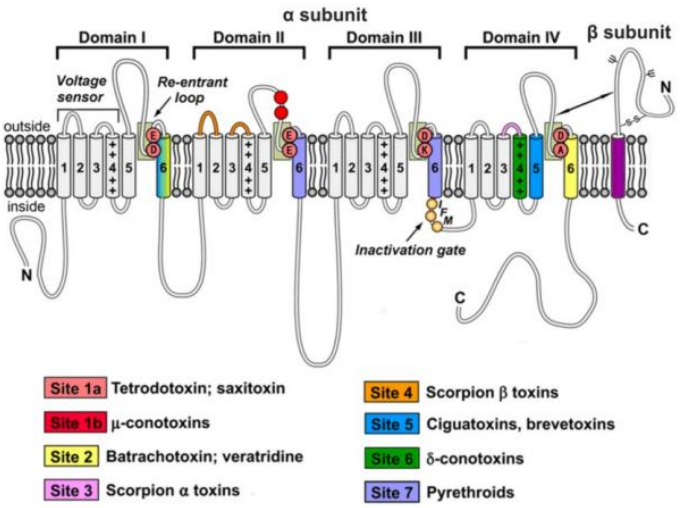

Fig. 16: (left) table of Na_v channel activators and inactivators (from *Catterall et al. (2007)* [39]). (right) simplified secondary structure of a Na_v channel with the modulator binding sites highlighted in colors (from *Zhang et al. (2013)* [67])

The newly discovered $Na_v1.1$-selective activator AA43279 (CAS: 354812-16-1) has been the chosen compound in this project to further elucidate about its mode of action. Despite the affinity of AA43279 for several Na_v isoforms, it is most efficacious for $Na_v1.1$ compared to the next channel, $Na_v1.5$ (2.5-fold vs.2-fold, respectively). The key modulatory effect of AA43279 is an inhibition of channel inactivation, hence resulting in an overall enhanced conductance of $Na_v1.1$. Under a current-time plot (I/t), a rightward shift of the inactivation phase for Na^+ current is observed, subsequently increasing the area under the curve (AUC), the inactivation half-time (tau) and slightly the maximum peak amplitude, for $Na_v1.1$-elicited currents (*fig. 17*). The fact that these effects are observed after the application of atracotoxins[46, 47, 48], α-scorpion toxin[49] or sea anemone toxins[50] (section *4.5. AA43279: effect assessment*), with a known binding in neurotoxin receptor site 3, suggests a probably similar mechanism of action for AA43279.

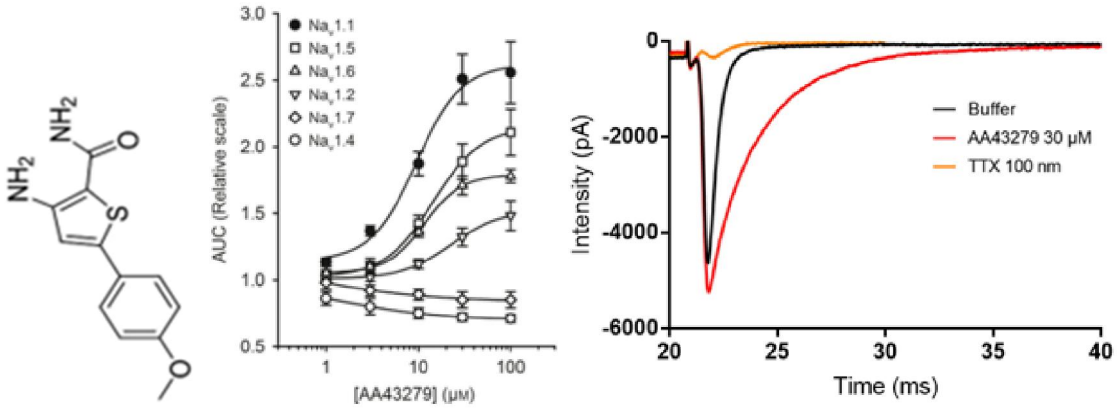

Fig. 17: (left) Molecular structure of AA43279 and (center) its effect on AUC for Na_v isoforms 1.1-1.7 (from *Frederiksen et al. (2017)* [9]). (right) superimposition of I/t sweeps of the same $Na_v1.1$-expressing cell under control conditions (black), modulator (red) and toxin (orange)

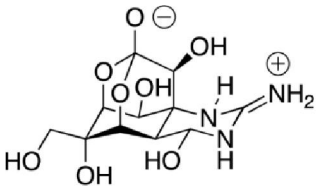

Fig. 18: 3D structure of TTX

The pore blocker tetrodotoxin (TTX, *fig. 18*) has been extensively used in research and it is known to bind sodium channel isoforms $Na_v1.2$, 1.1, 1.4, 1.3, 1.7 and 1.6 in increasing order of affinity[2]. Contrarily, $Na_v1.8$ and 1.9 are resistant to this toxin while $Na_v1.5$ is completely insensitive[38]. The fact that TTX binds inside the channel PFD (neurotoxin receptor site 1) makes it interact with segments S2 to S6 of all domains D1 to D4, sharing a similar toxicology with that of saxitoxin (STX) and μ-conotoxin. In a current-time plot, the main appreciable effect is the great decrease in the Na^+ peak amplitude, sometimes until a complete peak disappearance (*fig. 17 above*).

For its versatility, TTX has been used in this project as there are no $Na_v1.1$- nor $Na_v1.4$-specific inhibitors currently available.

[2] EC_{50} values for TTX are represented: $Na_v1.2$: 12 nM, $Na_v1.1$: 6 nM, $Na_v1.4$: 5 nM, $Na_v1.3$ and $Na_v1.7$: 4 nM, $Na_v1.6$: 1 nM [38]

1.9.2.1. - $Na_v1.1$

The voltage-gated, sodium channel alpha subunit type I ($Na_v1.1$) is encoded by the *SCN1A* gene (Entrez: 6323, UniProt: P35498) which, in *H. sapiens*, is located on chromosome 2. The CDS of *SCN1A* consists of 26 exons measuring 6030 base pairs. Thus, $Na_v1.1$ is a large protein being 2009 amino acids in length and 229 kDa in molecular weight[51]. As with other members of *the sodium ion channel family* (section *1.9.2.*), $Na_v1.1$'s tertiary structure consists of 4 homologous domains (D1-D4), each formed by 6 TM segments (S1-S6), linked by cytoplasmic and extracellular loops. $Na_v1.1$ is an integral membrane protein and, as such, can also structurally be divided into extracellular, transmembrane, and intracellular domains (*fig. 19*). Adding to the complexity, $Na_v1.1$ can be found non-covalently associated with beta subunits (β1-β4) for the modulation of the channel activity. Its structure is prone to conformational changes whereby the closed or "resting" state becomes fully open at -33 mV and conducting for sodium charges, and later inactivated (non-conducting) back at -72 mV during repolarization, to finally adopt the closed state again[38].

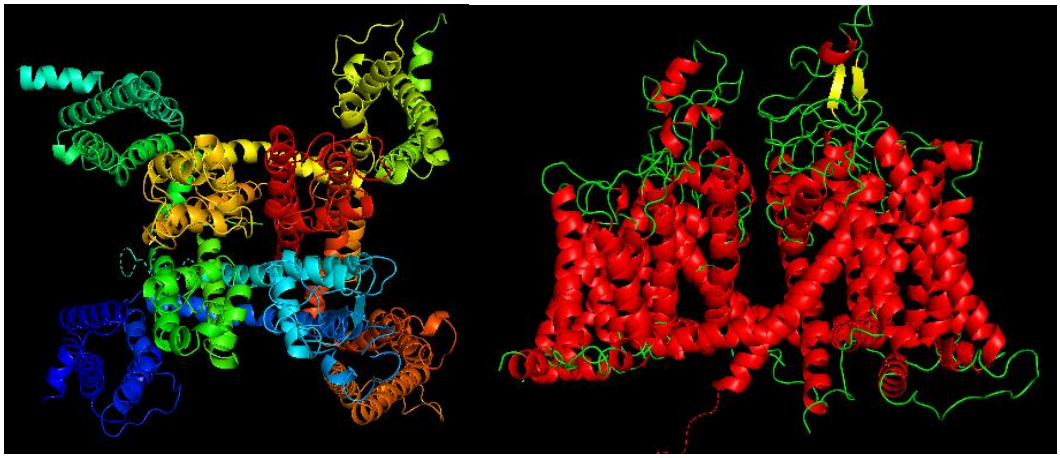

Fig. 19: 3D homology model (from fig. 20) of the tertiary structure of $Na_v1.1$ at its transmembrane section (courtesy of Laurent David, Lundbeck A/S), viewed from the top (left) and side (right). Yellow arrows indicate the portion of homologous β subunit

$Na_v1.1$ is unique among the Na_v channels as its expression is virtually restricted to interneurons. In the GABAergic PV^+ interneurons, $Na_v1.1$ is concentrated at the Axon Initial Segment (AIS) and it is one of the key effectors of their characteristic rapid-firing, fast-spiking action potentials[7, 52].

The unique expression pattern of the channel and the involvement of interneurons in different psychiatric diseases, constitutes $Na_v1.1$ as an attractive drug target. Given the deficit in interneuron firing observed in these diseases, one would hypothesize that an $Na_v1.1$ activator could potentially alleviate this deficiency. Lundbeck has previously discovered several $Na_v1.1$ activators[9, 53] that slow down the inactivation feature of $Na_v1.1$, thus sustaining the channel activation for a longer time and achieving the desired therapeutical effect *in vitro*.

$Na_v1.1$ modulators include activator and inhibitor compounds of the channel's Na^+-elicited current (*fig. 16*). Examples of activators are α-scorpion toxins (α-ScTxs), sea anemone toxins and atracotoxins, which bind to the extracellular loop connecting S3 and S4 in D4, otherwise known as receptor site 3[46-50]. The response obtained from the modulation of this

particular site results in the delay of the channel's fast inactivation phase, provoking a slower inactivation curve during which more Na^+ current is conducted, and thereby increasing the intensity of the action potential[39]. Due to the observation that AA43279 creates these same cellular effects on hippocampal neurons, enriched in $Na_v1.1$, a hypothesis of a similar binding site has been postulated[9]. The former modulators are "*inhibitors of fast inactivation*", ultimately producing an "*activation*". Other classes of $Na_v1.1$ activators, enhancing the activation phase by binding to receptor sites 2, 4 and 5, are fetched in *fig. 16* (section *1.9.2.bis Activators and inactivators*).

Inhibitors of $Na_v1.1$-mediated current include the non-selective TTX and saxitoxin (STX) in binding site 1, functioning as pore blockers[39].

1.9.2.2. - $Na_v1.4$

The 5511 bp CDS of the *SCN4A* gene encodes the sodium channel $Na_v1.4$ alpha subunit being 1836 residues in length[54] (Entrez: 6329, Uniprot: 35499). The secondary structure is similar to that of the rest of human sodium channels (*fig. 20*), only with namely point mutations in it (*fig. 26*). Only beta subunit β1 has been associated with this channel. A conformational change occurs in $Na_v1.4$ at -26 mV for activation and -56 mV for inactivation in CHO cells[38].

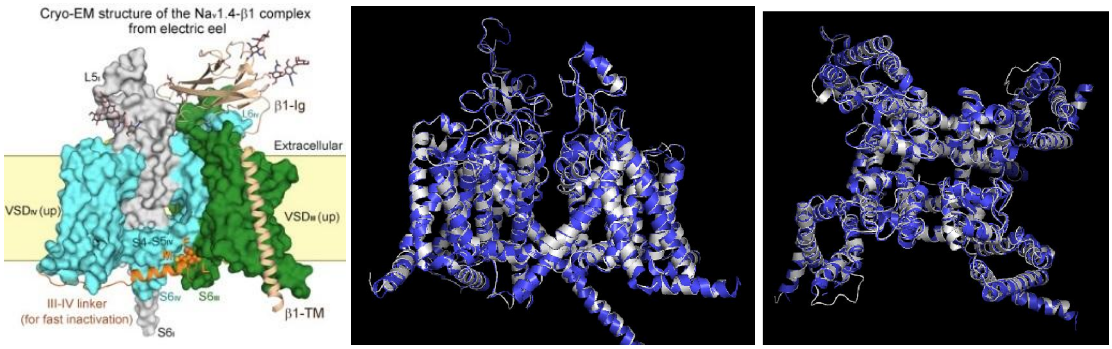

Fig. 20. Left: cryo-EM structure of eeNav1.4 (from *Yan et al. (2017)*[91]). Center and right: 3D transmembrane alignment between the $eeNa_v1.4$ channel (blue) and $hNa_v1.1$ (white), viewed from the side and top

The $Na_v1.4$ molecular structure from *E. electricus* ($eeNa_v1.4$, PDB: 5XSY), with open pore and associated to β1, has been resolved by cryo-electron microscopy (cryo-EM, *fig. 20*) with at a resolution of 4.0 Å by *Yan et al. (2017)*[91]. The nearly-atomical imaging structure revealed interesting properties of this channel such as a potential allosteric binding site for fast inactivation, the interaction of β1 with the VSD in D3 and extracellular loops, and further detailed insights of the particular structure mechanisms for conformational change.

Expression of human $Na_v1.4$ ($hNa_v1.4$) is restricted to skeletal muscle cells, driving the generation and transmission of APs in said tissues, and hence constituting a unique target for the selective treatment of myotonic diseases and other muscle channelopathies. Activators for this channel include the alkaloids veratridine, batracotoxin[55] and grayanotoxin[56] – all binding to site 2 – and β-scorpion toxin (β-ScTx)[57,58] – binding to site 4[39]. Inhibitors include the wide-spectrum TTX and saxitoxin, with μ-conotoxins being $Na_v1.4$-selective[59].

From a neurobiology point of view however, the choice of this channel for the development of this project's objectives was made from the observation of the absence of effect for the $Na_v1.1$ activator AA43279 (*fig. 17, center*). In fact, the binding of this ligand to $Na_v1.4$ causes a modest inhibition of its activity with a modest decrease in total current, AUC and reduction in the maximum peak amplitude as well. A complementation strategy, consisting on splitting the $Na_v1.4$ and $Na_v1.1$ domains and co-expressing them for analyzing changes on AA43279 binding, is the basis of this project.

1.9.3. - The potassium ion channel family

Up to 40 K^+ channel genes classified into 12 different phylogenetic families compose the most diverse and largest type of ion channels[60]. The main role of potassium channels in excitable cells is the re- and hyperpolarization of the membrane necessary for the AP termination and the cell return to a resting state, readying it for further stimuli. Such effect is achieved due to the conduction of intracellular K^+ ions out of the cell as dictated by the electrochemical gradient – oppositely to the direction of the extracellular Na^+ ions that generated the AP in the first place.

Voltage-gated potassium channel (VGKC) families can be further distributed depending on their specific molecular characteristics *current-wise*. Delayed rectifier and A-type channels are the most frequent eliciting ones, while a good fraction made of inward- and outward-rectifying channels prolongate said K^+ currents.

The tetramerization T_1 domain in the N(t) of K^+ channels allows the vast majority of K_v monomers to oligomerize with more subunits of their kind (*fig. 21*), thus enabling said proteins to be encoded in a more compact gene size[61, 62]. K_v monomers with the ability to homotetramerize virtually include all *KCN*-encoded α-subunits. In addition for versatility, some K_v monomers can also oligomerize with other K_v isoforms. Heterotetramerization has been found to occur in $K_v1.2$, $K_v2.1$, $K_v7.2$ and $K_v7.3$, with the first and last pair of monomers being able to hybridize into 2x $K_v1.2$- $K_v2.1$ and 2x $K_v7.2$- $K_v7.3$ channels[63].

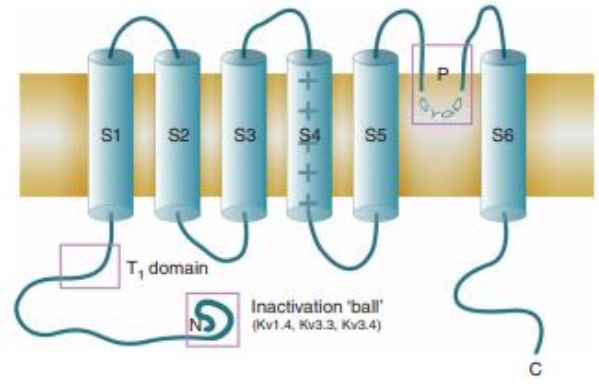

Fig. 21: schematic of the secondary structure of VGKCs. A channel with ball-and-chain and T_1 domains is represented (from *Rudy, B., et al (2010)*[61])

1.9.3.1. - $K_v2.1$

The *shab*-related, voltage gated potassium channel member 1, is encoded by a 2577 bp-long CDS of the *KCNB1* gene (Entrez: 3745, Uniprot: Q14721), located in chromosome 20 of *H. sapiens*. The resulting transcript is later translated into an 858-residue domain of 6 TM α-helices that, yet small in size, is able to homotetramerize in the cell membrane thus producing a functional K^+ channel[64].

$K_v2.1$ is a widely expressed outward delayed rectifier K^+ channel in the brain, a main contributor to the repolarization to the resting state in majorly cortical and hippocampal pyramidal neurons, and to a lesser extent in interneurons. It also regulates the frequency and duration in repetitive APs, the following neuronal excitability to new stimuli, and even neurotransmitter release[65]. Out of a neurobiology context, $K_v2.1$ can contribute to insulin release in beta-pancreatic cells, heart rate and contraction of smooth muscles among other functions[64]. Furthermore, $K_v2.1$ has the ability to form heteromultimers with other α-subunit monomers, namely with those of the non-functional modifier/silencer sort. Complexes with $K_v1.2$ (*fig. 22*), $K_v2.2$, $K_v5.1$, $K_v6.1$, $K_v6.3$, $K_v6.4$, $K_v8.1$, $K_v9.1$, $K_v9.2$, $K_v9.3$, $K_v12.1$ and $K_v12.2$ monomers have been reported to provide $K_v2.1$ with diverse regulation on its repolarization role across tissues[64]. Mutations in *KCNB1* can also lead to the appearance of heterogeneous epileptic encephalopathies[66].

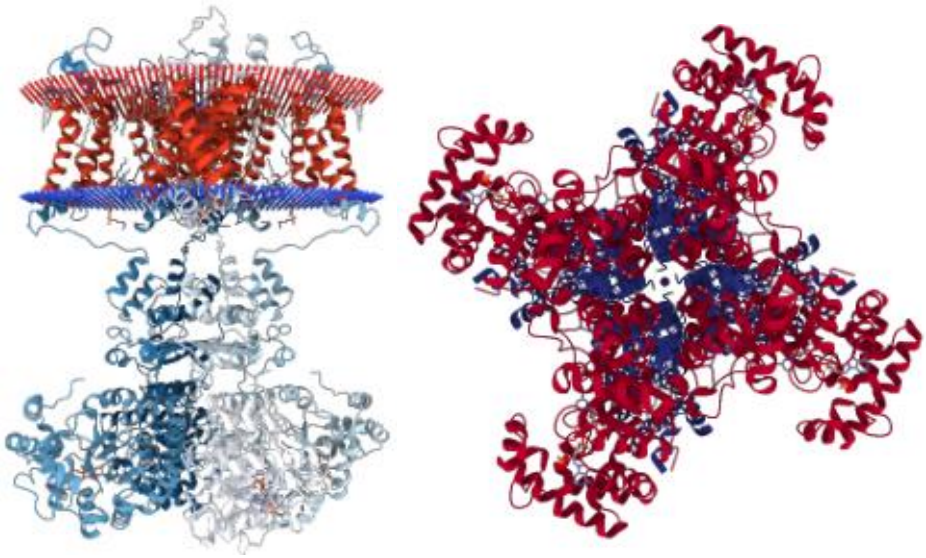

Fig. 22: PDB structure (2R9R) of a hybrid Kv1.2-Kv2.1 channel viewed from the side (left) and top (right). No $K_v2.1$-only structures were available as of August 2018

A typical $K_v2.1$-elicited K^+ current is exemplified in *fig. 23*. A sharp rising phase corresponding to channel activation precedes a brief peak and following characteristic slow descent of current of "delayed-rectifier" K_v channels. The channel remains open thus generating a sustained K^+ current that further drives the cell potential to more negative values (*not shown*), upon which a sudden conformational change to the inactivated state brings the current to a halt.

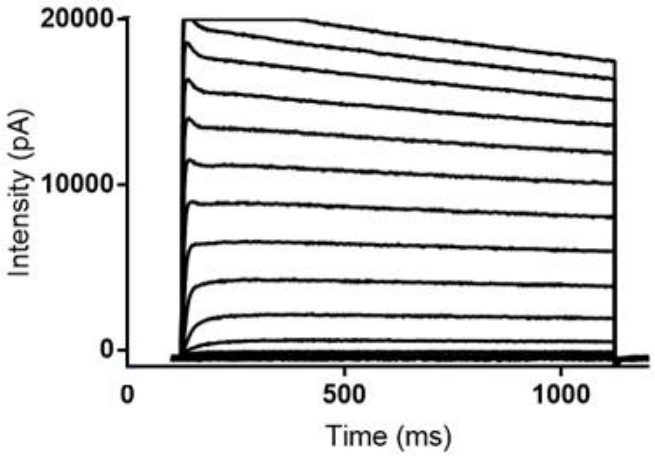

Fig. 23: I/V plot of an sfGFP-tagged K_v2.1 channel (section *3.5. K_v-sfGFP + sfGFP-K_v*). Recording threshold is +20000 pA

The purpose of employing a simpler, yet not project-related ion channel as K_v2.1, was due to its structural simplicity for cloning, expression and patch-clamping altogether, necessary during the first attempts for refining the methodology later utilized in Na_v channels. The reduced domain size and its ability to homotetramerize allows for an enhanced overall expression and following higher channel abundance in the membrane. Furthermore, a very efficient conductance (*fig. 23*) normally reaching tenths of thousands picoamperes (pA) is characteristic of K_v channels and thus optimal for electrophysiological recordings.

1.10. Electrophysiology

Electrophysiology techniques serve to detect and analyze electrical currents produced in excitable cells and tissues. On a bigger scale, the electrical properties of whole organs can be analyzed as in electrocardiograms or EEGs. The previous are examples of extracellular, non-invasive techniques, while intracellular recordings require inserting a measuring electrode inside the cell membrane, usually enveloped inside a borosilicate micropipette filled with an ionic intracellular solution similar to that of the cytoplasm.

To achieve this, the pipette can directly penetrate across the cell membrane, or rather have atmospheric pressure applied to it so to adhere the membrane (patching) in a *cell-attached* mode. The physical suction between the two components, in order of GΩ (gigaseals), can then be broken by removing the pipette with its attached membrane "patch" and record in either *inside-out* or *outside-out* configurations. If the pipette is not removed, but instead more suction is applied to break the patched area, a circuit continuum is created between the electrode and the cell membrane in what is known as a *whole-cell* configuration (*fig. 24*).

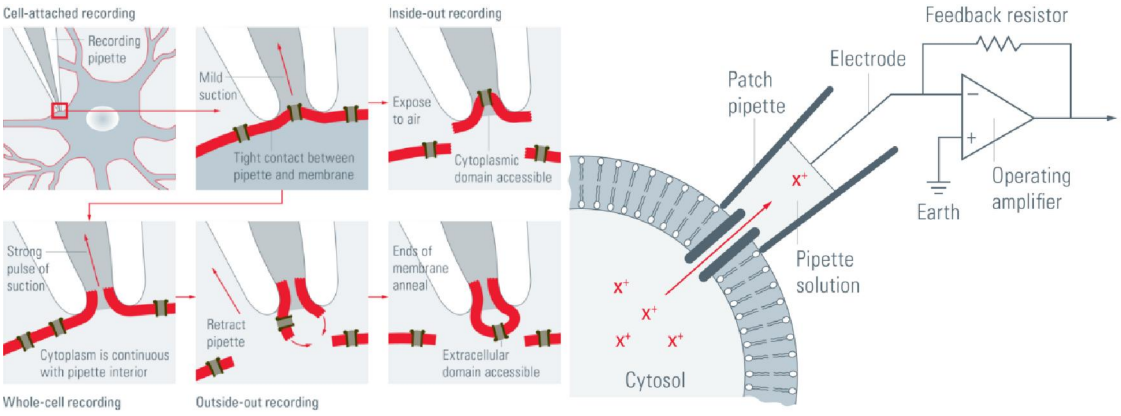

Fig. 24: (left) diagrams showing the most common cellular patching techniques and (right) electronical configuration of a *whole-cell* experiment (© Leica Microsystems GmbH)

1.10.1. Voltage-Clamp

Once patched, the electrode allows to measure either the cell-elicited voltages or currents one at a time, provided the other parameter is locked or controlled at user-induced magnitudes (clamping). Artificial ion currents can be introduced in the cell to observe their distribution across the membrane and have the difference in potential (voltage) measured in a *current-clamp* mode. However, a more useful technique involves applying artificial voltages to the membrane to trigger the VGICs open and conducting for ions to permeate through, thereby producing an electrical flow (current) across the apolar membrane. This is the *voltage-clamp* mode.

The Nernst and GHK equations are used to calculate the membrane potentials as logarithmic quotients between extra- and intracellular ion concentrations (*fig. 25*). Therefore, and should the ion have positive valence, currents flowing in an inward cell direction are represented negative in intensity vs. voltage (I/V) or vs. time (I/t) plots, positive for outward currents, and vice-versa for negatively-charged ions[34].

$$E_X = \frac{RT}{zF} \ln \frac{[X]_{out}}{[X]_{in}} \qquad V_m = \frac{RT}{F} \ln \left(\frac{p_K[K^+]_o + p_{Na}[Na^+]_o + p_{Cl}[Cl^-]_i}{p_K[K^+]_i + p_{Na}[Na^+]_i + p_{Cl}[Cl^-]_o} \right)$$

Fig. 25: Nernst (left) and Goldman-Hodgkin-Katz (right) equations

The exact electrophysiological technique utilized in this project is the *manual whole-cell patch, one electrode voltage-clamp intracellular recording*, or voltage-clamp in short, and often referred to as MPC (manual patch-clamp) along this thesis.

2. AIM OF THIS STUDY

The main purpose of this Master's Thesis project is to identify the binding region of the sodium channel activator AA43279 in the human sodium channel $Na_v1.1$ (*SCN1A*)[9]. Interneurons are enriched in this specific channel isoform and is therefore likely of relevance for the treatment of diseases with impaired synaptic transmission, like schizophrenia. While AA43279 is efficacious on some Na_v channels, it shows inhibition effects on $Na_v1.4$.

Mechanistically, AA43279 slows down the fast inactivation of the $Na_v1.1$ channel, thereby increasing the amount of current elicited – i.e., its conductance.

Similarly, this same pharmacological effect has been observed after the application of α-ScTx and other toxins[n], which bind to channel site 3, located in the loop between TM helices S3 and S4 in domain 4[**67**]. Interestingly, aligning $Na_v1.1$ to $Na_v1.4$ reveals these two channels differ most in this particular region (*fig. 26*).

Thus, and based on these observations, we hypothesized that AA43279 binds to a site within or near site 3 on the $Na_v1.1$ channel.

As Na_v channels are very large in size and thus difficult to clone, mutate and express, we sought to develop a modular approach based on complementation to test our hypothesis. Specifically, we *first* split each Na_v channel cDNA into two separate halves and co-expressed different combinations of said $Na_v1.1$ and $Na_v1.4$ modules.

Later, and upon the difficulties in the functional intermodular interactions between the $Na_v1.1$ and 1.4 halves, the purported binding region of AA43279 within $Na_v1.1$ was narrowed down with replacements of said section with that in $Na_v1.4$. The resulting unsplit, chimeric channels featured predominant $Na_v1.1$ structures but with its suspected critical domains, the D4 domain and its VSD region, replaced with those from $Na_v1.4$.

It is expected that the experimental data and the conclusions drawn could aid in the refinement of this method in the future, eventually making it useful to develop more selective and potent $Na_v1.1$ modulators.

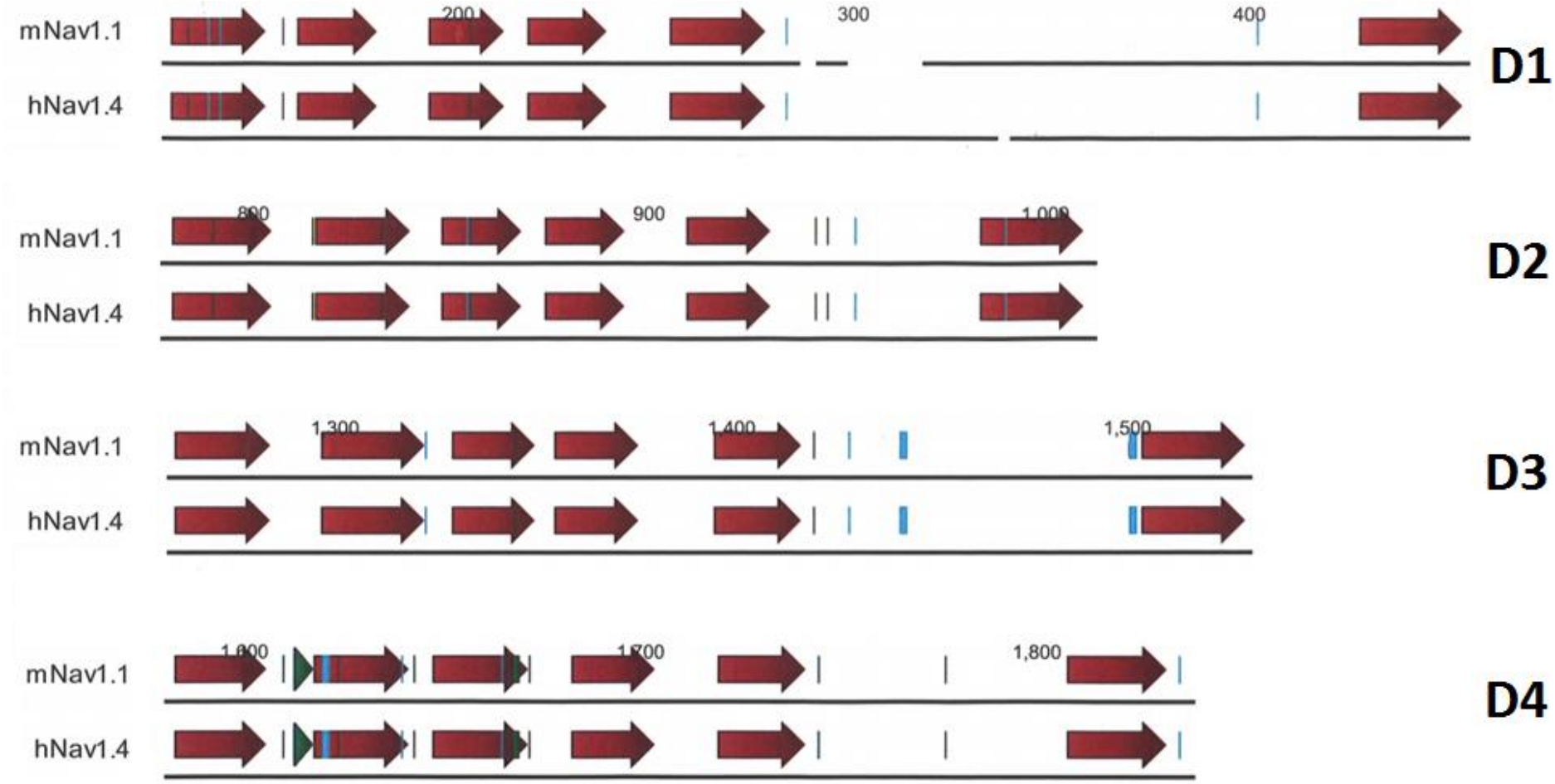

Fig. 26: local alignment of the mNav1.1 vs. hNav1.4 sequence, Domains I-IV are arranged vertically, segments 1-6 are represented horizontally in arrows, point sequence mutations are colored cross-bars

3. RESULTS

3.1. – Prelude to results

To identify the binding region of AA43279 in $Na_v1.1$ we exploited the observation that the compound is efficacious on $Na_v1.1$ but in turn is inhibitory on $Na_v1.4$[9] (*figs. 17* and *28*). The modular approach followed consisted on the co-expression of $Na_v1.1/1.4$ first (D1D2) and last (D3D4) pairs of domains, here referred to as "dimers" or "halves". This strategy would both ease the molecular biology workload, and allow the option to co-express different all combinations of halves if they were to form functional channels.

As mentioned, the inserts' sheer size posed large difficulties even when subcloning. Therefore, the channels' halves were amplified by directed PCR of their domains I and II (hereinafter: $Na_v1.xD1D2$) or domains III and IV (hereinafter: $Na_v1.xD3D4$) along with their cytoplasmic loops. Co-expression of the constituent subunits of the channels would manage to achieve sufficient product amount to reach the plasma membrane. However, concerns were also raised on whether these Na_v halves would functionally interact with their counterparts, or otherwise be conducting by themselves alone or by self-dimerization. In addition, analyses of the electrophysiological properties of these dimers would not be feasible by methods that would impair their intended live functionalization.

Therefore, these requirements were met with the addition of super-folded, split GFPs (sfGFP) to each of the dimers (*fig. 27*). This modified GFP is engineered to have its 11 β-strands separated into one larger, soluble part featuring strands 1 to 10 (hereinafter: sfGFP1-10), and the 11^{th} strand peptide (hereinafter: sfGFP11), allowing for an observable live complementation[68]. By exploiting this property, the $Na_v1.xD1D2$ dimers were tagged with sfGFP1-10, while the $Na_v1.xD3D4$ dimers were tagged with sfGFP11, additionally expecting the ensuing affinity between the sfGFP parts to drive the Na_v dimers together as well. As an early proof-of-concept experiment, a simpler $K_v2.1$ channel was sfGFP-tagged this way due to its structural simplicity and ability to tetramerize, easing the work during cloning, expression and patching.

Fig. 27: cartoon representation of sfGFP1-10 (left), sfGFP11 (center) and sfGFP (right, *from Kamiyama, D. et al.(2016)*[68])

The brief rationale followed above is explained in detail, along with the specific design for the experiments performed, in the following sections.

3.2. - Analysis of native channels

The effect of AA43279 on full-length $Na_v1.1$ and 1.4 channels was analyzed by manual patch-clamp recordings (MPC). This enabled a validation of the used electrophysiological method and allowed comparison with previous AA43279 data[9] (*fig. 28*) obtained using automated patch-clamp (APC). HEK cells stably-expressing $Na_v1.1$ or transiently-transfected $Na_v1.4$-expressing cells were submitted to *Step* and *IV* protocols (*fig. 31*). Cells under the same analysis run were put under control conditions with extracellular buffer, a single dose of AA43279, and TTX-mediated channel blocking as a final control for a confirmation of Na_v-elicited Na^+ currents.

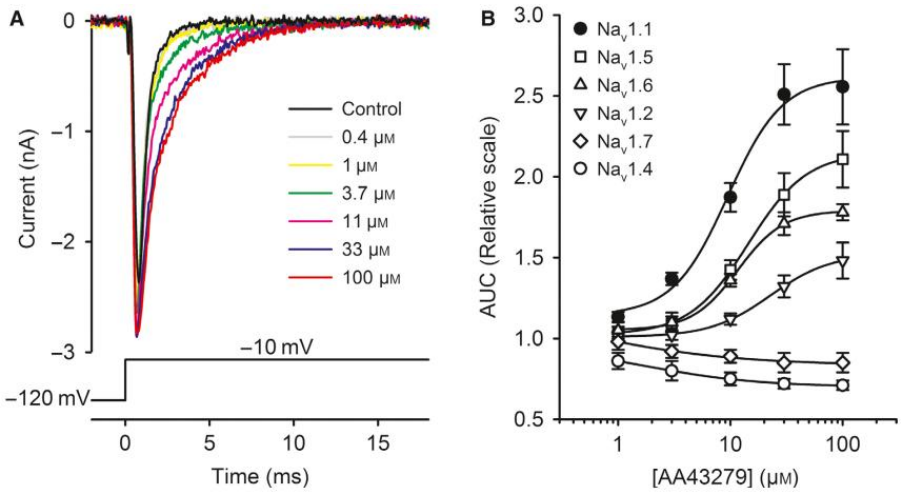

Fig. 28: (left) MPIs of the same representative cell with increasing AA43279 concentrations under an APC experiment. (right) Dose-response curves showing AUC variations for different Na_v isoforms (from Frederiksen et al. (2017) [9])

In general, the data analyzed from MPC confirmed a concentration-dependent increase (*fig. 28*) in the maximum peak intensity (MPI), area under the curve (AUC) and tau constants for $Na_v1.1$, according to APC results in published literature[9]. Furthermore, dose-response curves for $Na_v1.1$ were represented with high similarity to the ones in the article as well. The following sections describe the results obtained and depict the graph plots drawn from them.

3.2.1. - $Na_v1.1$ – Published literature

AA43279 is most efficacious over $Na_v1.1$ than the rest of Na_v isoforms. Despite a modest 1.2-fold increase in MPI is observed, average increases of 2.3-fold in AUC and 3.1-fold in tau are responsible of $Na_v1.1$'s rise in conductance (*fig. 29 below*). Larger AUCs are directly translated into a higher channel conductance over the same period of time (*fig. 28 above*), and into a tau increase (elapsed time after which MPI halves), which is also responsible of the key effect of AA443279 in delaying the fast inactivation phase of $Na_v1.1$. Altogether, a pronounced rightward shift in the curve's inactivation slope is ultimately provoked (*fig. 17, right*).

	$Na_v1.1$	$Na_v1.2$	$Na_v1.4$	$Na_v1.5$	$Na_v1.6$	$Na_v1.7$
Peak	120 ± 23	100 ± 12	86 ± 5	85 ± 15	88 ± 4	96 ± 5
AUC	230 ± 23	130 ± 14	75 ± 5	190 ± 15	170 ± 4	86 ± 5
Tau	310 ± 29	150 ± 12	89 ± 5	270 ± 15	220 ± 4	93 ± 6

Fig. 29: increases over buffer baseline (100) after AA43279 30 µM application in MPI (pA), AUC (pA/ms) and tau (ms), along with SD values (from Frederiksen et al. (2017) [9])

Another desired therapeutical effect of AA43279 is the restoration of the current baseline after the cessation of stimulatory impulse, recovering a 0 pA level with no persistent effects. Oppositely, the pharmacologically-similar Lundbeck compound Lu AE98134 differs in the creation of a persistent inward Na^+ current lasting after the stimulus application[53], and specifically hampering the conformational change of the channel from the open to the inactivated state (*fig. 30*).

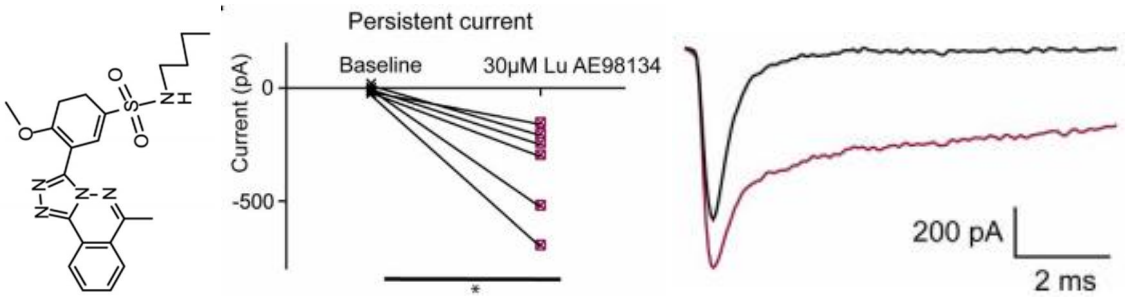

Fig. 30: molecular structure of Lu AE98134 (left), persistent currents after cessation of impulse (center) and representative sweep (right) of the effect in an I/t curve (buffer: black; Lu AE98134: purple) (from *von Schoubye et al. (2018)* [53])

3.2.1.1. - $Na_v1.1$ – Manual patch-clamp

A lineage of HEK293 cells stably expressing $Na_v1.1$ were individually analyzed at AA43279 concentrations of 30 µM (n = 6), 10 µM (n = 6), 3 µM (n = 4), 1 µM (n = 5) and 0.3 µM (n = 3), along with previous control recordings with extracellular buffer.

The *Step* stimulatory protocol (*fig. 31*) was automatically applied every 20 s with 3 differentiated phases. A holding potential of -80 mV was maintained in between stimulations to cancel any Na_v-elicited Na^+ currents. Prior to depolarizations, a 20 ms -120 mV hyperpolarization was applied to ready all Na_v channels from the inactivated into the closed conformation. Sudden depolarizing sweeps to -10 mV for 20 ms caused full activation of all cell channels. Finally, the potential was held at -80 mV again allowing for the re-establishment of ionic concentrations.

Another 3-phase stimulus protocol was applied in a manual, single manner after the full cell responses were observed. The "*IV*" protocol, programmed to sequentially apply Δ+10 mV impulses from -120 mV to +50 mV every 2 s (*fig. 31*), was utilized to draw the channel's elicited intensity vs. voltage relation (I/V), activation and inactivation constants under the different conditions applied. Currents elicited by $Na_v1.1$ were observed to take place at approximately 1.2 ms after the depolarizing transient capacitance.

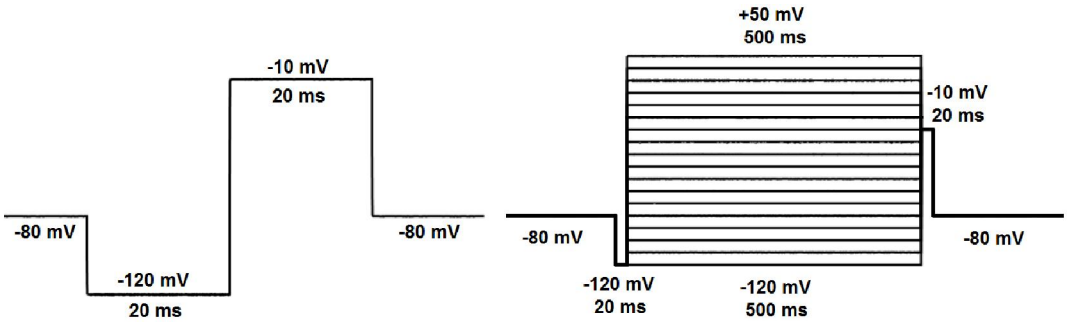

Fig. 31: schematic of the *Step* (left) and *IV* (right) protocols applied

$Na_v1.1$	30 µM	10 µM	3 µM	1 µM	0.3 µM
MPI	115 ± 16	120 ± 15	105 ± 5	108 ± 6	109 ± 9
AUC	377 ± 60	389 ± 85	292 ± 80	198 ± 23	152 ± 27
Tau	360 ± 100	297 ± 66	167 ± 11	122 ± 11	101 ± 15

Table 1: average increases in $Na_v1.1$ parameters (over buffer) with varying concentrations of AA43279. Values are represented as increases or decreases in regards to baseline (100). Error values are stated in SD

3.2.1.1.1. - $Na_v1.1$ – MPI

MPIs were extracted in Clampfit software by delimiting the peak curve while excluding secondary fused peaks, and recordings underneath -500 pA were discarded (section *3.2.3. Endogenous currents in control cells*). Peak increase after AA43279 application was found not to be *always* concomitant to its original intensity under buffer. Neither to the AA43279 concentration applied (paragraph below), but heavily depended over it: an explanation could point to the plateau in the effect for AUC between 10-30 µM (see following section), reported by MPC.

Application of AA43279 had a slight increase effect on the MPI the higher the concentration was, being appreciable at 30 µM and 10 µM and less noticeable at lower concentrations (*fig. 32*). Increases were recorded for 30 µM AA43279 from a 1.1-fold up to a 1.4-fold, with a 1.45-fold maximum under 10 µM AA43279. Slight decreases of -2% and -4% were noticed in some cells: possible explanations for such phenomenon may indicate a sustained cell leak or membrane closing over the course of the recordings. For instance, the biggest $Na_v1.1$-elicited peak dropped from -6560 pA to -6300 pA (0.96-fold) during 30 µM AA43279 application.

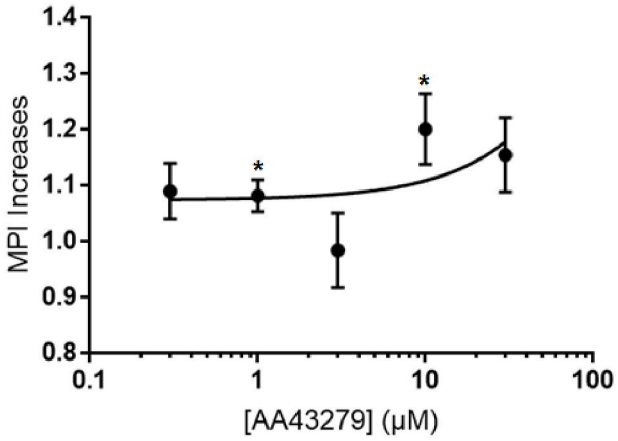

Fig. 32: dose-response curve of MPI increases for $Na_v1.1$ between 0.3 - 30 µM AA43279 (X axis) and fold increases (Y axis) normalized in regards to baseline (1). Function is linear, error bars expressed as ± SD values (*: $p < 0.05$)

3.2.1.1.2. - $Na_v1.1$ – AUC

AUCs were calculated by selecting the Na^+ curve from the beginning of the activation slope (descent into negative potentials), past the peak, and until a restoration of the baseline of the current to 0 pA after the rising slope (*fig. 33*). The area value (in pA/ms) is calculated as the sum of infinitesimal time/intensity integrals the activation curve can be divided into.

Increase in AUC was equally depending proportionally on the AA43279 concentration, but sometimes exceptions were found at lower applications likewise. For 30 µM AA43279, increases ranged from a 3-fold to a 4.5-fold, while a maximum of 5.1-fold was recorded under 10 µM AA43279. A decreasing effect in AUC was never observed. The effect on AUC increase was always observed as a broadening of the Na^+ inactivation slopes and not on the activation ones.

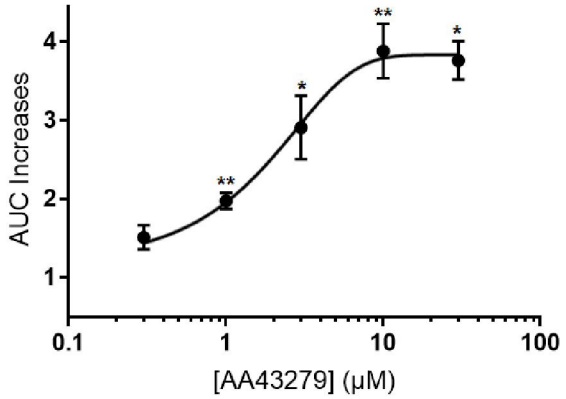

Fig. 33: dose-response curve of AUC increases for $Na_v1.1$ between 0.3 - 30 µM AA43279 (X axis) and fold increases (Y axis) normalized in regards to baseline (1). Function is fitted into a 4-parameter sigmoid, error bars expressed as ± SD values (*: $p < 0.05$; **: $p < 0.01$)

Saturation is observed around a 30 µM concentration range, with maximum dose-response slopes between 1 and 10 µM in close accordance to published literature[9]. Therefore, application of higher concentrations was considered not to be necessary.

The effective concentration needed to achieve half of the maximum activation for a given parameter is the EC_{50} value. From the previous section, the EC_{50} producing half of the maximum AUC achievable can be interpolated from the curve's nonlinear fit at 2.3 µM AA43279.

Ext. buffer	MPC	APC
NaCl	150	140
KCl	3	3
$MgCl_2$	1	1
$CaCl_2$	1	1
HEPES	10	5
$CdCl_2$	-	0.1
TEA-Cl	-	20
Sucrose	-	320
pH (HCl/NaOH)	7.3	7.3

Int. buffer	MPC	APC
NaCl	10	10
CsF	140	140
HEPES	10	5
EGTA	0.5	1
Sucrose	-	320
pH (HCl/CsOH)	7.3	7.3

Table 2. Components (in mM/mOsm) of the extracellular (left) and intracellular (right) buffer solutions used in the APC experiments (from Frederiksen et al. (2017) [9]) and utilized in this project (MPC)

A discordance is found in regards to APC results[9], which set the EC_{50} value at 9.5 µM. Differences in buffer ion concentrations were minimal, although some elements were not present in MPC (see table 2.). Step protocols were not used in APC and the IV protocols were modified but still maintained common sweeps in $Na_v1.1$'s activation range (-40 - -10 mV). Finally, applications of up to 100 µM AA43279 in said research may also be the cause of a different sigmoidal fit employed for the calculation of the EC_{50} value.

3.2.1.1.3. - $Na_v1.1$ – tau

The tau values (τ or $t_{1/2}$) of inactivation for each cell patched correspond to the elapsed time after which its MPI halves. These time values were extracted manually and their inactivation curves fitted automatically. The majority of inactivation slopes fit into a 2nd order exponential curve under buffer, and varying orders (1st to 6th) were observed for AA43279, often not being constant for one single concentration.

Application of AA43279 caused a notable delay in the inactivation phase in a concentration-dependent manner likewise. On average, 30 µM AA43279 increased tau values in a 3.6-fold, similarly to the results published[9], and 10 µM AA43279 induced a 2-fold increase. In practice, the mean $t_{1/2}$ values under buffer marked 0.51 ms while 30 µM AA43279 prolonged these to 1.62 ms, and up to 1.57 ms with 10 µM AA43279 (*fig. 33*).

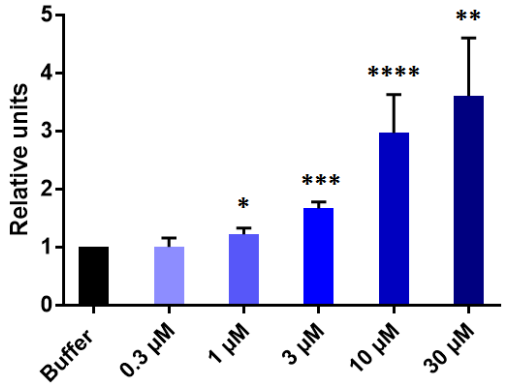

Fig. 33: tau increases for $Na_v1.1$ between 0.3 - 30 µM AA43279 (X axis) and fold increases (Y axis) normalized in regards to baseline (1). Error bars expressed as ± SD values (*: $p < 0.05$; **: $p < 0.01$; ***: $p < 0.001$; ****: $p < 0.0001$). RUs are in time units

3.2.1.1.4. - $Na_v1.1$ – I/V relation

Intensity vs. voltage relations can detailedly describe the behavior of the different fractions of Na_v expressed in a cell (*fig. 34*). First, the resting phase from -120 to -60 mV indicates no net activation of any $Na_v1.1$ channel. A descent in the baseline around -50 mV shows a first little fraction of $Na_v1.1$ channels transitioning to the open state, with the last of the channel fractions becoming active at -30 mV or -20 mV. For more positive potentials, a linear ascending phase is observed in the I/V plots indicating that, despite the Na_v channels remain open, a descent in the net Na^+ inward flow takes place. This is physically explained by the electrical field applied affecting the electrochemical Na^+ gradient, and not by any biomolecular impediments. Extrapolation of this trend (under buffer) gives an intersection at the plot's X axis of approximately +69.53 mV, the calculated Nernst (or reversal) potential for sodium at 25ºC, a turning point beyond which the Na^+ flow is inverted - experimentally - through the same open Na_v channels.

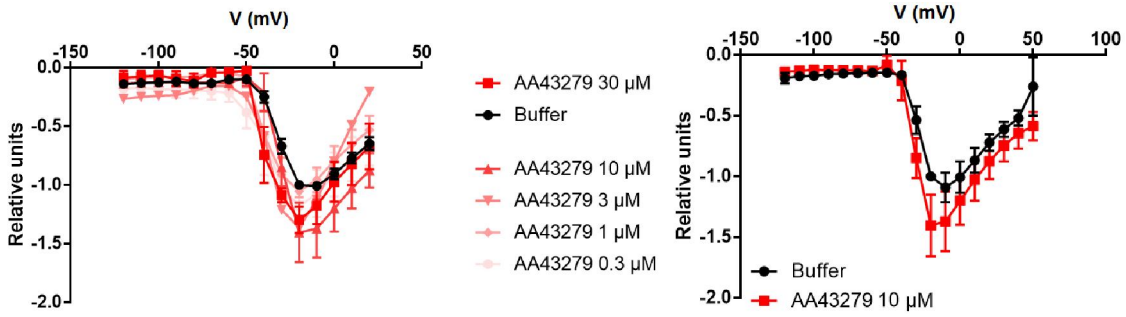

Fig. 34. Left: I/V plot normalized at -20 mV for buffer (1, black) with all AA43279 concentrations (degrees of red). Right: representative I/V plot at 10 µM AA43279, and a maximum peak at -30 mV. RUs are in intensity units

The I/V plots for $Na_v1.1$ show a common maximum ratio reached at around -20 mV for maximum conductance, in accordance to experimental data showing $Na_v1.1$'s $V_{50_{act}}$ at -33 mV[38] (section *1.9.2.1. $Na_v1.1$*). Punctual exceptions were also found at -30 or -10 mV. Indeed, the most intense $Na_v1.1$ current was elicited at -40 mV, increasing from a -4287 pA baseline to a -6677 pA maximum under 30 µM AA43279. At -30 mV however, the maximum buffer baseline was recorded at -5155 pA and increased up to -6152 pA with compound.

3.2.1.1.5. - $Na_v1.1$ – Activation

Steady-state activation relations (SSA, but hereinafter referred to as "activation") were calculated plotting Na^+ conductance ($G_{Na+} = I_{Na+} / V_m - E_m$) vs. voltage applied, and fitted into sigmoidal curves of variable slope. Related to I/V, no net conductance takes place in the -120 to -60 mV range (*fig. 35*), while the first channel activations occur at -50mV and the last ones at around -10 mV. Maximum conductance occurs at around 0 mV under control conditions, while a 30 µM AA43279 application causes a leftward shift for the *plateau* down to -20 mV.

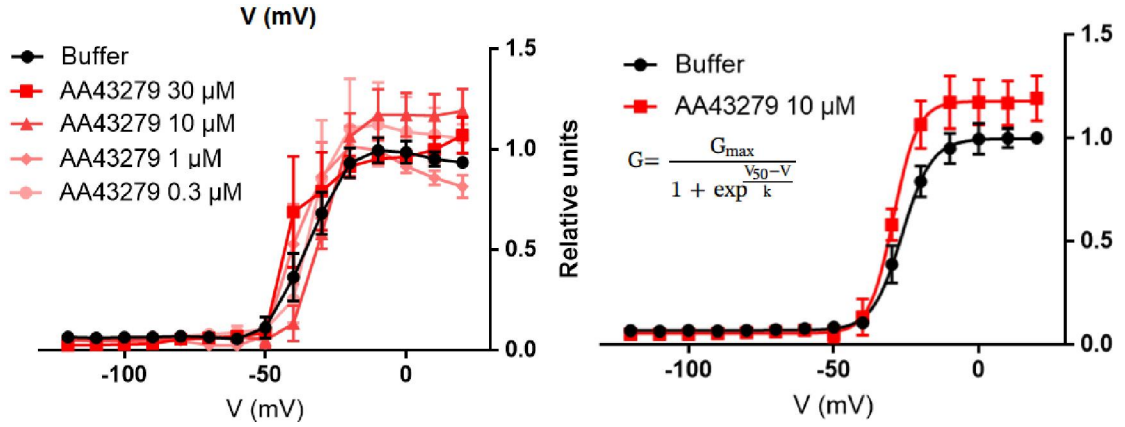

Fig. 35. Left: SSA plot normalized at -20 mV for buffer (1, black) with all AA43279 concentrations (degrees of red). Right: representative SSA plot at 10 µM AA43279 and a maximum peak at -10mV, fitted to the Boltzmann equation (right). Positive values past +20 mV were omitted due to excessive conductance abnormalities. 3 µM was omitted due to inconsistent values. RUs are in conductance units

An approximate 1.2-fold conductance rise is achieved regarding baseline. A robust fitting of the activation relations allows for the voltage values of V_{50act} to be interpolated at each concentration applied. For instance, the averaged control V_{50act} at -35 mV, decreases to -42 mV with 30 µM AA43279, thus making $Na_v1.1$ channels more conducting earlier and during a longer period of time.

3.2.1.1.6. - $Na_v1.1$ – Inactivation

Steady-state inactivation relations (SSI, hereinafter referred to as "inactivation") also fit into a variable-slope sigmoidal curve, represented as an intensity vs. voltage plot. However, the main difference in regards to the I/V relations above showed is that they follow these after their depolarizing stimuli. Thus, SSIs serve to know which fractions of the channels have not yet activated and hence remain available for opening still. The "inactivation" stimuli are the final part of the *IV protocol* described previously for which every sweep is brought to a fixed voltage of -10 mV (*fig. 31, right*), for maximum remnant activation.

A first stage of full conductance is observed between the preceding -120 and -90 mV sweeps in the *IV protocol* when depolarized to -10 mV. The second, decaying phase of conductance occurs between the -80 and -50 mV jumps to -10 mV, values at which Na^+ channels were not previously activated but fail to fully conduct either, because of the preceding depolarizing stimuli in the *IV protocol* not reaching the activation threshold, that ultimately renders the channels unable to fully open (*fig. 36*). A last, third phase with absence of current is observed from -40 mV to more positive potentials when suddenly brought to -10 mV, due to the preceding full activations in the *IV protocol* that do not allow the channels to be closed and re-opened again without a cessation of the stimulus. At the -110 mV to -10 mV step, the most conducting cell elicited a -4678 pA baseline which increased to -5321 pA with 30 µM AA43279.

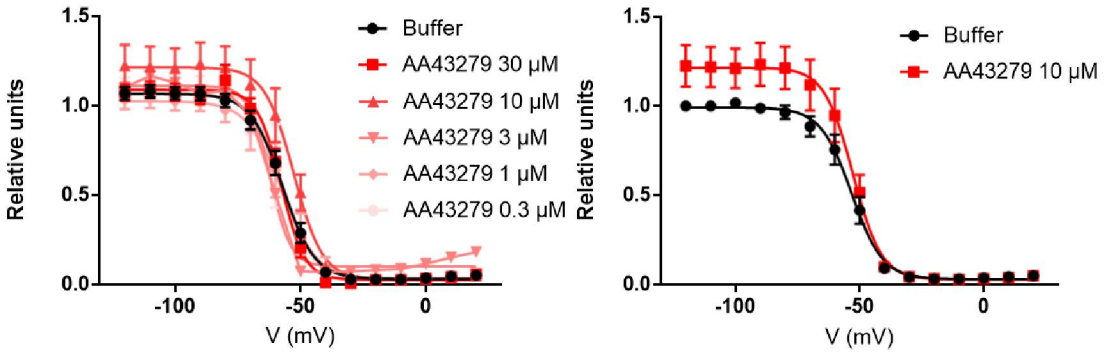

Fig. 36. Left: SSI plot normalized at -20 mV for buffer (1, black) with all AA43279 concentrations (degrees of red). Right: representative SSI plot at 10 µM AA43279, and a maximum peak at -90mV. Plots are fitted to the Boltzmann equation. RUs are in intensity units

AA43279 produces another 1.2-fold conductance increase, related to SSA. Averaged buffer controls for $V_{50_{inact}}$ at -57 mV, increased to -52 mV with a 10 µM AA43279 application, indicating that the modulator effect extends the conductance produced by secondary immediate activations (SSIs) of $Na_v1.1$.

3.2.2. - $Na_v1.4$ – Published literature

The overall effect of 30 µM AA43279 over $Na_v1.4$ is slightly inhibitory, consisting on a reduction in the MPI, AUC, and tau values of 0.86, 0.75 and 0.89-fold respectively. Saturation effects in AUC are reached between 30 and 100 µM (*fig. 28*) with a maximum decrease of only 0.7-fold to buffer baseline. There is an almost a non-existent standard deviation for all the cells analyzed by this automated patch-clamp method during 5 different, independent experiments. Altogether, these data provided with a solid evidence for the $Na_v1.4$ domains to be used as *intramolecular knock-outs* in $Na_v1.1$.

3.2.2.1. - $Na_v1.4$ – Manual patch-clamp

HEK293 cells co-transfected with the *SCN4A* gene and eGFP were cultured between 3-4 days before analysis. Cells were patched with applied AA43279 concentrations of 30 µM (n = 5), 10 µM (n = 3) and 3 µM (n = 3). Parameters in the *Step* and *IV* protocols were not modified. In the majority of cases, $Na_v1.4$-elicited currents also began 1.2 ms after depolarization.

$Na_v1.4$	30 µM	10 µM	3 µM
MPI	104 ± 9	97 ± 5	102 ± 1
AUC	143 ± 21	97 ± 17	112 ± 12
Tau	95 ± 17	97 ± 3	113 ± 23

Table 3: average increases in $Na_v1.4$ parameters (over buffer) with varying concentrations of AA43279. Values are represented as increases or decreases in regards to baseline (100). Error values are stated in SD

3.2.2.1.1. - $Na_v1.4$ – MPI

$Na_v1.4$ elicited MPIs from -400 pA to a maximum of -8477 pA without modulator, showing differences in transfection efficacy. Cells eliciting ≥ -400 pA were discarded as endogenous currents. Slight peak increases were found between 30 µM and 3 µM AA43279 applications, the majority of which averaged to 1.02-folds. A maximum 1.17-fold was recorded at 30 µM. The beforementioned sample for example, increased 1.03-fold up to -8703 pA under 10 µM AA43279. Only 3 had their MPI inhibited at 30 µM and 10 µM AA43279 concentrations, with 0.92, 0.93 and 0.96-folds, in accordance to published literature[9]. In general, the effect of AA43279 on $Na_v1.4$'s MPIs was not significant in regards to baseline.

Because of the lack of effect observed at 3 µM AA43279, experiments at lower concentrations of 1 µM and 0.3 µM were not carried further.

Sometimes the application of TTX did not completely block the $Na_v1.4$-elicited currents, but partially reduced their conductance thus leaving persistent responses to depolarizations (*fig. 37*). The overall intensity of the persistent currents observed under TTX was proportional to the original baseline under buffer. The TTX's mode of action is pore-blocking most members of the Na_v channel family, including $Na_v1.4$. Thus, such phenomena could either be explained by an insufficient TTX concentration (100 nM) or the presence of other endogenous channels (Discussion section *4.4.*).

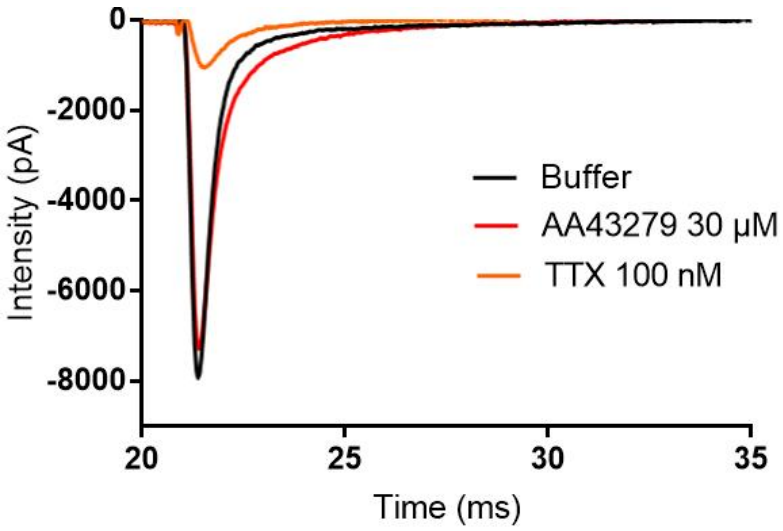

Fig. 37: superimposition of I/t sweeps of a $Na_v1.4$-transfected cell under control conditions (black), modulator (red) and toxin (orange)

3.2.2.1.2. - $Na_v1.4$ – AUC

Effect of AA43279 over $Na_v1.4$ was found to be slightly activating on all samples analyzed except for 2 cells which responded with an AUC decrease of 0.93-fold and 0.83-fold at 10 µM AA43279. Increases in AUC were produced proportionally to the concentration applied, ranging from 1.01-1.24-fold at 3 µM AA43279, to 1.26-1.8-fold with 30 µM AA43279 (*fig. 38*), these last ones considered as significant effects.

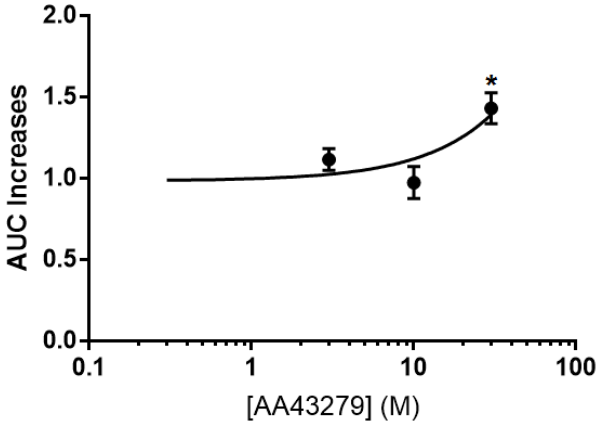

Fig. 38: normalized AUC increases in regards to buffer (1) plotted into a fitted linear fit curve (*: $p < 0.05$)

These data frontally contradict the results obtained from APC[9] which report a trending AUC decrease inversely proportional to concentration, and no absolute AUC increase from baseline in any samples. This could be explained by differences in the protocols applied with each method, specifically in the time of analysis after the application of the modulator. In MPC, the sweep to analyze is chosen based on the observation of the first effects – AUC broadening, MPI reduction – and their immediate stabilization. However, delayed secondary effects were sometimes noticed whereby the width of the broadened $Na_v1.4$'s AUC slightly shrinks, and the reduced MPIs rise again after a prolonged compound application (*fig. 39*), partially recovering the original values under buffer. Another explanation could point to a possible contribution of endogenous channels (section *3.2.3.* and Methods section *4.4.*) as the responsibles of the AUC increase, with AA43279 actually causing inhibition in $Na_v1.4$'s AUC (masked effect due to AUC increase of ECs) and MPI (visible effect).

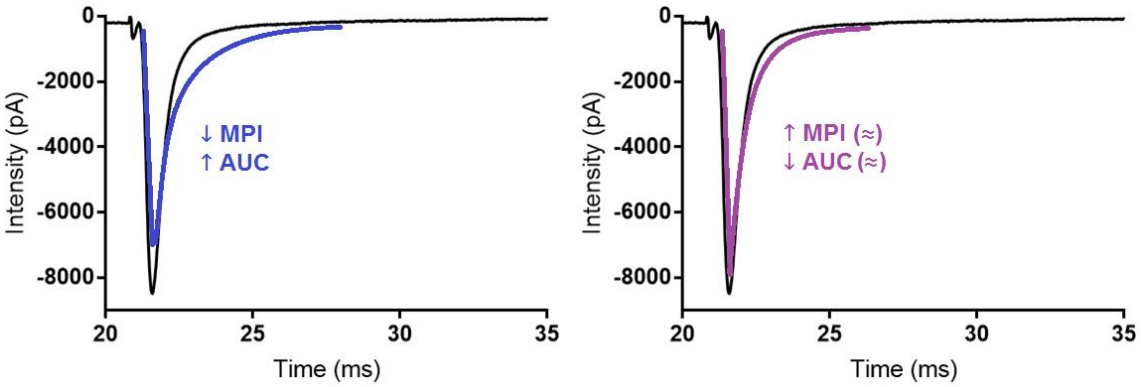

Fig. 39 (modified from fig. 15): immediate observed effects upon AA43279 application (left, blue line) and delayed recoveries observed (right, purple line) should AA43279 be present for an extended period of time

The EC_{50} value for $Na_v1.4$ cannot be calculated properly by MPC for $Na_v1.4$, due to the impossibility to fit an almost-linear AUC plot (*fig. 38 above*) into a 4-parametric sigmoidal curve, and because of the lack of enough data points showing a significant AA43279 effect.

3.2.2.1.3. - $Na_v1.4$ – tau

The effect of AA43279 on the $Na_v1.4$ tau values was negligible, either causing slight increases or decreases in the inactivation half-time point (*fig. 40*). For a mean of 0.51 ms under control conditions, application of 30, 10 and 3 µM concentrations resulted in shifts to 0.59, 0.39 and 0.44 ms respectively. The minor increase observed with 30 µM AA43279 is directly correlated to the AUC increase for the homonymous concentration (section above), while the decreases at lower concentrations would explain the corresponding lacks of AUC increase likewise.

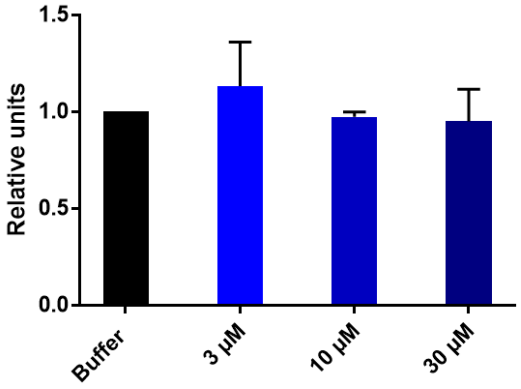

Fig. 40: tau increases for $Na_v1.4$ between 3 - 30 µM AA43279 (X axis) and fold increases (Y axis) normalized in regards to baseline (1). Error bars expressed as ± SD values. RUs are in time units

In agreement with previous results[9], the previous data collectively show that the effect of AA43279 is much less pronounced on $Na_v1.4$ compared to $Na_v1.1$. Moreover, it justifies the use of these two channels in the aim of identifying the binding site of AA43279 using a modular strategy.

3.2.2.1.4. - $Na_v1.4$ – I/V relation

Noticeable to the I/V relations drawn at all concentrations (*fig. 41*) is the virtual overlapping of sweep points thus showing a minor effect of AA43279 on $Na_v1.4$'s voltage-dependent elicited currents. Only the -40 mV and -30 mV sweeps at respectively 10 µM and 3 µM can be found displaced, which indicate the minor MPI increases reported in the above section.

Relatedly to $Na_v1.1$, for $Na_v1.4$ no net Na^+ currents were elicited from -120 to -60 mV, with the first channel activations occurring at -50 mV. The highest I vs. V relation is again reached between -30 and -20 mV, and it precedes the characteristic linear conductance phase of positive potentials.

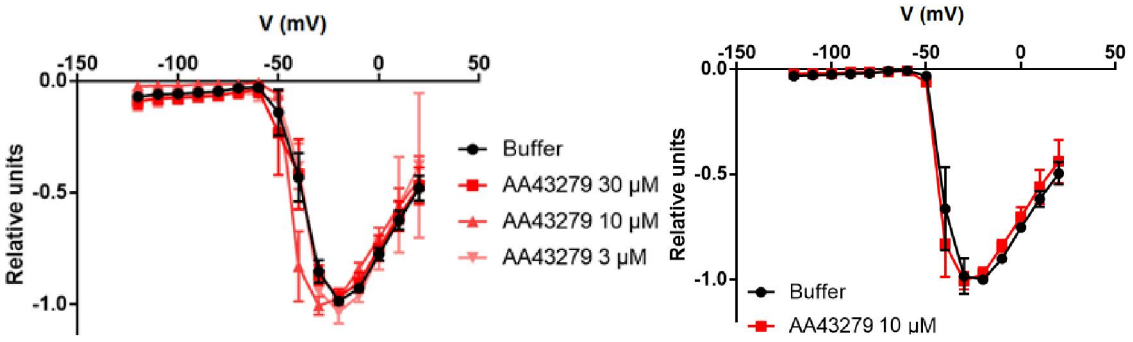

Fig. 41. Left: I/V plot normalized at -20 mV for buffer (1, black) with all AA43279 concentrations (degrees of red). Right: representative I/V plot at 10 µM AA43279, and a maximum peak at -20 mV. RUs are in intensity units

In the -30 mV sweep, a recorded current of up to -9715 pA under buffer was increased slightly with a 10 µM AA43279 application to -9771 pA, the highest current recorded in this project.

3.2.2.1.5. - $Na_v1.4$ – Activation

The first $Na_v1.4$ channel fraction became conducting at -50 mV, with the successive channels opening exponentially until -10 mV, for both buffer and the 3 AA43279 concentrations applied. Data at 0 mV and beyond is omitted due to abnormal conductance decreases into negative values (*fig. 42*).

In accordance to previous $Na_v1.4$ data, an almost total overlap for the buffer and AA43279 curves is observed for all the experiments, except for the "upward shift" in conductance noticed between -30 mV and -10 mV with 30 µM AA43279. This is directly translated into the concomitant rise in MPI and AUC previously reported for this concentration.

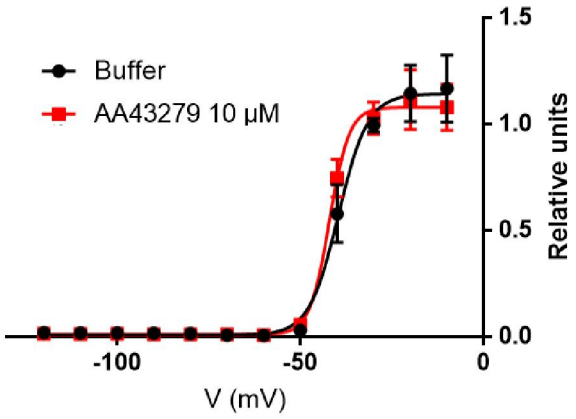

Fig. 42: representative SSA plot at 10 µM AA43279, fitted to the Boltzmann equation. Positive values past 0 mV were omitted due to excessive conductance abnormalities. 30 and 3 µM were omitted due to inconsistent values. RUs are in conductance units

The average of all V_{50act} for $Na_v1.4$ situated at -34 mV under control conditions. After 30 µM and 3 µM AA43279 applications, these voltages shifted to -37 mV and -35 mV respectively, showing a minor, earlier activation threshold.

3.2.2.1.6. - $Na_v1.4$ – Inactivation

Nearly overlapping plots can be seen for the 3 different AA43279 concentrations employed. The maximum currents elicited from the -120 and -100 mV voltages to -10 mV, start their decay phase at -90 mV (Δ-10 mV sooner than $Na_v1.1$) and finish at -50 mV. Lastly, no net current is produced from -40 mV towards positive potentials (*fig. 43*). Tiny leftward shifts can however be noticed in the decaying slopes of the 30 µM and 10 µM AA43279 applications, but such effect was not experimentally translated into narrower, nor faster inactivation of AUCs in $Na_v1.4$-elicited currents.

Two opposite effects observed at the -110 mV to -10 mV step, include the most conducting cell eliciting a -8778 pA baseline which increased to -8914 pA, and the second most conducting cell reducing its peak intensity from -6173 to -5718 pA, both cells under 10 µM AA43279.

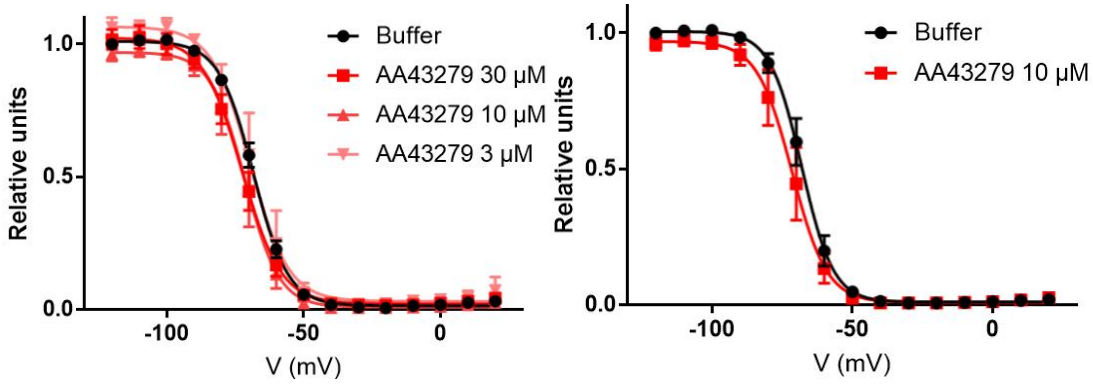

Fig. 43. Left: SSI plot normalized at -20 mV for buffer (1, black) with all AA43279 concentrations (degrees of red). Right: representative SSI plot at 10 µM AA43279, and a maximum peak at -100mV. Plots were fitted to the Boltzmann equation. RUs are in intensity units

Average $V_{50_{inact}}$ were robustly obtained at -68 mV under control conditions, and decreased to more negative potentials the higher the AA43279 concentration was: 3, 10 and 30 µM caused a progressive decrease from -69 mV through -71 mV and to -72 mV. This indicates the mode of action of AA43279 on $Na_v1.4$ reduces the conductance produced by secondary immediate activations (SSIs) of $Na_v1.4$.

3.2.3. - Endogenous currents in control cells

Small Na^+-like elicited currents, ranging from -400 pA to an observable minimum of -20 pA (*fig. 44*), were repeatedly recorded both in non-transfected HEK293 cells, control-transfected cells with eGFP, transfected products without expression (E12, see section *3.9. qPCR*) and with non-functional channels (split-reconstituted channels and chimeras). They were also reported in $Na_v1.4$-transfected cell cultures confirmed as current-positive. A postulated hypothesis of constitutively expressed channels led to electrophysiological analyses of control, unmodified HEK cells.

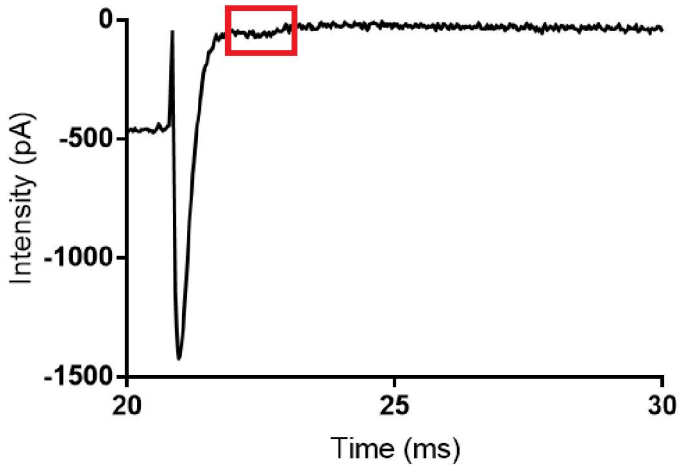

Fig. 44: smallest endogenous current (red box) of a -20 pA difference regarding baseline. The peak to its left is the artificial transient capacitance applied for depolarization

3.2.3.1. - Endogenous currents – patch-clamp

ECs were observed in 2 non-transfected cells (n = 2) with intensities of -45 pA and -160 pA, being elicited 1.2 ms after depolarization in *Step* protocols, and featuring a Na_v-like curve shape. The addition of 30 µM AA43279 caused both a noticeable MPI increase to -260 pA (*fig. 45*), and the retardation of the curve's rapidly-inactivating phase subsequently broadening its AUC, expected to happen in AA43279-sentitive Na_v channels. *IV* protocols showed a maximum activation of these currents between -30 and -20 mV, keeping close MPI values to the ones reached in *Step* protocols (*not shown*). Application of 100 nM TTX resulted in a partially complete disappearance of these currents (*fig. 45*). Another 2 cells, transfected with just eGFP as a control, produced currents of -100 pA and -200 pA, but no AA43279 testing was performed.

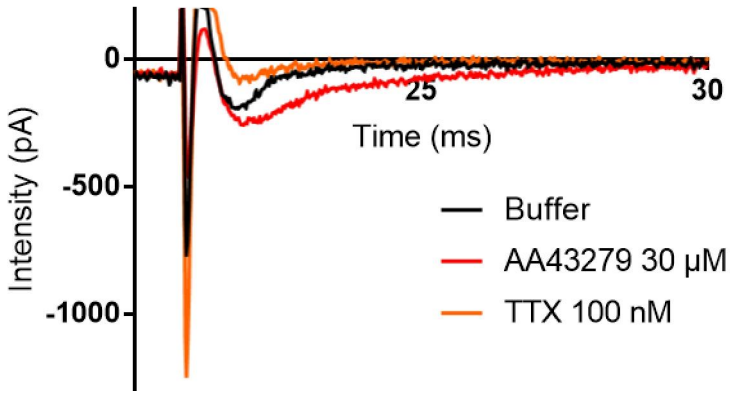

Fig. 45: ECs elicited in a non-transfected cell, subjected to AA43279 (red) and TTX (orange)

These observations altogether suggest that a sodium channel from the Na_v family could possibly be expressed in HEK cells, eliciting small Na^+ flows through it during electrical stimulations. The properties of these endogenous currents are briefly analyzed in the discussion section *4.4.* and subsections.

3.3. - Transfection of sfGFP constructs

Prior to the sfGFP-tagging of K_v and Na_v domains, experiments were performed to verify the functional interaction between the two parts of the sfGFP molecule when bound to one different intracellular target each. Two simpler molecules were chosen: a single-helix transmembrane construct (FLAG-TAC) C(t)-tagged with sfGFP11 (section *3.4.* and subsections), and a CD4 protein C(t)-tagged with sfGFP1-10. However, due to the impossibilities on correctly cloning the CD4 construct, this was replaced with the soluble sfGFP1-10 part alone.

3.3.1. - Absence of sfGFP emission with C(t)-tagged sfGFP11 constructs

Live experiments to test *in vitro* sfGFP complementation of soluble sfGFP1-10 and sfGFP11-C(t)-tagged TAC were negative for any observable fluorescence under epifluorescence microscopes (*not shown*). To test whether a hypothetical lack of expression of either tagged construct was the issue, TAC-sfGFP11:sfGFP1-10 DNA ratios were titrated from 5:1 to 2:1, 1:1, 1:2 and 1:5 (*fig. 46*). None of the mentioned titrations resulted in observable live fluorescence alike, thus suggesting that complementation did not occur with these particular constructs or that one or both did not express well.

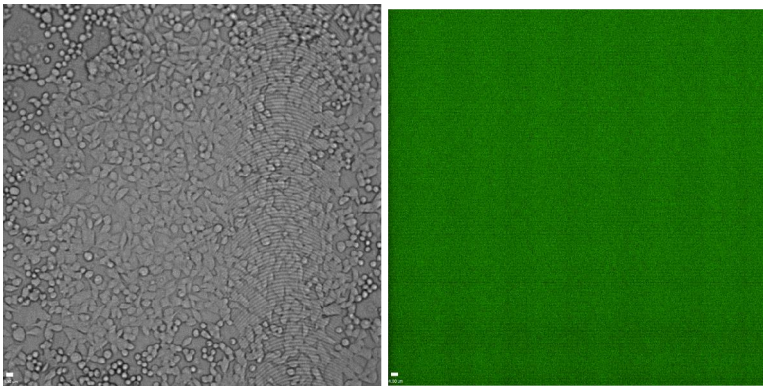

Fig. 46: 40x view of HEK cells co-transfected with TAC-sfGFP11:sfGFP1-10 in a 5:1 ratio. Left: DIC visible channel. Right: green channel with λ = 488 nm excitation (uncontrasted). Bar indicates 4 µM

3.3.2. - Detection of FLAG-TAC and sfGFP1-10 by antibody staining

To address whether the lack of fluorescence was related to the latter, the expression of the TAC construct was examined by antibody staining of the highly antigenic FLAG tag on the N(t) of the construct. Located on the extracellular side of the cell membranes and highly trafficked there through the ER-Golgi pathway, said construct can be observed as tiny dots or bigger clumps (*fig. 48*) in the green channel (λ = 488 nm, pictures not shown) by secondary staining with an Alexa 488 antibody (see Methods section).

The sfGFP1-10 protein was stained with an Alexa 488 antibody (Methods section *Fixation and antibody staining*) and detected in the green channel (λ = 488 nm). Due to the soluble nature of sfGFP1-10, a cytoplasmic spread with no specific localization in any cell compartments (*fig. 47*) was observed.

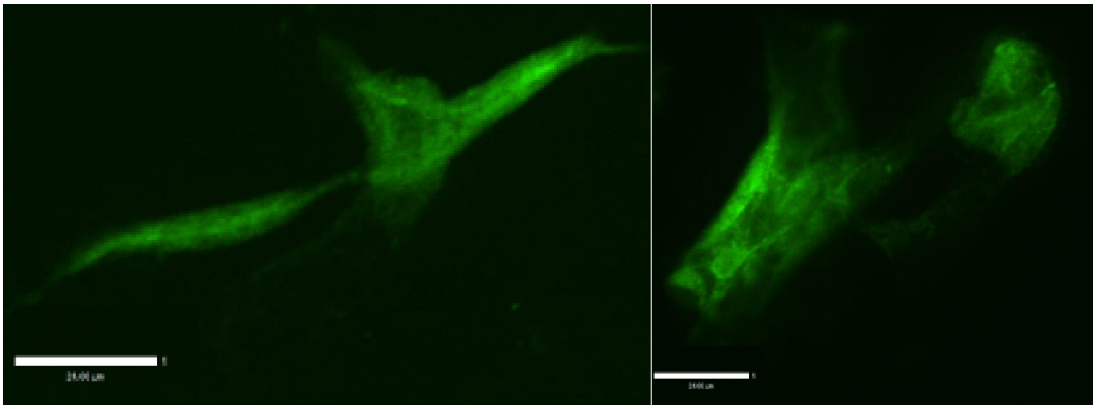

Fig. 47. Secondary staining of a primary labeling of sfGFP1-10, showing its distribution. Magnification is 100x, bar indicates 24 µM

When both molecules were co-detected simultaneously, an Alexa 568 secondary antibody was used to stain the FLAG-TAC construct in the red channel (λ = 568 nm), while Alexa 488 was kept for sfGFP1-10. But despite the intracellular production of both constructs a co-localization was non-existent (*fig. 48*). In either case, these experiments verify that both constructs are expressed and that the lack of fluorescence likely relates to incomplete complementation.

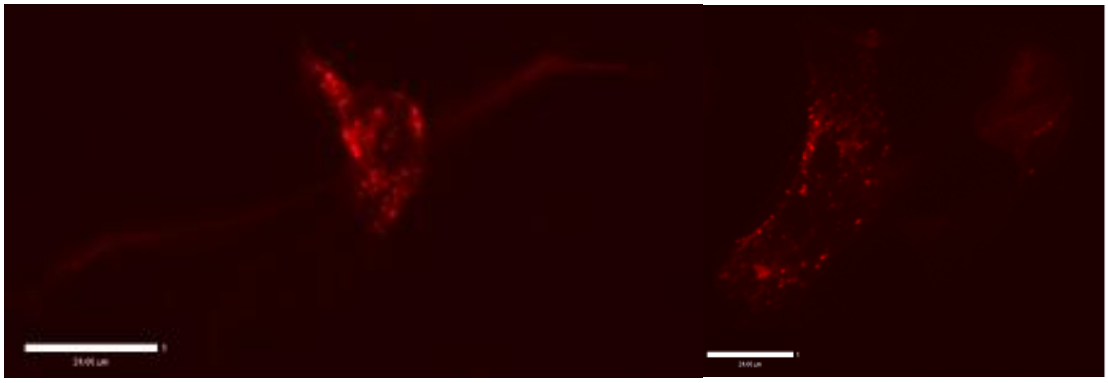

Fig. 48. Secondary staining of a primary labeling of FLAG-TAC, showing its distribution. Magnification is 100x, bar indicates 24 µM

3.3.3. - Verifiable sfGFP emission with N(t)-tagged constructs

We hypothesized that the location of the sGFP11-tag could putatively be an explanation and a N(t) sfGFP11-tagged β-actin was therefore employed for the verification of an orientation-dependent complementation for sfGFP proteins. Indeed, upon co-transfection with soluble sfGFP1-10, fluorescence was observed localized around the cytoplasm in cytoskeleton-like fibers outside the cell nuclei (*fig. 49*), suggesting a complementation of the free sfGFP1-10 molecule with the N(t)-actin-bound sfGFP11. Furthermore, an additional titration experiment of 3:1, 1:1 and 1:3 for the sfGFP1-10:sfGFP11-actin relation determined the most fluorescent concentration ratio to be - at least - 3:1 (*fig. 50*). After confirmation of the correct orientation dependence for sfGFP-tagged products, all following constructs were N(t)-tagged for sfGFP11 including the $K_v2.1$ monomers and $Na_v1.1/1.4$ dimers.

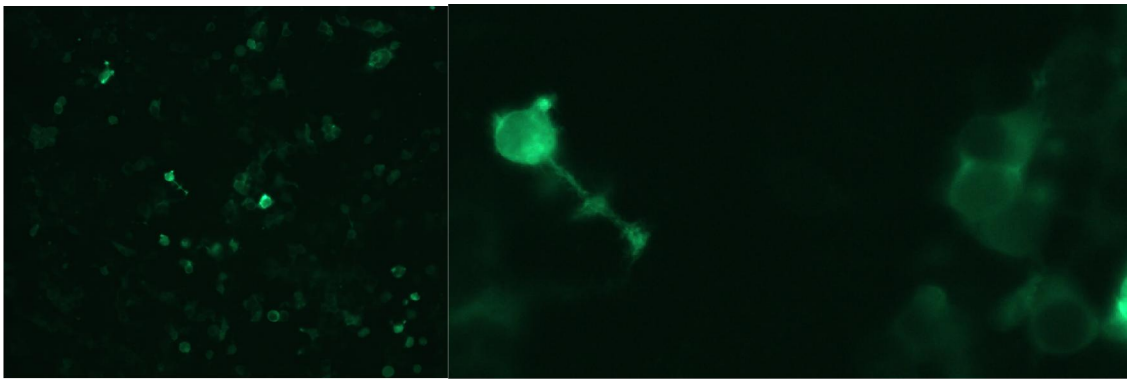

Fig. 49. Left: 40x image in the green 488 channel. Right: close-up of the center of the picture

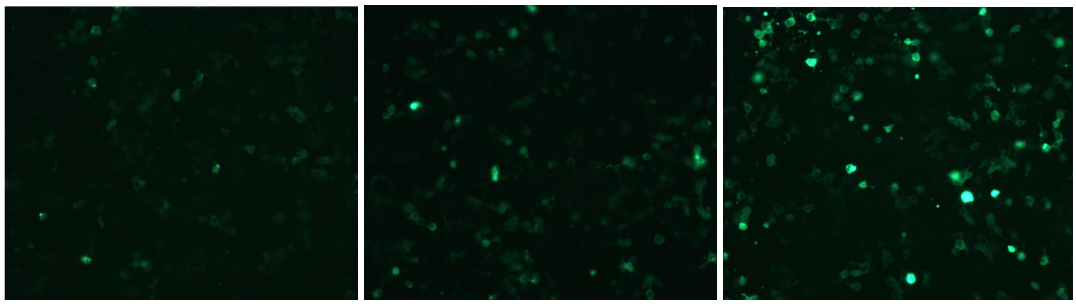

Fig. 50: co-transfection of sfGFP1-10:sfGFP11-actin in 1:3 (left), 1:1 (center) and 3:1 (right) ratios. Magnification is 40 x

Negative-control experiments were also made to confirm the absence of fluorescence produced by either part of sfGFP alone. Cells transfected with only sfGFP1-10 or sfGFP11-actin were imaged (*fig. 51*) and no other emissions were determined apart from residual cell autofluorescence. Bound sfGFP1-10-sfGFP11 were observable from 40x through 100x objectives.

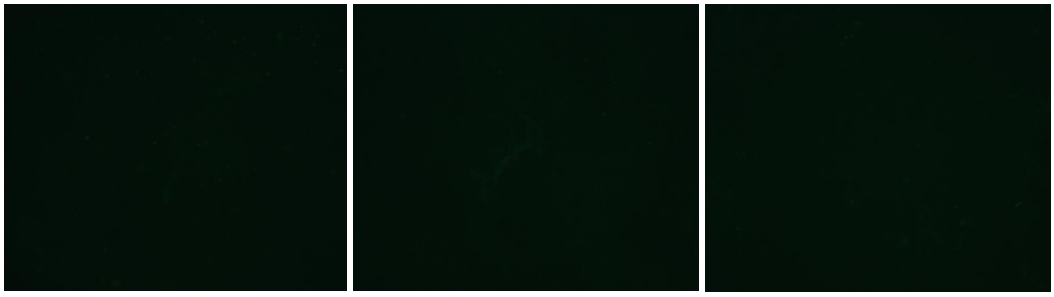

Fig. 51: controls with sfGFP1-10 (left) and sfGFP11-actin (center) alone. Right: control untransfected cells. Magnification is 40x

Very dim emissions, small and round in size can also be noticed if no actual fluorophores are present (*fig. 51* above, *right*). These actually belong to the cells' autofluorescence, and must not be confused with real fluorescence. Quick shifts between visible, green, red or other channels can reveal the cells' unspecific light absorption enabling to be disregarded as such.

Positive-control experiments with eGFP were always included due to its high expression within minimal incubation time and success in a 96% of transfections (26/27). eGFP-induced fluorescence was the brightest among the rest of fluorophores and far surpassed sfGFP-induced emissions (*fig. 52*). eGFP was visible from objectives 5x through 100x in the green channel (λ = 488 nm).

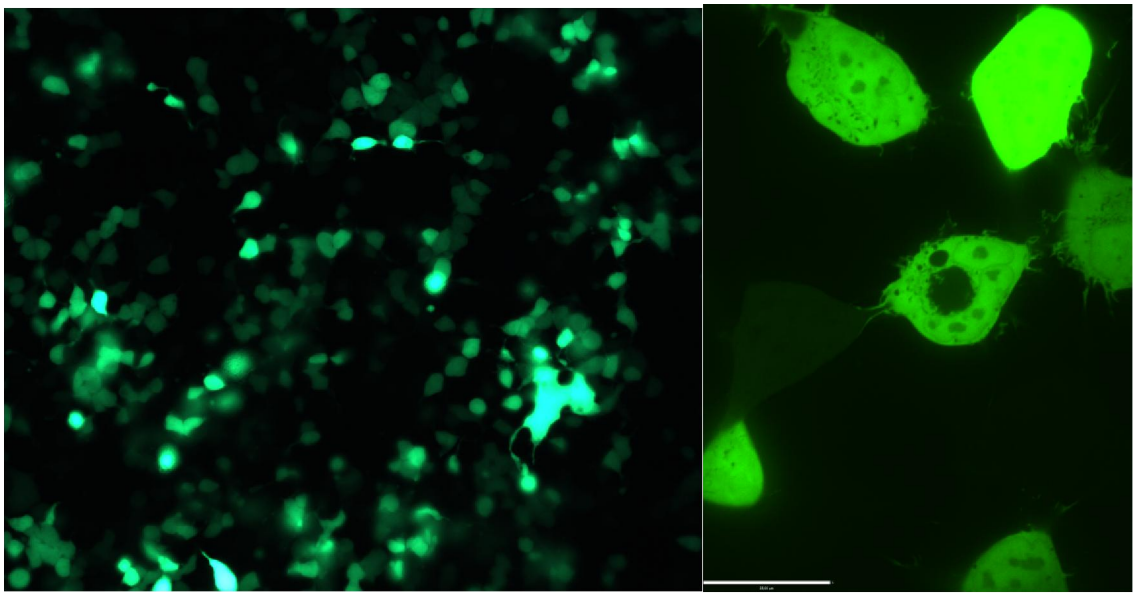

Fig. 52. 40x picture of eGFP under confocal (Zeiss, left) and 100x picture under spinning disk (Hamamatsu, right) microscopes, bar indicates 24 µM

Co-transfections with eGFP were also performed for detection of transfected cells with non-fluorescing channels ($Na_v1.4$), and with sfGFP-tagged dimers after a lack of fluorescence was assessed (*Modular approach* sections *3.6 – 3.8*).

3.3.3.bis - Autofluorescence of damaged cells and debris

A common phenomenon repeatedly observed were membrane-damaged and apoptotic cells giving strong fluorescence in the GFP channels. Such were found both in control wells (with control DNA and untransfected) and test wells for fluorescence, where they were harder to discriminate. A quick comparison between excitation lasers and visible light (*fig. 53*) clearly showed an unhealthy morphology, or their position out of focus, for such pretendedly "positive" cells. Debris and other microscopical impurities also produced strong emissions in any laser channel and were discarded the same way.

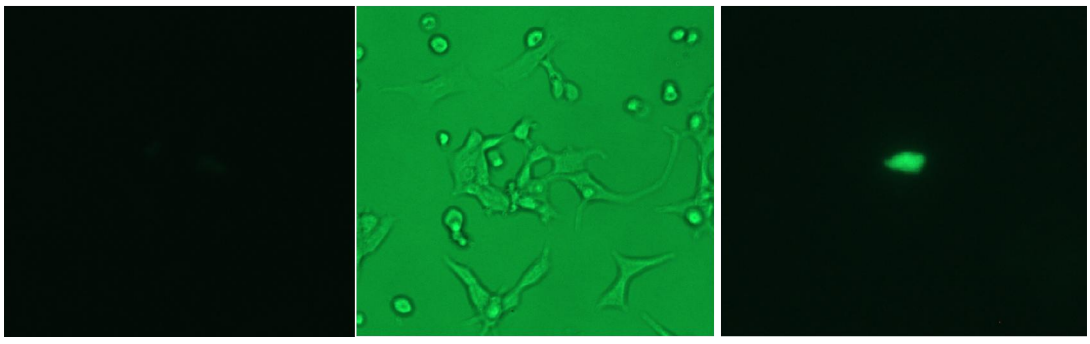

Fig. 53: dim cells in a single frame under the green (left) and visible (center) channels, revealed to have an "splat" morphology. Right: debris emitting strong green autofluorescence

3.4. - Cloning of sfGFP tags into constructs

Cloning techniques were employed for the addition of C(t)-sfGFP1-10 and N(t)-sfGFP11 to the inserts of interest. A pcDNA3.1-sfGFP1-10 vector (from GenScript, *fig. 54*), with the GFP strands 1-10 downstream in the multiple cloning site (MCS) was digested with the same pair of restriction enzymes for each insert, to later have the cohesive ends ligated between the two. The resulting constructs were consequently 699 bp (233 aa) heavier in size than the original inserts (*fig. 54*).

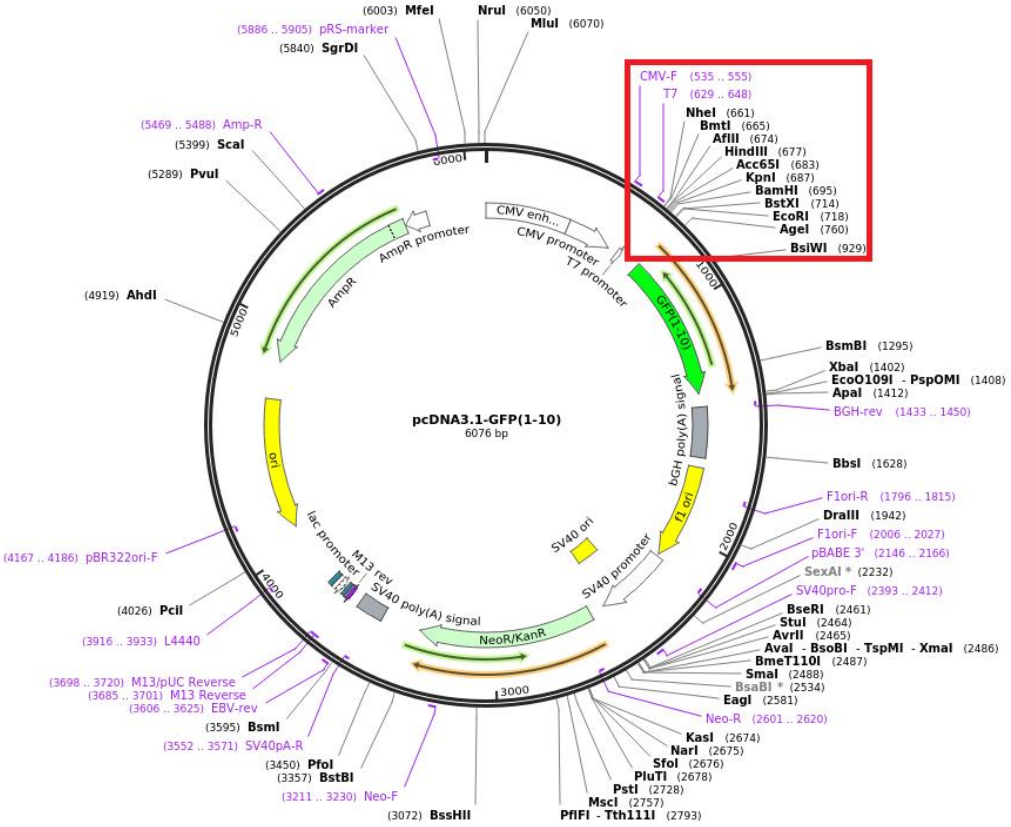

Fig. 54: molecular map of the pcDNA3.1-sfGFP1-10 vector with its MCS (red box)

The 11th GFP strand, of only 17 residues, was added by a directed-amplification strategy in PCR with flanking, custom primers. The forward primers (approximately 23-28 bp in length) were added the 51 bp-long sequence of sfGFP11 to their 5' end. Furthermore, an upstream restriction site of our choice was added with a 6 nt-long palindromic sequence (*fig. 55*). These designed primers *in silico* were then synthesized (Eurofins Genomics).

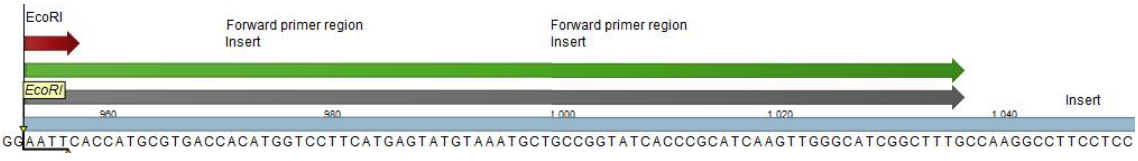

Fig. 55:example of a sfGFP11 N(t)-tagging. From 5' to 3': Primer and its binding region (green and grey arrows) includes the enzyme restriction site at the 5' (red arrow) and the rest of the sfGFP11 sequence (down to its 3')

Construct	Insert (CDS) origin	Vector base	Amplification success	Transformation success	Large-scale success	Expression success (qPCR)	Functionality
FLAG-TAC	*IL-2R* + rat *SCN2A* + sfGFP	M1 pcDNA3.1^{AmpR}	Yes	Yes	Yes	Yes	Yes
CD4	Human *CD4* + sfGFP	M1 pcDNA3.1^{AmpR}	No	No	No	No	No
sfGFP1-10	sfGFP	pcDNA3.1^{AmpR}	Yes	Yes	Yes	Yes	Yes
sfGFP11-Actin	sfGFP + Human *ACTB*	peGFP^{KanR}	Yes	Yes	Yes	Yes	Yes
peGFP	eGFP	peGFP^{KanR}	Yes	Yes	Yes	Yes	Yes
E12 (own)	Mouse *SCN1A*	pcDNA3.1^{AmpR}	Yes	No	No	No	No
E12 (GenScript)	Mouse *SCN1A*	pcDNA3.1^{AmpR}	Yes	Yes	Yes	No	No
E34	Mouse *SCN1A*	pcDNA3.1^{AmpR}	Yes	Yes	Yes	Yes	No
F12	Human *SCN4A*	pcDNA3.1^{AmpR}	Yes	Yes	Yes	Yes	No
F34	Human *SCN4A*	pcDNA3.1^{AmpR}	Yes	Yes	Yes	Yes	No
E3F4	*SCN1A* + *SCN4A*	pcDNA3.1^{AmpR}	Yes	No	No	No	No
F3E4	*SCN1A* + *SCN4A*	pcDNA3.1^{AmpR}	Yes	Yes	Yes	Yes	No
E123-LE-4 (Ch #0)	*SCN1A* + *SCN4A*	pcDNA3.1^{AmpR}	Yes	Yes	Yes	Yes	No
E123F4 (Ch #1)	*SCN1A* + *SCN4A*	pcDNA3.1^{AmpR}	Yes	Yes	Yes	Yes	No
E123 F4 VSD E4PFD (Ch #2)	*SCN1A* + *SCN4A*	pcDNA3.1^{AmpR}	Yes	Yes	Yes	Yes	No
K_v-sfGFP1-10	Rat *KCNB1* + sfGFP	pcDNA3.1^{AmpR}	Yes	Yes	Yes	Yes	Yes
sfGFP11-K_v	Rat *KCNB1* + sfGFP	pcDNA3.1^{AmpR}	Yes	Yes	Yes	Yes	Yes

Table 4. List of all cloning constructions performed in this project

3.4.1. - Impossibility to clone $Na_v1.1$D1D2-sfGFP1-10

Only one construct in this project resulted impossible to be produced by own production within our facilities. Domains I and II of *SCN1A* were successfully amplified by PCR, digested along with pcDNA3.1-sfGFP1-10, and ligated (*fig. 56*). However, no competent cells could be transformed with this construct and large-scale production was thus deemed unreachable.

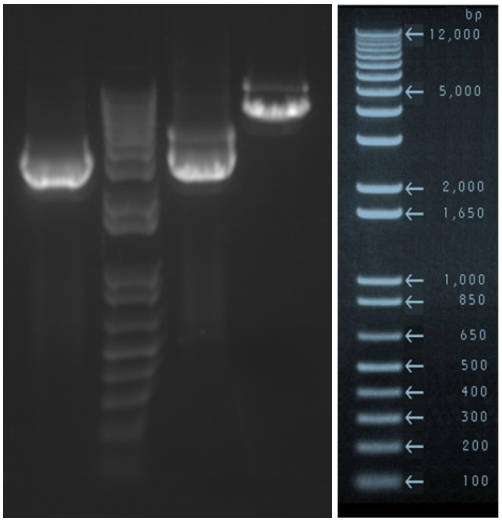

Fig. 56. Left: PCR (lane 1) and digest (3) of $Na_v1.1$D1D2, vector digest (lane 4). Right: schematic of the 1 kb ladder used (Invitrogen)

Due to this difficulty, cloning said construct was outsourced (GenScript, *fig. 57*), but numerous difficulties in the process were also reported. Among them, random point mutations, instability during synthesis, and contamination with gDNA posed a problem before an acceptable QC purification was achieved.

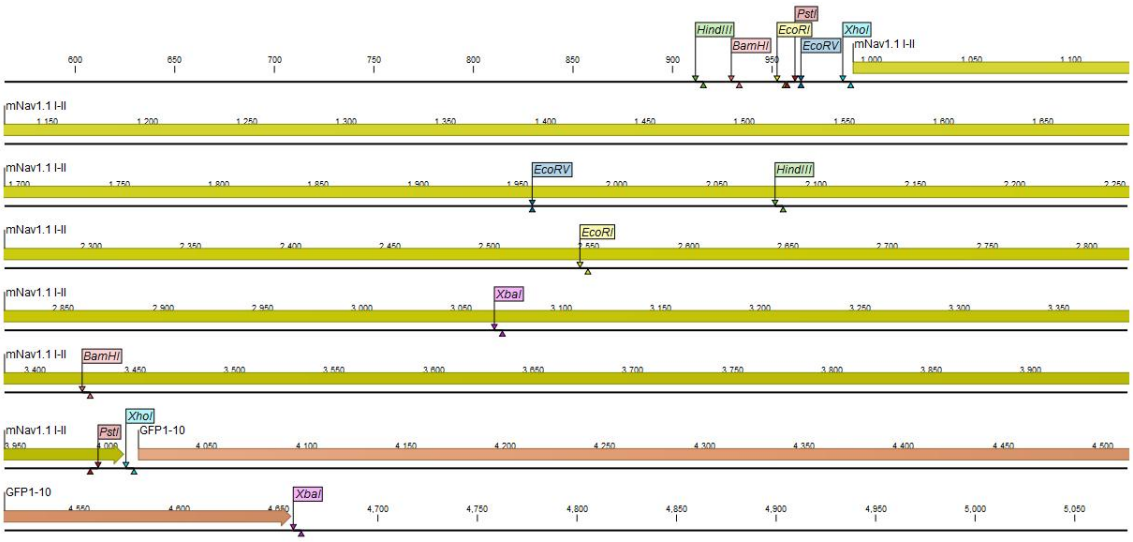

Fig. 57: schematic of the 5'-$Na_v1.1$D1D2-sfGFP1-10-3' insert (yellow arrow for $Na_v1.1$D1D2, red arrow for sfGFP1-10) within the pcDNA3.1+ vector

In the end, the large-scale construct provided neither even achieve to be expressed in sufficient mRNA levels (see section *3.9. qPCR*). Therefore, co-transfections with this construct and its respective D3D4 counterpart only resulted in the latter being virtually produced.

3.5. - K_v2.1: K_v-sfGFP + sfGFP-K_v

As a proof-of-concept to test a live functionalization of sfGFP-tagged channels, experiments were designed with simpler K_v2.1 monomers to be cloned with sfGFP into expression vectors.

HEK cells were co-transfected with the N(t)-sfGFP11-K_v2.1 monomer and either soluble sfGFP1-10, or with the K_v2.1-sfGFP1-10-C(t) monomer (*fig. 58*). Successfully expressing cells were visually detected at 10x and 20x by *in situ* sfGFP fluorescence, and subject to patching. Their elicited K^+ currents were analyzed under a *modified IV* protocol (*fig. 59*) every minute. *Step* protocols were not performed as the effects in applying K_v-specific modulators or toxins were not sought in K_v2.1. However, and out of curiosity, the applications of 3 µM AA43279 and 100 nM TTX were tested in K_v-sfGFP + sfGFP-K_v cells with no effect at all.

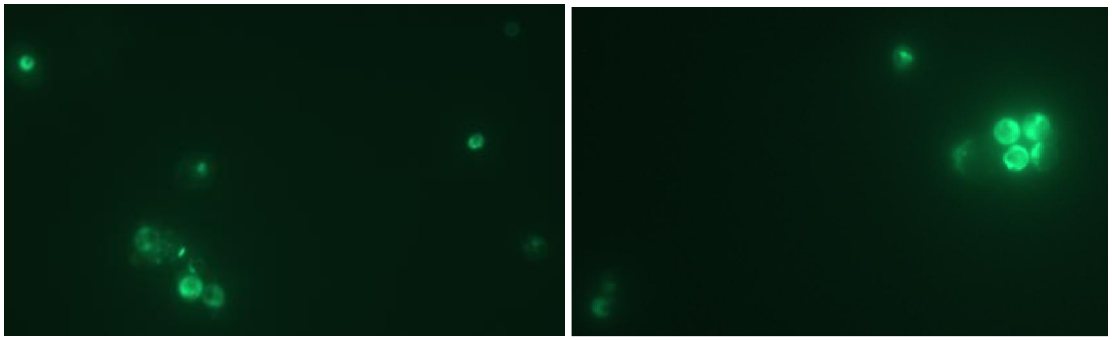

Fig. 58: 40x images of sfGFP11-Kv + sfGFP1-10 soluble (left), and Kv-sfGFP1-10 + sfGFP11-Kv (right)

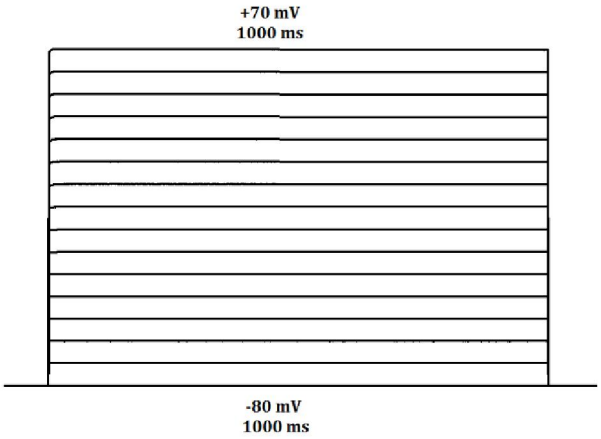

Fig. 59: *modified IV* protocol for VGKCs. Each sweep represents a +10 mV increment

3.5.1. - K_v2.1: K_v-sfGFP + sfGFP-K_v – MPI

Very intense MPIs were characteristic of K_v2.1-transfected cells, with the highest voltage sweeps normally generating currents of > +20000 pA that exceeded Clampex's sensitivity threshold (*fig. 60*). From a -80 mV holding potential, K_v2.1 activated at around -30 mV (red sweep), becoming more conducting the higher the voltage applied, up to +70 mV. K_v2.1 channels completely inactivated back at -80 mV after the cessation of depolarizing stimuli.

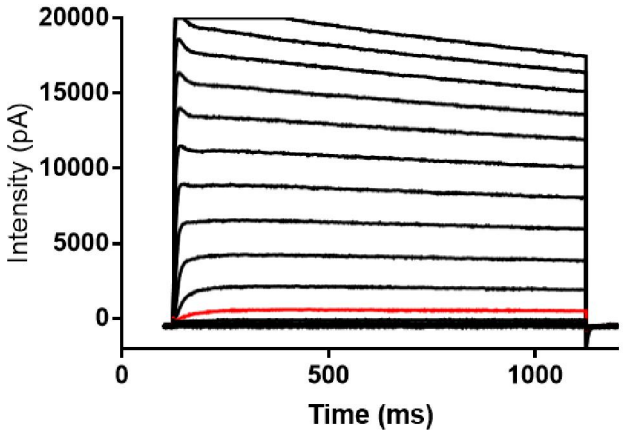

Fig. 60 (modified from fig. 23): I/V relation of an sfGFP-tagged K_v channel (K_v-sfGFP1-10 + sfGFP11-K_v). The first sweep eliciting activation (-30 mV) is displayed in red

The K^+ currents above showed match in morphology with K_v2.1-elicited curves in previous bibliography[69, 70].

3.5.2. - K_v-sfGFP + sfGFP-K_v – I/V relation

I/V relations for K^+ channels usually consist on one monophasic linear (or slightly curved), increasing slope, due to their proportional voltage-dependent conductance (*fig. 61*). For K_v2.1, such relation can be observed in the current values excluding the -80 - -40 mV region (without activation) and the +60 mV sweeps onwards (where the recording threshold is reached).

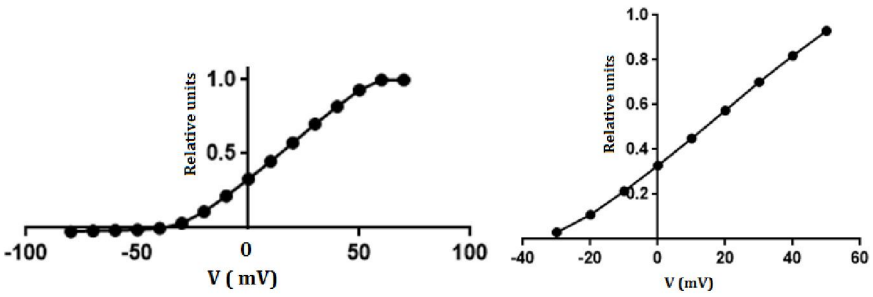

Fig. 61: I/V relation of the sfGFP-tagged K_v channel from -80 to +70 mV (left), and linear trend of the same I/V plot (right, just displaying the -30 to + 60 mV range). RUs are in intensity units

Settings and protocols specifically designed for VGKCs can apply depolarizations of up to +80 mV and measure their currents elicited without sensitivity limitations[71].

3.5.3. - sfGFP11-K_v2.1 monomer alone

Due to the tetramerizing nature of the *KCNB1*-encoded monomer, a simultaneous co-transfection of both sfGFP1-10-tagged and sfGFP11-tagged constructs was not exclusively necessary for channel functionality. Co-expression of N(t)-sfGFP11-K_v2.1 with the soluble sfGFP1-10 was enough to detect fluorescent complementation and analyze K^+ currents on transfected cells.

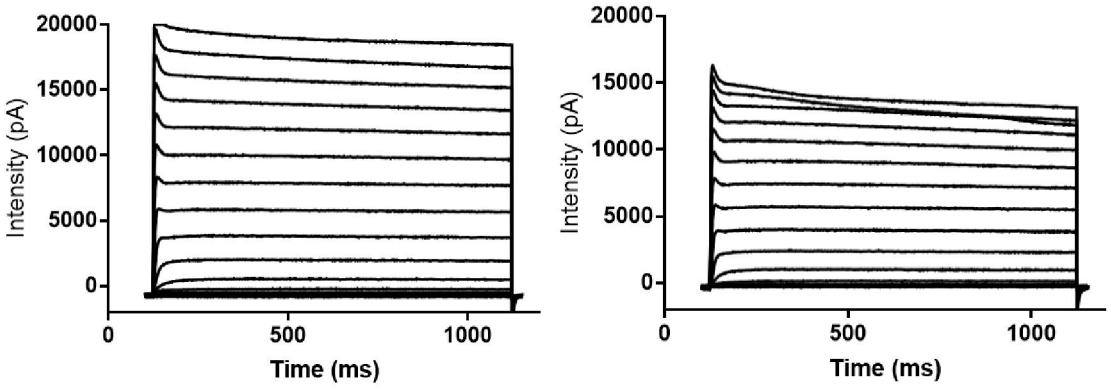

Fig. 62: first (left) and fifth (right) consecutive depolarizing protocols of the same sfGFP11-K_v2.1 cell

Figure 62 above depicts a K^+ current of tetramerized sfGFP11-K_v2.1 monomers (with bound sfGFP1-10), with the closest $V_{1/2}$ represented in the red sweep (+10 mV), in the first and fifth consecutive protocols. An effect of decrease in the MPI for K^+ is observed the more depolarizations applied.

3.5.4. - K_v2.1-sfGFP1-10 monomer

The properties of the K_v2.1-sfGFP1-10 constructs alone were not tested *per se*, but tested along with sfGFP11-K_v2.1 (subsections *3.5.1.* and *3.5.2.* above).

3.5.5. - sfGFP-K_v2.1 – Microscopy

K_v2.1 monomers tagged with sfGFP11 and sfGFP1-10 were co-detected as fluorescent clusters in the cell membrane of HEK cells (*fig. 64*). In accordance to previous research, agglutination into clusters is a characteristic feature of K_v2.1 channels in neuronal membranes as revealed by GFP staining[69, 72, 73]. Furthermore, a previous experiment was done co-transfecting soluble sfGFP1-10 with the sfGFP11-K_v2.1 monomer, in 3:1, 1:1, and 1:3 ratios. All titrations were equally visualized both in relative fluorescence brightness and number of cells lit (*fig. 63*, also see Discussion section *4.6*).

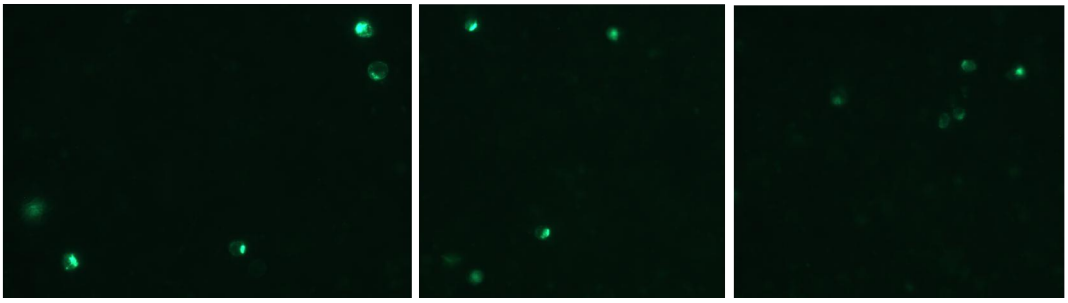

Fig. 63: titration experiments with soluble sfGFP1-10 + sfGFP11-K_v2.1 in 3:1 (left), 1:1 (center) and 1:3 (right) ratios

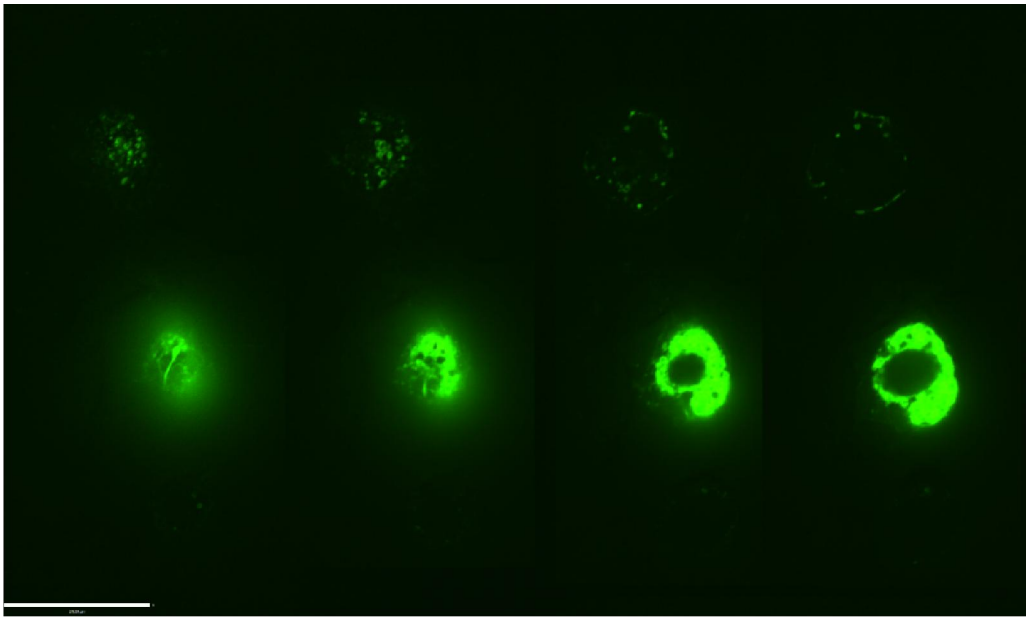

Fig. 64: stacked 4-image series at 100x of co-transfected K_v-sfGFP-sfGFP-K_v cells. Bar indicates 24 µM

Thus, these experiments altogether reveal that the K_v2.1 monomers have been successfully sfGFP-tagged, trafficked into the cell membrane abundantly to be visualized, and retain their functional electrophysiological activity. Autofluorescence of the sfGFP1-10-tagged or sfGFP-11-tagged K_v2.1 monomers was discarded likewise (*fig. 65*).

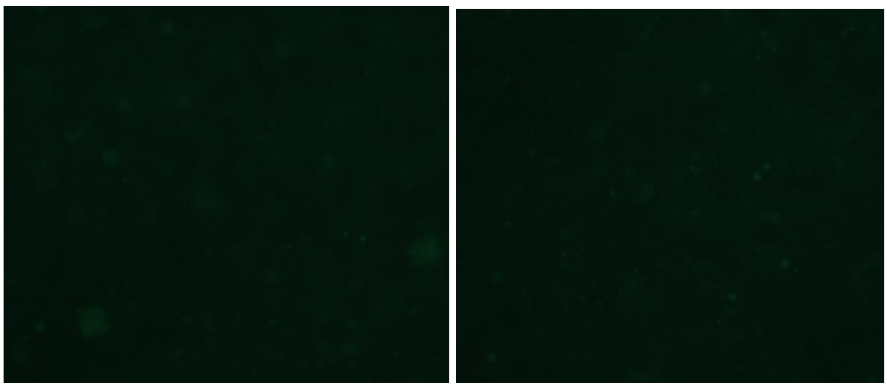

Fig. 65: dim autofluorescence of cells transfected with K_v-sfGFP1-10 (left) and sfGFP11-K_v (right)

3.6. - Modular approach

Upon the successful results obtained with the sfGFP-tagged K_v2.1 monomers, the properties of sfGFP-tagged Na_v1.1 and Na_v1.4 dimers were tested. The next sections depict the characteristics of the cells expressing channel dimers alone, prior to the co-transfections with complementary halves of the channels.

3.6.0. - Modular approach – Naming system: To better assimilate the reading of the tagged-dimers analyzed in the following sections, their identification has been abbreviated to a 3-character system explained in the *table 5.* below:

Construct	Isoform	Abbreviation	Domains I-II (D1D2)	Domains III-IV (D3D4)	Examples
$Na_v1.1$	1.1 -> 11	Eleven (E)	E12	E34	E12-E34, E12-F34, E123-F4
$Na_v1.4$	1.4 -> 14	Fourteen (F)	F12	F34	F12-F34, F12-E34, F3E4
sfGFP1-10 (soluble)		Soluble (Sol)			E34-Sol, F34-Sol
sfGFP11-Actin		Actin (Act)			E12-Act, F12-Act

Table 5: abbreviations for the sfGFP-tagged Na_v halves assayed in this project

As noted before, all D1D2 constructions are C(t)-sfGFP1-10 tagged, while all D3D4 dimers are N(t)-sfGFP11 tagged. This way, a co-transfection with $Na_v1.4$D1D2-sfGFP1-10 and sfGFP11-$Na_v1.4$D3D4 is simply reduced to "F12-F34". All the above dimers tested alone, not fluorescent by themselves, were always co-transfected with eGFP to enable patching by cell fluorescence. Also, after the discovery of a lack of fluorescent complementation between the sfGFP-tagged Na_v constructs (sections below), triple co-transfections with reporter eGFP were deemed necessary. Knowledgably, this increased the risk of not finding cells that had been transfected with both domains I-II and domains III-IV of either channel, in addition to eGFP.

Channel	Nº cells tested	Of which successful*	Fluorescent?	MPI range (min. -max.)	Of which ECs	TTX response?** Yes/No/Partial
$Na_v1.1$	24	19	No	-800 - -6560	5	Yes
$Na_v1.4$	32	19	No	-800 - -8900	13	Yes + Partial
$K_v2.1$	4	4	Yes	> +20000	0	-
E12	10	0	No	-20 - -600	8	No + partial
F12	6	0	No	-70 - -800	5	Partial
E34	5	0	No	-30 - -95	4	Partial
E34-Sol	4	0	Very dim	-620 - -800	1	Partial
F34	5	0	No	-140 - -700	4	N/A
F34-Sol	2	0	Very dim	-20	1	N/A
E12-F12	4	0	No	0	0	N/A
E34-F34	5	0	No	-50 - -250	5	N/A
E12-E34	6	0	No	-60 - -250	5	No + partial
F12-F34	14	0	No	-20 - -300	9	N/A
E12-F34 (Co #1)	4	0	No	-50 - -200	3	N/A
F12-E34 (Co #2)	6	2?	No	-930 - -1400	4	Partial
E3F4	-	-	-	-	-	-
F3E4	8	0	-	-20 - -200	4	N/A
E123-LE-4 (Ch #0)	10	0	-	-20 - -300	8	N/A
E123F4 (Ch #1)	8	0	-	-20 - -220	6	N/A
E123 F4VSD E4PFD (Ch #2)	9	0	-	-30 - -700	9	Partial
Untransfected	2	0	No	-45 - -260	2	Partial
eGFP	2	0	Yes	-100 - -200	2	N/A

Table 6. Summary of all types of ion channels, halves, combinations and controls tested in electrophysiology experiments
*: MPIs exceeding < -800 pA ; **: yes if around 90% inhibition is reached, no if 10% or less is reached, partial if >10& and <90%

Summing up these data, clear conclusions are drawn which show no success of the sfGFP-tagging method for the Na_v halves, nor any currents elicited from them. This assumption comes from the only obtaining of low intensity currents (> -800 pA) and their partial TTX inhibition repeatedly observed, altogether pointing to an endogenous origin of these currents (ECs, see Discussion section *4.4*).

3.6.1. - $Na_v1.1D1D2$ (E12)

Control cells expressing only E12 were co-transfected with eGFP. Up to 8 cells patched (n = 10) showed little ECs (section *3.2.3. Endogenous channels in control cells*) to a total absence of current. The remaining 2 cells also elicited currents with MPIs of -553 pA and -441 pA under buffer, augmented to -601 and -479 under 30 µM AA43279 (*fig. 66*). AUCs respectively increased 2.16 and 2.31-fold, while tau values elongated 1.64 and 2.33-fold. Nevertheless, the altogether low success rate of these cells, average low MPIs below the threshold for ECs, unstable recordings with sustained leak, and no virtual mRNA expression of the E12 construct (section *3.9. qPCR*) can only situate these currents, if anything, as produced by endogenously expressed channels.

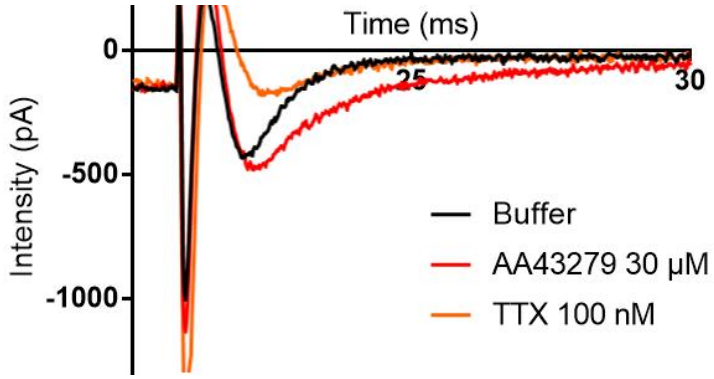

Fig. 66: low-intensity current produced by an E12-transfected cell

An antibody staining was performed with a primary antibody targeting the intracellular D1D2 loop of $Na_v1.1$ (Alomone Labs), and a secondary Alexa 488 antibody. However, the primary antibody bound unspecifically to a variety of intracellular targets following the same aggregation pattern in clumps (*fig. 67*). Adding to the lack of mRNA expression for the E12 construct, this antibody staining resulted inconclusive. Another microscopy control was performed with the co-transfection of E12 and sfGFP11-actin to detect any possible interactions between their expression pathways. The only observations among the low fluorescence yield may point to actual apoptotic cells (*fig. 68*), instead of any E12 products which expression showed negligible by qPCR.

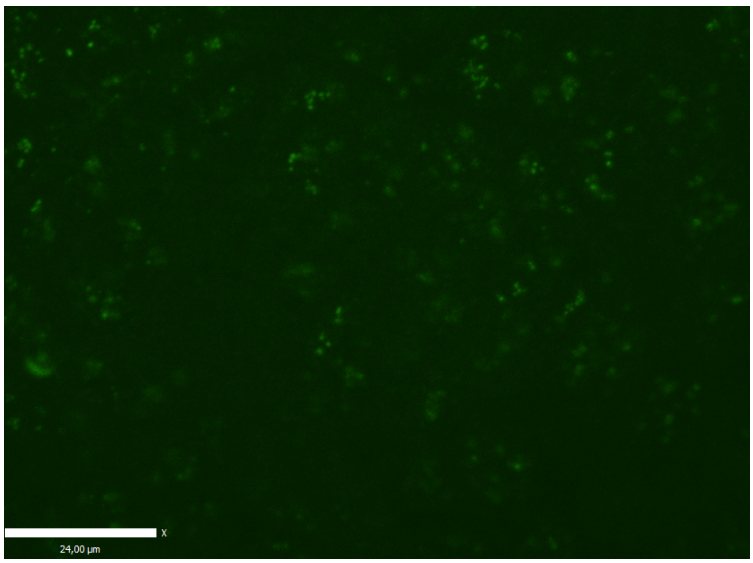

Fig. 67: unspecific staining with α-$Na_v1.1D1D2$ across cellular substructures

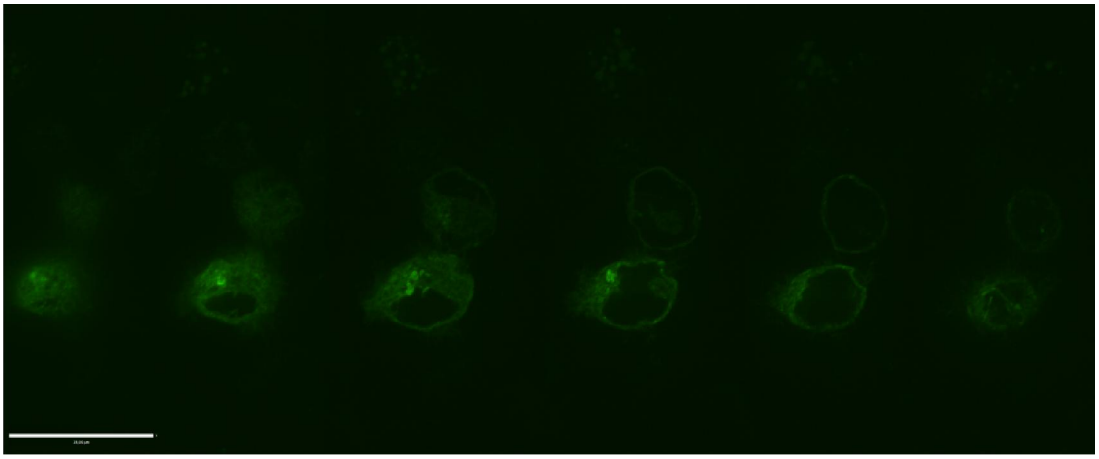

Fig. 68: stacked 6-image series of an E12-Act co-transfection. Bar indicates 24 µM

3.6.2. - $Na_v1.1$D3D4 (E34)

Control E34 cells were co-transfected with either eGFP (n = 5), or with sfGFP1-10 (n = 4) to pinpoint cells fluorescing with sfGFP. Only small ECs (> -800 pA) were recorded with considerable leak. If positive pressure was applied to counter this, currents were observed to rise between -800 pA - -1400 pA. However, the abnormal high conductance values (up to 143 pF) for the Na_v peaks fused to the transient capacitances indicate these probably are none other than magnified ECs.

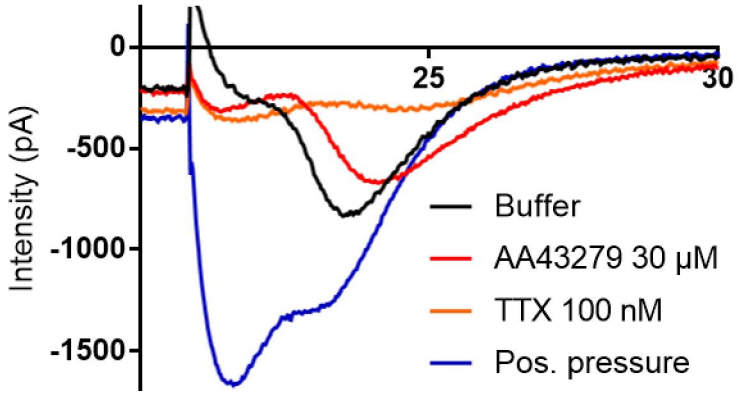

Fig. 69. Effect of positive suction to counter cell leak: a dramatic increase in conductance causes fusion of the Na_v-elicited curve to the artificial transient capacitances and gives along a false increase in MPI to the Na^+ current, making its analysis impossible.

Interestingly, and despite the very dim sfGFP fluorescence observed *in situ* in 3 E34-Sol cells, no currents were elicited (0 pA) nor no other endogenous currents were found. Co-transfection of both constructs did not achieve the expected sfGFP complementation between the intracellularly-tagged E34 in the membrane and its soluble cytoplasmic counterpart. The majority of cells were not lit despite transfected with E34-Sol. Only a 100x magnification shows an apoptotic cell (*fig. 70*) initially thought as a true positive of this interaction.

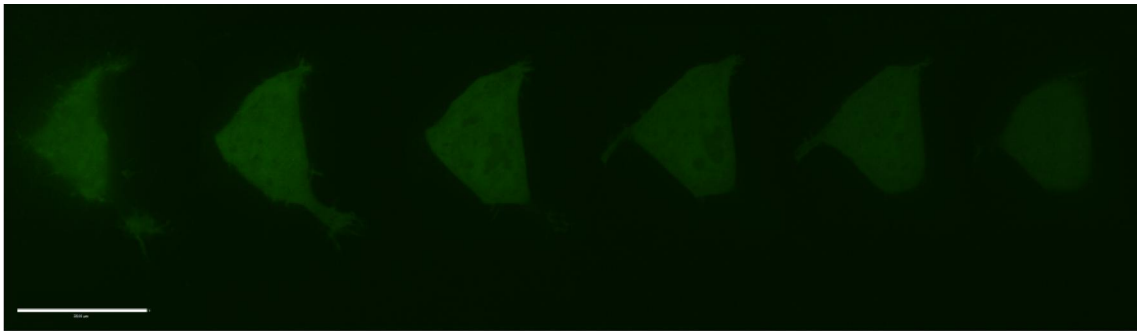

Fig. 70: stacked 6-image series of an E34-Sol co-transfection. Magnification is 100x, bar indicates 24 µM

3.6.3. - $Na_v1.4D1D2$ (F12)

Co-transfection with F12 and eGFP yielded 5 ECs (n = 6), the biggest of which either were fused to transient capacitances, or were affected with continuous leak, making any analyses impossible. Characteristic MPI losses and leak increases were produced after each IV protocols applied (*fig. 71*). Similarly to the previous section, these currents cannot be classified as F12-elicited.

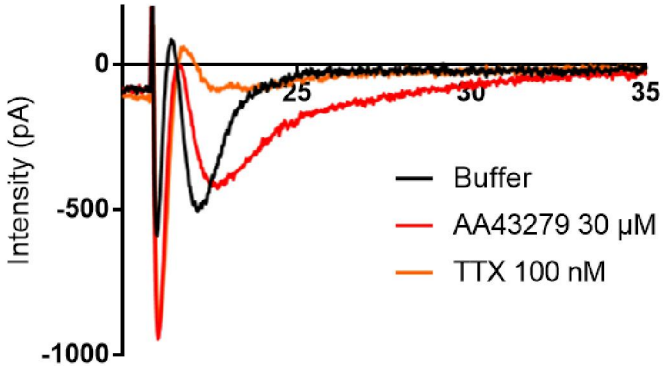

Fig. 71: low-intensity current produced by an F12-transfected cell

The primary α-$Na_v1.1D1D2$ antibody was incubated in F12-expressing cells for the detection of any possible interactions. The visualization of fluorescent clumps (*fig. 72*) identical to the ones observed with E12, stresses the unspecificity of this antibody for staining purposes. Another similar negative microscopy control was done with a F12 and sfGFP11-actin co-transfection. The lack of intracellular filamentous structures lit indicated no interaction, with the only observations belonging to artifacts in the membrane contours (*fig. 73*).

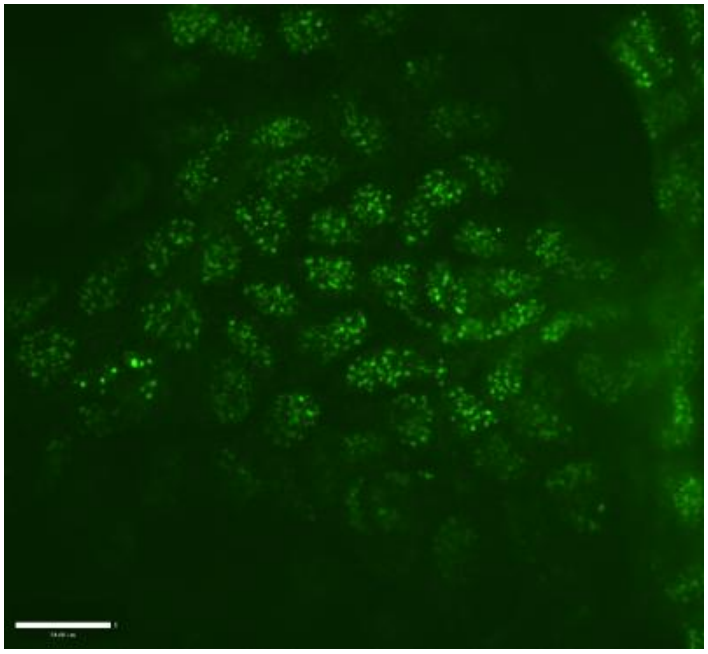

Fig. 72: unspecific staining caused by the α-Na_v1.1D1D2 primary antibody

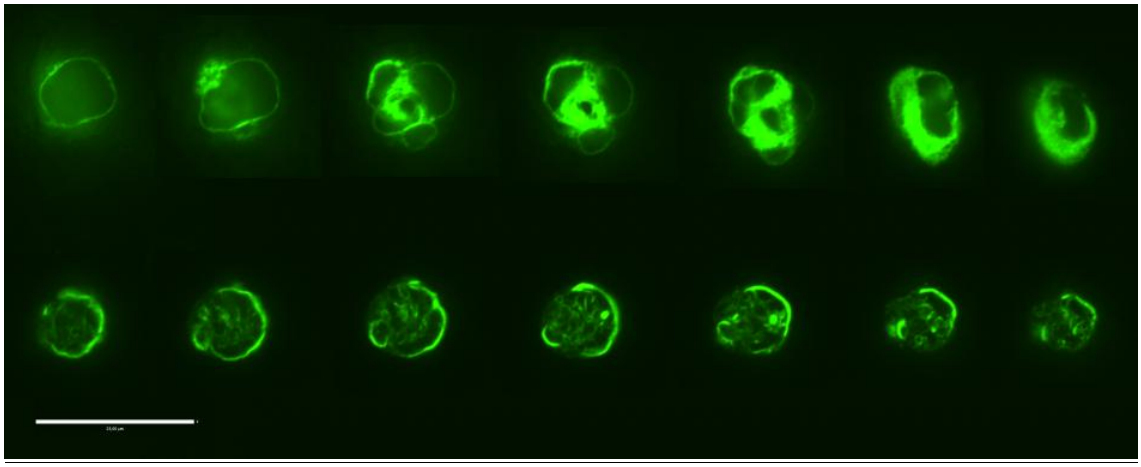

Fig. 73: stacked 7-image series of 2 cells co-transfected with F12-Act. Magnification is 100x, bar indicates 24 µM

3.6.4. - Na_v1.4D3D4 (F34)

Five cells co-transfected with F34 + eGFP and other 2 cells co-transfected with F34-Sol (n = 7) only produced ECs and absences of current. Cells with eGFP elicited -400 and -700 pA currents unrecordable past a few sweeps due to their great instability and immediate lysis. F34-Sol cells produced -20 and 0 pA despite dim, observable fluorescence *in situ*. Therefore, I/t analyses with AA43279 are TTX are unavailable. Imaging at 100x magnification despite showing fluorescent cells (*fig. 74*), their pathological morphology might indicate cell apoptosis or damage instead of – or mixed with – actual sfGFP emissions.

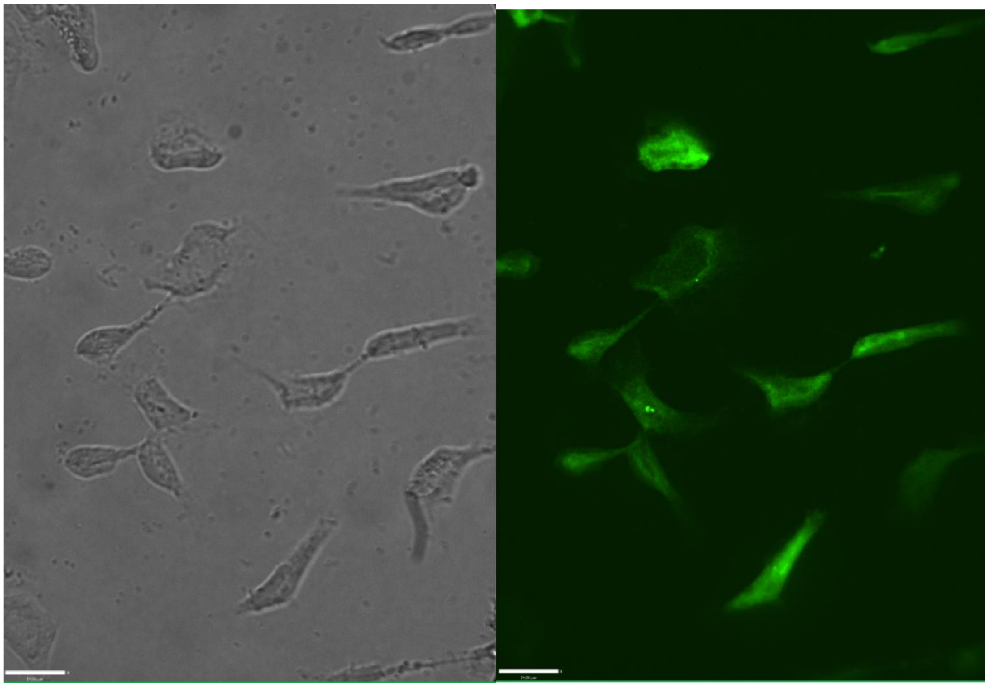

Fig. 74: cells co-transfected with F34-Sol under DIC (left) and green channel (right). Magnification is 100x, bar indicates 24 µM

3.6.5. - E12-F12

A triple co-transfection (+ eGFP) and negative control was done to detect any possible electrophysiological interactions between the E12 and F12 constructs. A total absence of current (0 pA) in all cells analyzed (n = 4) indicates no functionality of these dimeric domains with each other. Cells co-transfected with E12 and F12 produced no observable fluorescence emissions.

3.6.6. - E34-F34

Another triple co-transfection with E34, F34 and eGFP was carried out as negative control likewise. Currents no larger than -250 pA (n = 5) under buffer were discarded as ECs and not analyzed further with AA43279 nor TTX. Cells co-transfected with E34 and F34 produced no fluorescence emissions either.

3.7. - Analysis of split, reconstituted channels

The 4 dimeric domains of channels $Na_v1.1/1.4$ were co-transfected in all double combinations for both microscopy and electrophysiology analyses. For patching however, triple co-transfections with eGFP were performed upon the lack of observed sfGFP fluorescence under both spinning disk 100x objectives (sections below) and confocal 40x microscope used in electrophysiology, for any of the combinations containing tagged D1D2 with D3D4.

3.7.1. - E12-E34 (split $Na_v1.1$)

Absence of current or ECs were only recorded for the cells (n = 6) transfected with the reconstituted $Na_v1.1$ channel cleaved by the half. The 2 currents analyzed, of around -250 pA were dismissed as ECs (*fig. 75*). The low E12 mRNA abundance revealed by qPCR (section *3.9.*) is one probable cause for the lack of $Na_v1.1$-like elicited currents. An absence of sfGFP fluorescence was patent alike, with only few cells emitting autofluorescence (*fig. 76*).

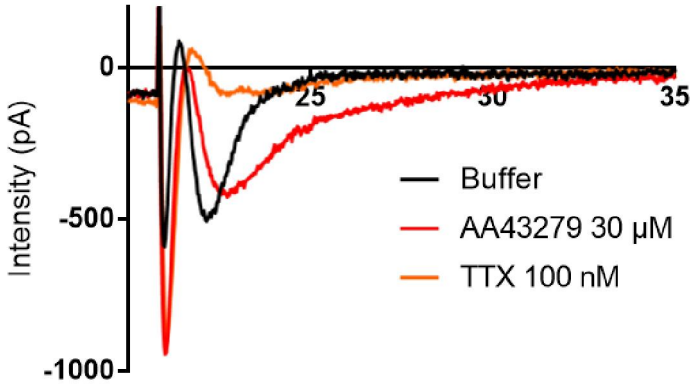

Fig. 75: low-intensity current produced a cell co-transfected with E12 and E34

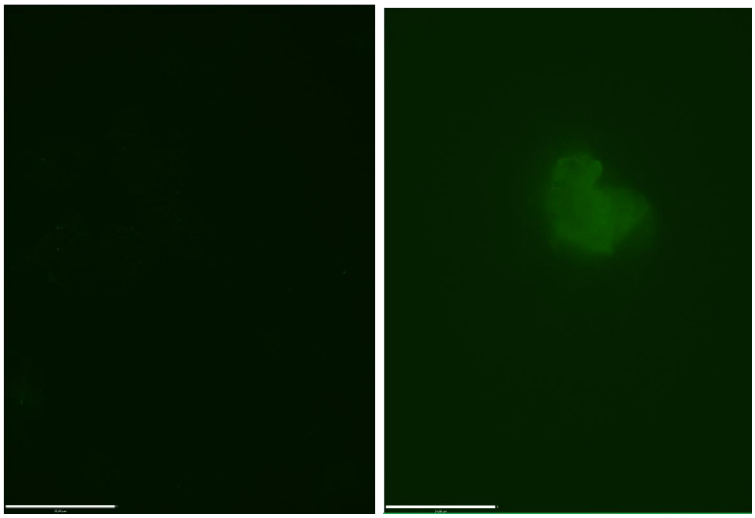

Fig. 76: very dim absorbance (left) and autofluorescence (right) of E12-E34 cells. Magnification is 100x, bar indicates 24 µM

3.7.2. - F12-F34 (split $Na_v1.4$)

Up to 14 cells co-transfected with F12, F34 and eGFP were patched in two different days (7 each), and no $Na_v1.4$-like currents could be recorded. From them, a total absence of current was noted 5 times, while the rest of cells produced ECs not exceeding -100 pA, and a -300 pA unstable during recording. All types of size, morphology and relative eGFP fluorescence were included among the cells patched. sfGFP-induced emissions were neither achieved, with the only autofluorescence present (fig. 77) highly similar of the E12-E34-transfected cells (section above).

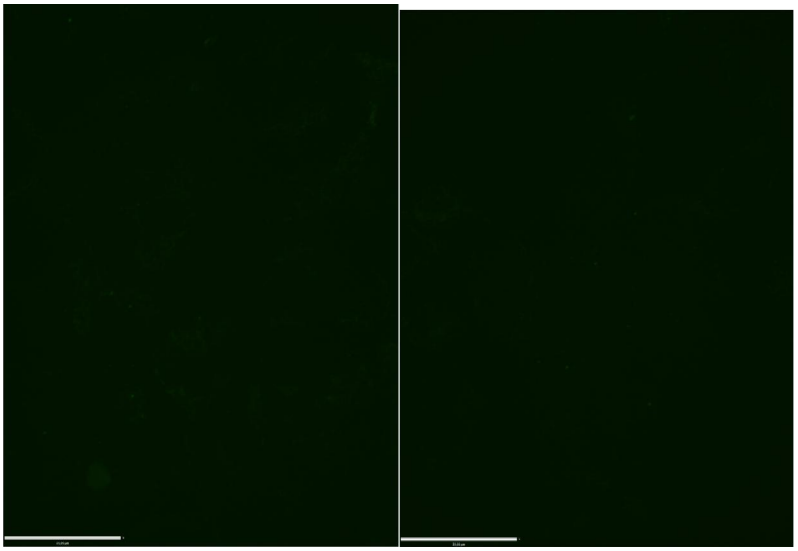

Fig. 77: minor absorbance of F12-F34 cells. Magnification is 100x, bar indicates 24 µM

3.7.3. - E12-F34 (Combination #1)

ECs not surpassing -200 pA were produced in the cells patched (n = 4). A possibility again points towards the lack of E12 expression (section *3.9. qPCR*). Consequently, no sfGFP-induced fluorescence was present from transfected cells (fig. 78).

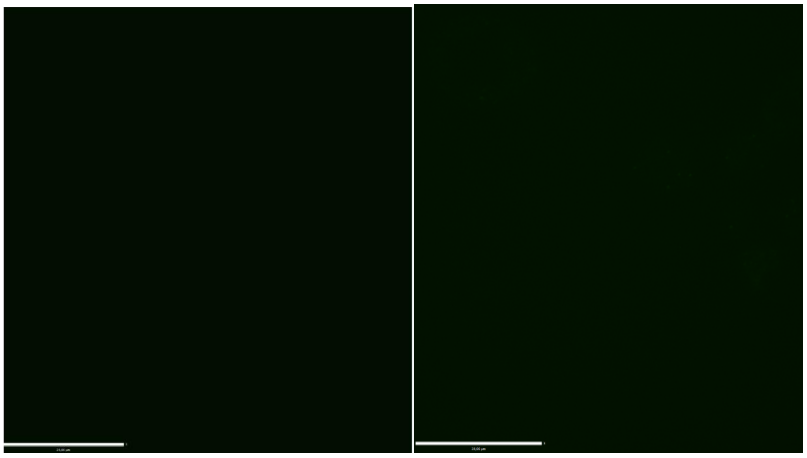

Fig. 78: no fluorescence in E12-F34 cells. Magnification is 100x, bar indicates 24 µM

3.7.4. - F12-E34 (Combination #2)

After the electrophysiological analysis of the characteristics of $Na_v1.1/1.4$-elicited currents in the previous sections, we proceed to examine the properties of the only working dimer combination in this project, which produced < -800 pA currents past the EC threshold. Co-transfection of F12 with E34 produced a low successful yield of current-eliciting cells (3 recorded out of 6, only 2 analyzable on *fig. 79*) that was still higher than other dimer combinations (0), including re-constituted $Na_v1.4$ channels (F12-F34).

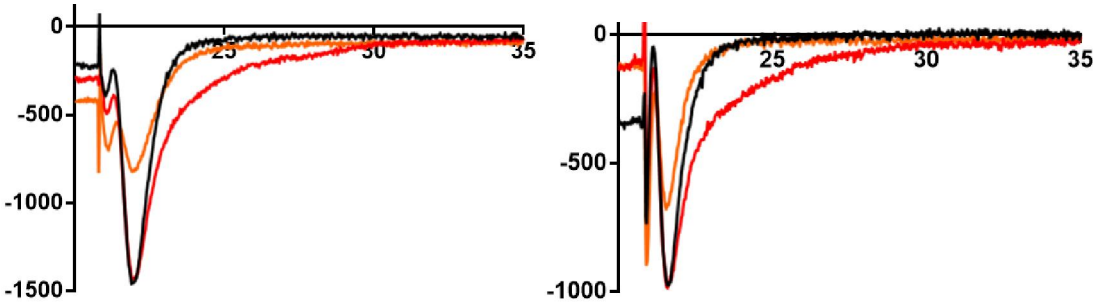

Fig. 79: superimposition of AA43279 and TTX effects over buffer, in the 2 analyzable F12-E34 cells (left and right). Legends have been omitted (black: buffer, red: AA43279 30 µM, orange: TTX 100 nM)

A great number of conditionals to take into account do not allow for an assured identification of these currents as F12-E34-elicited. The only 2 currents available, deviations between them, instability along the recordings (*fig. 81*), absence of sfGFP fluorescence (*fig. 80*) and low intensities with respect to $Na_v1.1$-1.4-elicited currents must be considered. Application of TTX only resulted in a partial inhibition of these 2 currents (*fig. 79*), another characteristic of endogenously-elicited currents. A probability exists in which these currents result from the sum of a big contribution of ECs and F12-E34-elicited, or that could even be the highest ECs recorded to date.

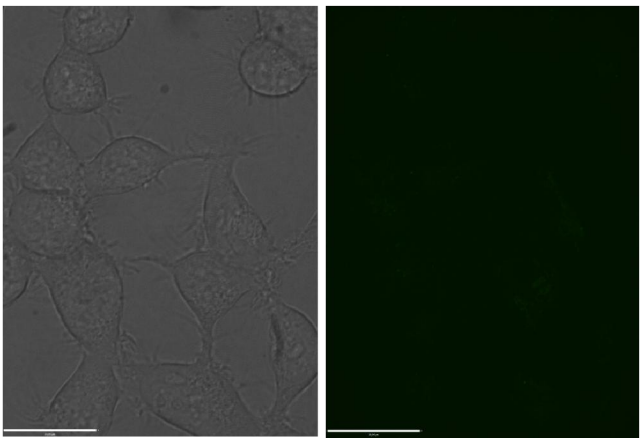

Fig. 80: dim autofluorescence of subcellular organelles (right) in E12-F34 cells (left). Magnification is 100x, bar indicates 24 µM

3.7.4.1. - F12-E34 – Manual patch-clamp

The cells patched elicited Na_v-like currents despite the absence of fluorescent sfGFP complementation. Noticeably, the quality of the recordings resulted impaired and decreased over the course of the experiment runs (due to sustained leak), and especially after depolarizing *IV protocols* (*fig. 81*). Furthermore, the only samples available allowed for a unique 30 µM AA43279 analysis.

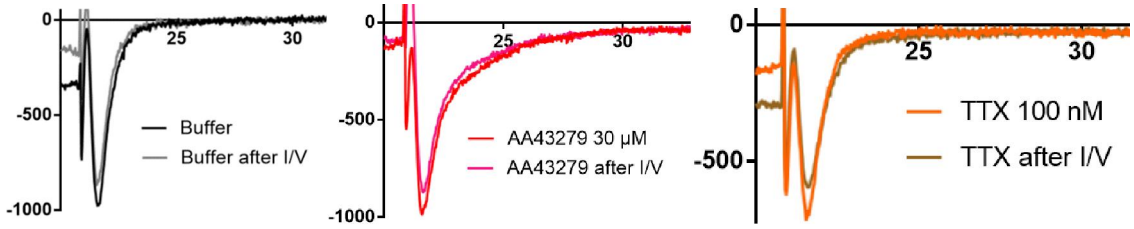

Fig. 80: instabilization effect observed repeatedly in *Step* protocols, immediately after applicating *IV* protocols. MPI is suddenly decreased between -50 and -100 pA, and non-recovering, for cells transfected with dimers

The aim of the following sections is to analytically draw conclusions regarding the identity of these 2 currents recorded, and to be able to discover variations in AA43279's effect when applied in this *supposed* chimeric molecular target.

3.7.4.1.1. - F12-E34 – MPI

The 2 MPIs recorded under control conditions reached -1458 and -976 pA, surpassing the -800 pA threshold that the largest ECs have achieved in HEK293 cells[76]. Compound application slightly increased said currents to -1467 and -985 pA, a 1.01-fold increase for both (*fig. 82*). The third, unanalyzable current due to a quick cell lysis, elicited a -1040 pA MPI under buffer.

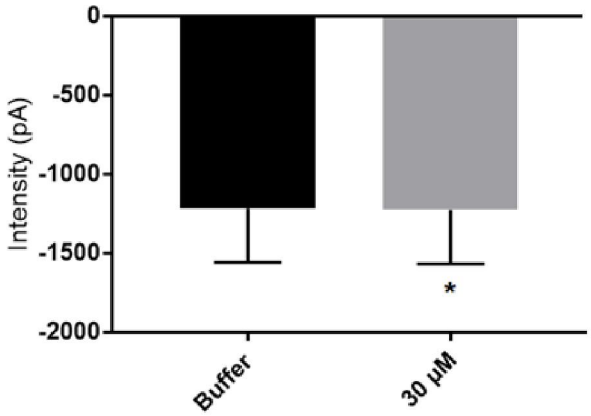

Fig. 82: mean MPI increase after 30 µM AA43279 application (*: $p < 0.05$)

Bearing the overall modest peak increases elicited by AA43279 in the previous channels analyzed, it is still difficult to relate the peak increase to any of the Na_v members. However the smallest MPI increases, not usually higher than 1.1-folds at 30 µM AA43279, are most characteristic of $Na_v1.4$.

3.7.4.1.2. - F12-E34 – AUC

More substantial increases were obtained for AUCs with respective 1.89 and 2.27-folds for the 2 cells, which also indicate a non-concomitant AUC increase regarding to original buffer MPIs (*fig. 83*).

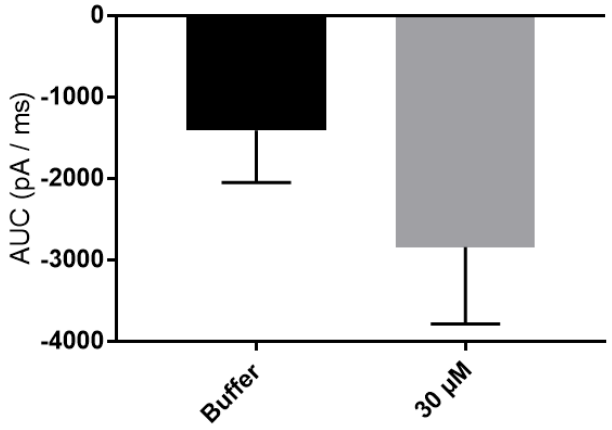

Fig. 83: mean AUC increase after 30 µM AA43279 application

These increases surpass the ones elicited for $Na_v1.4$ (1.29 to 1.8-folds), albeit they broadly miss to reach the AUCs produced in $Na_v1.1$ (3 to 4.5-folds) with 30 µM AA43279, but however fall into the orbit of the ones recorded for ECs (2.16 to 2.76-folds, Discussion section *4.4.*).

3.7.4.1.3. - F12-E34 – tau

Tau values under control conditions marked respectively 0.62 and 0.52 ms, prolongated respectively to 0.91 and 0.83 ms (*fig. 84*) and accounting for a mean 1.54-fold increase.

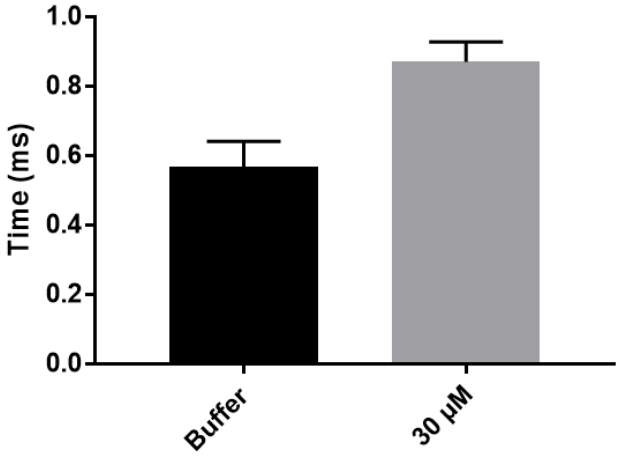

Fig. 84: mean tau increase after 30 µM AA43279 application

Comparing to the overall tau increases in other Na_v members, the 1.83-fold in ECs seems most related than the 3.6-fold in $Na_v1.1$ or the mean 0.96-fold decrease for $Na_v1.4$.

3.7.4.1.4. - F12-E34 – I/V relation

A complete overlap in the baseline and activating phases is observed between control and compound applications, with no major differences. The first fraction of these *channels* becomes conducting at -50 mV, even if a slight decrease from baseline is noticeable at -60 mV (*fig. 85*), a trait never observed for the previous channel members. For the linear ascending phase, the minor leftward shift in conductance is something only observed for $Na_v1.4$ at 10 µM and 3 µM AA43279 concentrations.

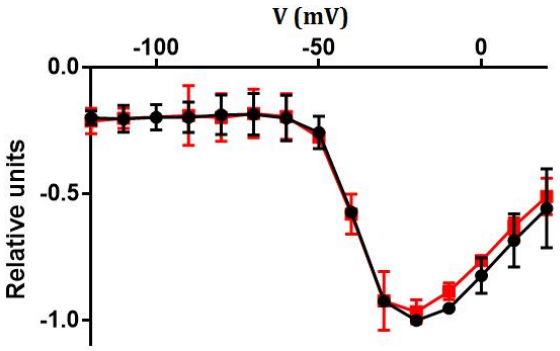

Fig. 85: I/V plot normalized at -20 mV for buffer (1, black). RUs are in intensity units

From these data altogether, a relatability is traced to the $Na_v1.4$ I/V relations with their characteristic "virtual overlaps" in the majority of phases and sweep points that indicate no substantial AA43279 effect.

3.7.4.1.5. - F12-E34 – Activation

Despite a virtually complete overlap likewise, AA43279 produces an almost neglectable tiny leftward shift in the activation slope from -50 mV to -30 mV. In accordance to the I/V relation expressed in the above section, the first tiny conductance increase can be perceived at -60 mV (*fig. 86*). It is also remarkable the absence of current enhancement at high potentials (typical of $Na_v1.4$) that it actually becomes slightly reduced at -10 mV with AA43279 application.

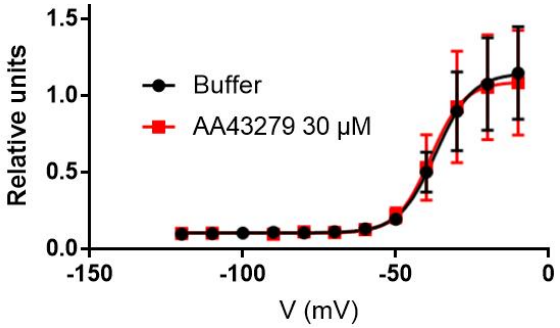

Fig. 86: SSA plot normalized at -20 mV for buffer (1, black) and fitted for the Boltzmann equation. RUs are in conductance units

Consequently, V_{50act} is decreased from -36.9 mV to -38.6 mV with 30 µM AA43279. It represents the smallest difference in V_{50act} recorded so far, in comparison with the Δ-3 mV differences for $Na_v1.4$ and Δ-2.5 mV for ECs.

3.7.4.1.6. - F12-E34 – Inactivation

A clearer effect of AA43279 is noticed for the inactivation relation with a small conductance increase at -120 and -110 mV (*fig. 87*), and a distinctive leftward shift in the inactivation slope typical of $Na_v1.4$ likewise.

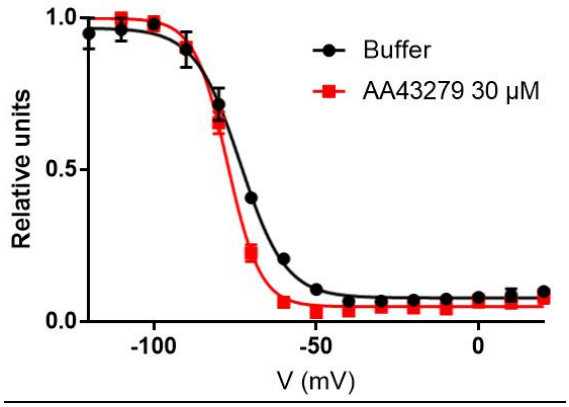

Fig. 86: SSI plot normalized at -20 mV for buffer (1, black) and fitted for the Boltzmann equation. RUs are in intensity units

The $V_{50_{inact}}$ is thus shifted from -73.4 mV with buffer to -77.4 mV under AA43279 application. A Δ-3 mV was also the signature effect of 30 µM AA43279 over $Na_v1.4$.

With all the data provided for the F12-E34 combination, the need for more replicates and robust samples should be necessary, along with a full dose-response evaluation of the AA43279 effect. The low amount of successfully patched cells and the lack of sfGFP complementation may indicate that only ECs were elicited, and that this combination did not actually work. However, the small but unique differences these currents showed are discussed in more detail in section *4.2. F12-E34: final assessment*.

3.7.5. - F3E4

A last dimeric construct with D3 from $Na_v1.4$, and D4 from $Na_v1.1$, was cloned and transfected for a final attempt at narrowing the binding site of AA43279. A functional self-dimerization was again found to be non-existent, for 8 cells patched only one exhibited a -200 pA EC, with the rest producing >-50 pA and total absences of current.

3.7.6. - E3F4

This dimeric construct, having domain III from $Na_v1.1$ and domain IV from $Na_v1.4$, resulted impossible to clone past the stage of ligation, and therefore unable to be produced for electrophysiology analyses.

3.8. - Full length chimeric channels

Data from MPC shows a clear delay of the fast-inactivation slope of $Na_v1.1$ after application of AA43279, subsequently increasing the AUC and tau parameters. In accordance to other toxin compounds exerting this same effect[38], AA43279 was hypothesized to bind on the same extracellular site between S3 and S4 of D4.

As a secondary approach to the modular strategy, full-length channel constructs were synthesized (GenScript) replacing $Na_v1.1$D4 by its homologous in $Na_v1.4$. These experiments aimed to test a possible decrease in AA43279's efficacy towards those chimeric $Na_v1.1$ channels expressing critical transmembrane regions of $Na_v1.4$ instead.

By using one the 3' XhoI restriction site on $Na_v1.1$ cDNA, another XhoI site (CTCGAG) was introduced in the cytoplasmic loop between D3 and D4. After the synthesis of $Na_v1.4$'s D4 with the addition of flanking CTCGAG sequences, the chimeric constructs were ready to be cloned.

Co-transfections with eGFP were performed for an *in situ* localization of the cells to patch. Furthermore, qPCR analysis showed the 3 chimeric constructs (sections below) being expressed at correct mRNA levels.

3.8.1. - E123-(LE)-4 (Chimera #0)

The mere addition of the CTCGAG sequence implied the insertion of residues Leu and Glu in the channel's D3D4 loop. Therefore, this construct was tested as a control in transfected HEK cells (n = 10). ECs between -200 pA and -300 pA (5 cells) and absence of current (2 cells) were observed, indicating this mutation compromises the functionality of $Na_v1.1$ nearly abolishing any current to be elicited.

3.8.2. - E123F4 (Chimera #1)

This chimeric channel featured TM segments S1-S6 from $Na_v1.4$D4 replacing the homonymous in $Na_v1.1$ sequence with no other modifications in the flanking D3D4 or C(t) cytoplasmic loops. Similarly to the previous construct, all the cells patched (n = 8) showed just endogenous Na^+ curves (max. MPI = -220 pA) and no current in 2 of the cells.

3.8.3. - E123 F4VSD E4PFD (Chimera #2)

On this construct, only TM segments S1-S4 from $Na_v1.4$D4 – forming the voltage sensor domain – replaced the ones of $Na_v1.1$, while keeping this last's segments S5 and S6 – the pore-forming domain. This chimeric D4 was not cloned but synthesized *de novo*, and later added downstream the inserted XhoI site.

For n = 9, up to 7 cells produced ≤ - 700 pA ECs (*fig. 87*), with the remaining 2 eliciting -900 pA and -1050 currents. However, the cells with the largest MPIs were remarkable in their

instability, including premature lyses, great leaks, MPI losses after bursts, and peaks fused to transients altogether affecting their correct analysis.

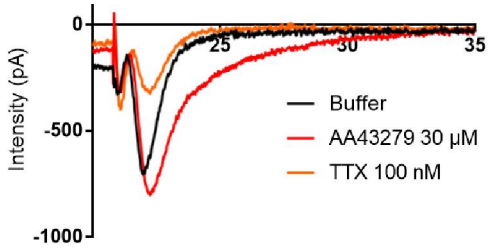

Fig. 87: low-intensity current produced a cell transfected with the ch#2 $Na_v1.1$

3.9. - qPCR

The absence of dimer-elicited and chimera-elicited currents in general led to the suspicion of a possible lack of expression of the constructs at a transcriptional level. A qPCR experiment was carried out with the design of custom primers flanking each insert CDS within their respective constructs. The same set of 4 primers were used for each construct: 2 annealing to $Na_v1.1$ sequence, and the other 2 with $Na_v1.4$ (fwd + rev). The ΔCt values were represented in grouped sets of 4 columns for each construct, their height indicating the amount of DNA replicated (measured by incorporated fluorescence) in regards to the nº of amplification cycles (*fig. 88*). Thus, the first columns of each group trespassing the Ct threshold indicate presence of $Na_v1.1D1D2$, second columns indicate $Na_v1.1D3D4$, third columns indicate $Na_v1.4D1D2$, and fourth columns indicate $Na_v1.1D3D4$.

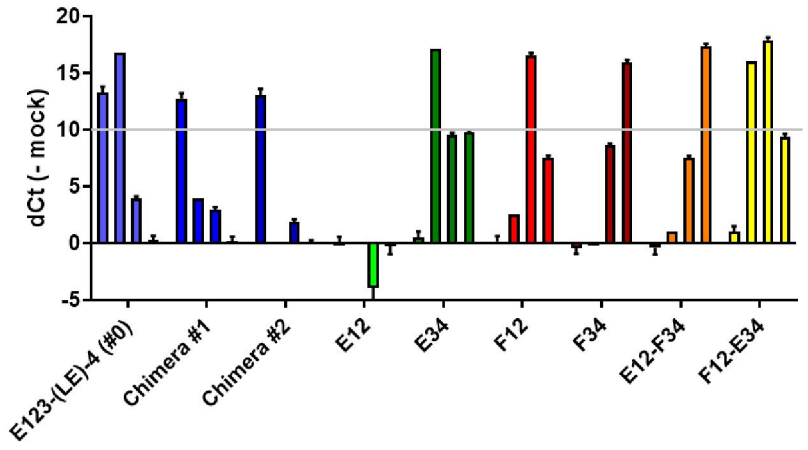

Fig. 88: qPCR plot of the constructs assayed (X axis) and their *in vitro* amplification values represented as fluorescence (Y axis) in regards to nº cycles (ΔCt). Threshold is set at n = 10 cycles

From the plot above, it is noticeable that all of the dimeric – except for E12 – and chimeric constructs are produced intracellularly in enough levels (ΔCt > 10). Moreover, the amplification of each dimer (alone or in combination) corresponds to its reported fluorescence (2nd column for E34, 3rd bar for F12…). This discovery frontally clashes with the previous results that altogether show no elicited currents expectedly proceeding from them. An incorrect protein trafficking, structure misfolding, or displacement of the VSD charges leading to voltage misgatings, could be among the hypotheses explaining the absences of current (section *4.2.2.*).

4. DISCUSSION

4.1. - Prelude to Discussion: summary of results

The workflow of the experiments performed in this project started with the testing of the sfGFP complementation method with small constructs, which resulted negative for C(t)-sfGFP11 and positive for its N(t)-tagging as revealed by fluorescence microscopy. Afterwards, all the ion channels chosen had their individual or pair of subunits amplified, N(t)-tagged with sfGFP11 or C(t)-tagged with GFP1-10 and cloned as confirmed by sequencing.

The constructs were expressed in HEK cells to confirm production and functionality by respectively imaging and electrophysiology. Previously, dose-response MPC experiments of $Na_v1.1/1.4$ response to AA43279 showed success despite small divergences with APC. Upon confirmation with sfGFP-$K_v2.1$, the individual Na_v dimers were assayed as controls having negative fluorescence and conductance. All combinations of D1D2 + D3D4 domains, including split *native* Na_v channels ($spNa_v$) and split *hybrid* channels (combinations), elicited no own currents. An exception was found in 2 (out of 6) F12-E34 cells producing yet unstable, medium-intensity recordings resistant to TTX.

Finally, the chimeric Na_v constructs showed that a simple insertion of 2 residues in the interdomain D3D4 loop is enough to nullify any of their own produced currents. Therefore in general, Na_v channels have proved to be sensitive constructions to modify and work with, in regards to simpler K_v channels.

4.2. - F12-E34: final assessment

Based upon the minor conclusions reached after each parametrical analysis for F12-E34, there are numerous arguments for and against behind the true nature of these currents as the result of a functional interaction or simply as ECs.

Arguments for include the parameters not resembling an EC: MPI, I/V and inactivation relations. The overall resemblances after AA43279 application can be considered identical towards $Na_v1.4$, with the highlighted differences also more characteristic of that channel than of others.

Arguments against include all the parameters most related to an EC (sections *4.4.* and *4.4.2.*): AUC, tau and activation rate – this last one also closely related to $Na_v1.4$ –, without overlooking the low transfection success (2 of 6).

Nevertheless, the fact that the 2 analyzed currents surpass the maximum -800 pA threshold for ECs, distances the possibility of such being totally endogenously-elicited - notwithstanding a probable partial contribution. Besides, the attenuated $Na_v1.1$-related effects (AUC and tau), despite the verified E34 expression, raises a hypothesis on whether the non-affine F12 dimer may be driving the AA43279-sensitive E34 dimer towards a lesser affinity for the

compound, ultimately reaching "midpoints" in effectivity that come into proximity to those observed in ECs and are falsely related to it.

The possibility of an incomplete interaction between F12 and E34 rendering it functionally responseless to stimuli, is neither discarded. A reduced/impaired ion conductance for F12-E34 could explain why currents larger than -800 pA were achieved. However, other research addressing functionality of split Na_v channels between domains II and III (section *4.3.*) reinforces the possibility of functional interdomain interactions.

The arguments above exposed might indicate that a F12-E34 functional interaction is taking place, with hybrid effects in the AA43279 mode of action as a result, and that the currents observed might be a sum of this F12-E34 interaction and a partial EC contribution. However, the only cells recorded (2/6), their medium-low intensities elicited (> -1400 pA) and the absence of any currents from up to 14 F12-F34 samples (the split, reconstituted $Na_v1.4$) despite expression, might plainly indicate these are just either magnified ECs (by drastic conductance rises) or the biggest ones recorded to date in HEK293 cells. Further experiment replicates with this combination of dimers, additionally using $Na_v1.7$-specific toxins (section *4.4.* and subsections), could probably evidence the nature behind these currents.

4.2.1. - F12-E34: further study

The need of more stable, robust analyses is imperative for a definitive assessment of the identity and true electrophysiological properties of the interaction between these two dimers. Such data would also strengthen the hypothesis of the mode of action of AA43279 in the $Na_v1.1$D3D4 half that is nevertheless impaired by the presence of the $Na_v1.4$D1D2 dimer.

Analyses performed by APC would allow a greater amount of cells to be tested, their recordings to be better fitted and normalized, and the false EC positives to be excluded subsequently reducing standard deviations. Besides, the possibility of performing dose-response curves for the AUC and tau values, and to compare them with those of the other Na_v members, would help to state the nature of this F12-E34 combination thus allowing for other combinations of Na_v constituent domains to be tested in the future.

4.2.2. - F12-E34 and F12-F34: discussion of failure

The two dimer combinations in this project giving place to a split, but reconstituted whole channel ($spNa_v1.1$ and $spNa_v1.4$), did not even become functional and work as intended. Despite the lack of sfGFP complementation, a qPCR analysis revealed enough expression for 3 of the channel halves (excluding E12) by using specific 5' and 3' flanking primers for each. Therefore, an explanation must reside at a genetic or post-translational level.

Cloning of the $Na_v1.1/1.4$ dimers implied minor modifications to the *SCN1A* and *SCN4A* genes, aside from the 3' and 5' tagging with sfGFP. The split location for both was chosen in the intracellular loop between domains II and III, immediately downstream the AIS binding domain in

each gene. This implied the AIS sequence, despite conserved without splitting, would be relegated to the I+II dimers with the III+IV halves receiving no sequence. Furthermore, the new location for the AIS, just immediately upstream the new split 3' end, could have had some implications for the intended function of this sequence in channel trafficking to the neuron AIS[74].

At a protein level, a structure cut in a half implies the exposure of internal segments of the Na_v channels to the cytoplasm and lipid bilayer. The potential new hydrophilic or hydrophobic interactions could result in structural changes that would ultimately render the 2 split dimers unable to complement sterically. Subsequently, the ubiquitination of non-functional proteins could be the cause leading to their degradation through intracellular proteases or proteasomes.

However, none of these hypotheses were observed in the first reported experiments at studying the functionality of split Na_v channels (section below), where the same rationale for the split location (in between D2D3) worked indeed as good as with native channels. The exact explanation for the failure in this project is therefore unknown, however future attempts with the addition of signal or trafficking sequences to the channels' cDNA could produce enough desired functionalization.

4.3. - Previous attempts at modular approach with sodium channels

The first attempt at studying how the Na_v domains are responsible for channel activity, while following a modular approach, was performed in 1989[45]. The authors expressed pairs of cleaved $Na_v1.2$ domains in different combinations, and reported elicited Na^+ currents should the 4 constituent domains be present in the cell. From them, co-expression of domains I and II with domains III and IV, yielded almost native Na^+ currents in shape in *Xenopus* oocytes. Cleavages between domains III and IV produced impaired non-inactivating currents, while cuts between domains I and II resulted in marginal currents. The modifications allowed even for deletions to be produced at the N(t), C(t), or between D2 and D3 and still produce significant currents. Finally, the authors discarded the generation of any Na^+ currents by the expression of single, pairs or trios of domains alone.

The number of coincidental strategies performed in this project (split halves of channels, co-expression, controls for halves alone) throws in the question of why many channel combinations did not result functional - let alone the lack of E12 expression - and why did so few attempts achieved success. The reasons may be situated in the different methodology employed. The size of the *Xenopus* oocytes allows to obtain large currents and likewise magnify smaller ones that would go unperceived in other cell systems. Furthermore, the mRNA injections applied guarantee a total control and assurance that the desired mRNA – which also experiments an immediate translation – will be expressed. However, these results cannot be directly related to a biomedical application because of the heterologous expression system and mRNA injection methods used.

Another similar project developed by a group at University College of London[75] aimed at splitting $Na_v1.1$ by the D2-D3 loop and delivering said cDNAs in N2a cells (neuroblastoma) using two different sets of AAVs. A higher expression was intended by the addition of synapsin

promoters to both inserts, and the detection of their live functionalization was achieved by a GFP+RFP terminal labeling of each half.

This method allowed for a co-localization – let alone their physical close interaction – of both inserts by the additive green and red fluorescence observed, without the problems derived from a sfGFP complementation *in situ*. Besides, the use of AAVs is documented to produce high transduction rates in many cell models. But despite the detected co-expression of $Na_v1.1$ halves, the maximum currents elicited of only -150 pA along with a leak of the same magnitude, raise the question of whether that current belongs to the $Na_v1.1$ domains together. Different types of neurons can express Na_v isoforms 1.1/1.2/1.3/1.6/1.7 in varying proportions, and the possibility for ECs to be elicited by residual expression of any of those channels could still be high in a N2a tumoral neuroblast line.

4.4. - Endogenous channels in control cells - Article

According to a paper[76], HEK293 cells can produce $Na_v1.7$ channels with a constitutive expression. Other Na_v isoforms were also detected endogenously like $Na_v1.3$, 1.5 and 1.2 – but not 1.1 nor 1.4 –, although with a much lower abundance and not permanently over passages. $Na_v1.7$ was found to be the isoform expressed over a longer number of passages.

The study discovered HEK cells eliciting -100 - -400 pA currents on average, with MPIs reaching up to -800 pA. Up to 3 different fractions of cationic currents were classified based upon sensitivity to TTX, cadmium, or neither (*fig. 89*).

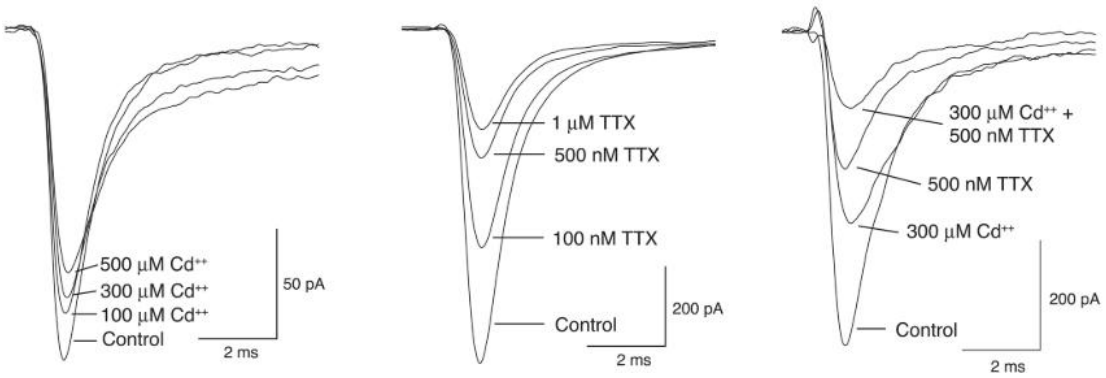

Fig. 89: effect on $Na_v1.7$-elicited MPIs after Cd^{2+} and TTX application (from He, B., & Soderlund, D. M. (2011) [76])

Application of tefluthrin provoked a great delay in the inactivation phase of the curves, an effect associated to Na_v-elicited currents. Furthermore, toxins reduced MPIs to a mean 53% of control upon 500 nM TTX application, to 65% with 300 µM Cd^{2+}, and to 28% with joint administration of both (*fig. 89*). The repeatedly persistent currents reported were identified to be elicited by polycystin-2 (*PKD2*), a Cd^{2+}-sensitive, TTX-resistant cation channel constitutively present in the plasma membrane of renal cells[77].

Therefore, the possibility is raised that many of the recorded low-intensity currents in this project, falling below -800 pA MPIs, might actually be elicited by constitutive $Na_v1.7$ channels and not by the transfection with modified channels nor their domains alone as initially thought.

4.4.1. - $Na_v1.7$ – Published literature

Data from APC[9] shows $Na_v1.7$ being the second-least affine Na_v member for AA43279 and, like $Na_v1.4$, responds to it with a 0.96, 0.86 and 0.93-fold inhibition to MPI, AUC and tau values respectively. Moreover, a plateau is again observed between 30-100 µM indicating no further inhibitory activity.

$Na_v1.7$ is mainly expressed in ganglional neurons in the PNS (and to a lesser extent in the CNS) and has been characterized as the main player in the generation of neuropathic pain[78]. Consequently, a great focus on developing drugs against $Na_v1.7$ has been put for the treatment of algesic diseases, with selective and potent compounds (heteroarylsulfonamides as PF-06456384, PF-05089771[79, 80, 81]; peptide toxins as ProTx II and ProTx III, *fig. 90*) already developed as analgesics. For this study, it would have been useful to employ one of the previous drugs for a possible identification of $Na_v1.7$ as the causing agent of the ECs present.

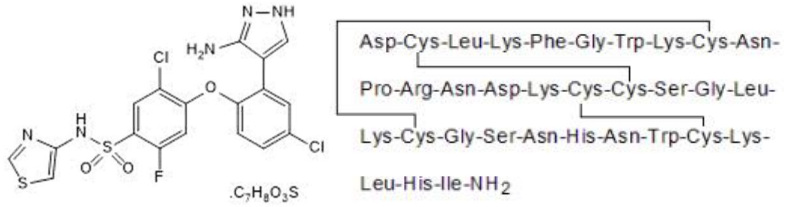

Fig.90: chemical structure of PF-05089771 (left). Biological structure of ProTx III (right)

4.4.2. - Endogenous currents – Parameters

A parallel analysis was performed in some of the cells with MPIs below -800 pA. Despite here treated as "endogenous currents", these cells proceeded from both the $Na_v1.1$-stable and $Na_v1.4$-transfected lines that failed to elicit a sufficient MPI, and also behaved differently than them. However, a residual contribution of these channels could be present and thus these ECs cannot be completely attributed as endogenously-elicited.

AA43279 concentrations of 30 and 3 µM were tested. At 30 µM, MPI, AUC and tau increased in 1.08-1.5 folds, 2.15-2.76 folds, and 1.83-fold. At 3 µM, MPI, AUC and tau increased in 1.1-fold, 1.09-1.24 folds, and 1.46-fold. Both concentrations promoted a leftward shift on the I/V activation slopes, and a net increase in maximum conductance at -20 mV. The $V50_{act}$ were shifted a mean Δ-3.5, and the $V50_{inact}$ shifted a mean Δ-1.2 mV. Baselines and first voltages of activation/inactivation were similar to those in $Na_v1.1/1.4$. Finally, application of 100 nM TTX resulted in a partial disappearance of these currents, with some showing continued conductance and resistance to a complete blockage.

4.5. - AA43279: assessment of effect

The binding site of AA43279 in could unfortunately not be traced by this modular strategy. Nevertheless, the general aspects of the AA43279 effects reported could be related to its prospective therapeutical administration. The modest MPI increases, proportional to the compound concentration, can make GABAergic FSINs produce more satisfactory inhibition outputs onto the Pyr's they innervate. The key rises in AUC and tau can be directly translated into

the prolongation of inhibitory stimuli over a longer period of time. Finally, the leftward shift in the I/V and activation relations to more negative potentials, can mean the FSINs will require a lower AP threshold to be activated from their feed-back and feed-forward circuitries. These effects altogether situate AA43279 as a potential candidate to effectively modulate the activity of $Na_v1.1$. But importantly however, the also worrisome activation of cardiac $Na_v1.5$ channels in considerable magnitudes (*fig. 28*) will be an issue to extensively assay in *in vivo* and preclinical studies before its possible commercialization.

The hypothesis of a binding site in the S3S4 loop of $Na_v1.1$D4, based on the same effect achieved by other compounds, must still be tested. These compounds included a wide variety of animal toxins from spiders, scorpions and sea anemones (see introductory section *1.9.2.bis* Activators and inhibitors). The spider δ-atracotoxin halves the MPI and I/V relation while rises AUC, mainly because of inducing a persistent inward Na^+ current and not because a delay in the $t_{1/2}$ of inactivation[46, 47, 48]. The scorpion α-toxin, despite not affecting MPI, achieves a great AUC increase too by persistent currents and an extraordinary delay in the inactivation conformational change[49[. Lastly, sea anemone toxins produce an AUC and tau rise without persistent current and reduced variations in MPI, the most related effects altogether compared to AA43279[50].

4.6. - sfGFP-$K_v2.1$ and its relation between fluorescence and conductance

Up to 4 sfGFP-tagged *hetero*tetramers can form up a functional $K_v2.1$ channel, which will be visible as long as one sfGFP1-10-tagged and one sfGFP11-tagged are present in the structure at least. The least "bright" channel can be produced as a result of a 3:1 or 1:3 $K_v2.1$-sfGFP1-10:sfGFP11-$K_v2.1$ oligomerization. By taking this channel as a reference, a "double-bright" channel can be possible with a 2:2 relation that yields 2 complete sfGFP molecules within the same channel.

Imaging-wise, discerning between the 3 different combinations abovementioned is currently impossible with available methodology, notwithstanding the altogether size, expression rate and health between the cells observed. Electrophysiology-wise, it is likewise impossible to certainly correlate the brightness observed with the total K^+ current elicited by the cell. Firstly, because functional tetramerization is not dependable on relative sfGFP complementation, and a 3:1 or 1:3 channel can be as conducting as a 2:2 one. Secondly, because dim cells that receive either low $K_v2.1$-sfGFP1-10 or sfGFP11-$K_v2.1$ plasmids can still be very conducting, should they majorly produce channels in 4:0 or 0:4 configurations. Thirdly and last, because $K_v2.1$ density in the cell membrane is inversely proportional to total conductance[69, 72]: an overpopulation of $K_v2.1$ channels reduces the total K^+ current the cell can elicit.

Finally, a "4-fold bright" channel is the result of 4x sfGFP11-$K_v2.1$ monomers bound to 4x soluble sfGFP1-10s, and the brightest channel achievable by sfGFP-tagging $K_v2.1$. Its electrophysiological properties are undistinguishable from the above combinations (Results section *3.5. $K_v2.1$*). A fluorescence comparison is however not possible here because of the different type of microscopes and objectives used (*fig. 63*).

4.7. - Alternative strategies in the treatment of schizophrenia

A number of other pharmacological approaches have been proposed for the treatment of schizophrenia[82]. Apart from the classical dopamine approaches targeting D1 and D2 receptors (section *1.5.1. Schizophrenia*), the administration of atypical neuroleptics increasing the levels of dopamine and serotonine (clozapine[83], risperidone) seem to alleviate the negative symptoms in some patients. Noradrenaline is implicated in both the cognition issues and the positive symptoms in SZ, therefore a double approach in activating presynaptic and postsynaptic α_2 receptors, respectively reducing and enhancing NE activity, has been hypothesized[82]. Acetylcholine also holds an important role in cognition, hence why some AChE inhibitors (rivastigmine[84], donezepil[85]) have been proven to increase neuronal cholinergic activity and alleviate psychotic symptoms of SZ. Finally, the allosteric modulation of M1 and M4 mAChRs, found in decreased levels in SZ patients[86], may activate the signaling pathways for the release of dopamine and acetylcholine without the adverse effects of the conventional drugs targeted at these neurotransmitters.

4.7.1. - Other ion channels implicated in epilepsies

Apart from sodium channels $Na_v1.1$ and $Na_v1.2$, mutations in several other ion channel genes can result in various types of epilepsy. An early diagnostic of the genes affected by next-generation sequencing techniques can detect nearly all pathologic SNP variations[87], and is fundamental for correctly addressing the therapeutic strategy to administer.

Mutations in *KCNQ2* are associated to benign familial neonatal epilepsy, an encephalopathy with better remission rates for seizures and cognition. The role of this $K_v7.2$ channel is the repolarization of the membrane potential to control further APs from being evoked, so its loss-of-function is postulated to generate a network overexcitation that would ultimately cause these seizures[87]. Contrarily, gain-of-function mutations in the *KCNT1*-encoded, Na^+-activated K^+ channel is related to the appearance of epilepsy in infancy with migrating focal seizures. It is a rare type of epilepsy with an onset between the first 3-6 months and characterized by turns in head and arms.

The calcium channel $Ca_v3.2$ can bear more than 30 mutations on its *CACNA1H* gene and they are all associated with childhood absence epilepsy (CAE) and other genetic generalized epilepsies. Other LGICs implicated in epilepsies include nAChRs (autosomal dominant nocturnal frontal lobe epilepsy), GABAA receptors (CAE, generalized epilepsy with febrile seizures), and NMDARs (Landau-Kleffner syndrome, nonsyndromic epilepsy)[87].

5. CONCLUSION

Pinpointing the binding site of AA43279 within $Na_v1.1$ was not possible with a modular approach. Despite a reported expression of the majority of modified channel structures at a transcriptional level, their absence of co-localization and functionalization points to the channels destabilizing or degrading. Moreover, the 2 only F12-E34 cells eliciting stable currents do not allow for certain conclusions to be drawn nor to certainly dismiss them as ECs. However, the functionality reported with versatile sfGFP-tagged K_v monomers could potentially be used in upcoming projects, to assess the hybridization of different K_v tetramers and their subsequent electrophysiological variations.

The main objectives not met in this project could otherwise be achieved in future research, by rethinking the methods followed to fix any flaws. Tracing the production of the Na_v halves along their expression pathway could be firstly attained with a more specific antibody labelling. Correctly trafficking the dimers to the cell membranes could be achieved by adding the signal peptides necessary to overcome the putative cellular location where they are retained. Possible destabilizations in the halves' structures could be limitedly-detected by radiolabeled pulse-chase, or with other energy techniques when mixing them in media with varying hydrophobicity. Using brighter and sharper upcoming sfFPs (as mNeonGreen2[88, 89]), along with tandem repetitions of the 11th strand[68] + soluble sfGFP1-10 would allow for a better detection of the split, reconstituted channel halves. Finally, another cell model without endogenous channels or currents would spare the difficulties derived from discerning between false-positive currents and the true ones sought.

Other strategies such as the use of an AAV system could increase the number of transduced cells in regards to lipofections, and stronger promoters could raise the inserts' expression if needed. The use of a double reporter system of fluorescent proteins, despite good for detection without relying in complementation, does not guarantee an interaction is taking place. In this sense, FRET techniques could potentially solve this issue by labeling the separate channel components with dimer-specific antibodies on their extracellular domains – should the big size of the antibodies not interfere with their conductance[90].

All in all, the possibilities that sfFPs provide to study protein-protein interactions whilst safeguarding their *in vitro* function should not be overlooked. This becomes even more important with pathological molecular targets that are sensitive to modifications impairing their function, and that otherwise cannot be studied with current methods. It is possible this technique will be refined and applied in a future between alpha subunits of more complex VGICs or LGICs, and even with their regulatory β-subunits, to overall provide us with deeper knowledge about the activity of ion channels.

6. ACKNOWLEDGEMENTS

The author of this work wishes to extend his utter thanks to Drs. Benned-Jensen, T. and Duroux, M., as well as to Sr. Tech. Hougaard, C., for their incontestable support along the realization of this project. Another great number of scientists, technicians and students provided with unquestionable help and are mentioned in the Preface of this Thesis.

7. CONFLICT OF INTERESTS

This work was financially supported with a scholarship from the Lundbeck Foundation (Lundbeckfonden). All the materials and devices were provided by Lundbeck, as well as all experiments were carried within Lundbeck's facilities (Lundbeck A/S, Valby, Denmark).

8. REFERENCES

1. Schultz, S. H., North, S. W., & Shields, C. G. (2007). Schizophrenia: a review. *Am Fam Physician*, *75*(12), 1821–1829. doi.org/10.1590/S0103-65642006000400014

2. Picchioni, M. M., & Murray, R. M. (2007). Schizophrenia. *British Medical Journal*, *335*(7610), 91–95. doi.org/10.1136/bmj.39227.616447.BE

3. Rossignol, E. (2011). Genetics and function of neocortical GABAergic interneurons in neurodevelopmental disorders. *Neural Plasticity*, *2011*, 30–40. doi.org/10.1155/2011/649325

4. Freund, T., & Kali, S. (2008). Interneurons. *Scholarpedia*, *3*(9), 4720. doi.org/10.4249/scholarpedia.4720

5. Chung, D. W., Fish, K. N., & Lewis, D. A. (2016). Pathological basis for deficient excitatory drive to cortical parvalbumin interneurons in schizophrenia. *American Journal of Psychiatry*, *173*(11), 1131–1139. doi.org/10.1176/appi.ajp.2016.16010025

6. Konradi, C., Yang, C. K., Zimmerman, E. I., Lohmann, K. M., Gresch, P., Pantazopoulos, H., … Heckers, S. (2011). Hippocampal interneurons are abnormal in schizophrenia. *Schizophrenia Research*, *131*(1–3), 165–173. doi.org/10.1016/j.schres.2011.06.007

7. Hu, H., & Jonas, P. (2014). A supercritical density of Na+channels ensures fast signaling in GABAergic interneuron axons. *Nature Neuroscience*, *17*(5), 686–693. doi.org/10.1038/nn.3678

8. Jensen, H. S., Grunnet, M., & Bastlund, J. F. (2014). Therapeutic potential of NaV1.1 activators. *Trends in Pharmacological Sciences*, *35*(3), 113–118. doi.org/10.1016/j.tips.2013.12.007

9. Frederiksen, K., Lu, D., Yang, J., Jensen, H. S., Bastlund, J. F., Larsen, P. H., … Grunnet, M. (2017). A small molecule activator of Nav1.1 channels increases fast-spiking interneuron excitability and GABAergic transmission in vitro and has anti-convulsive effects in vivo. *European Journal of Neuroscience*, *46*(3), 1887–1896. doi.org/10.1111/ejn.13626

10. Markram, H., Toledo-Rodriguez, M., Wang, Y., Gupta, A., Silberberg, G., & Wu, C. (2004). Interneurons of the neocortical inhibitory system. *Nature Reviews Neuroscience*, *5*(10), 793–807. doi.org/10.1038/nrn1519

11. Hattori, R., Kuchibhotla, K. V., Froemke, R. C., & Komiyama, T. (2017). Functions and dysfunctions of neocortical inhibitory neuron subtypes. Nature Neuroscience, 20(9), 1199–1208. doi.org/10.1038/nn.4619

12. Rudy, B., Fishell, G., Lee, S. H., & Hjerling-Leffler, J. (2011). Three groups of interneurons account for nearly 100% of neocortical GABAergic neurons. Developmental Neurobiology, 71(1), 45–61. doi.org/10.1002/dneu.20853

13. Kepecs, A., & Fishell, G. (2014). Interneuron cell types are fit to function. Nature, 505(7483), 318–326. doi.org/10.1038/nature12983

14. Parihar, R., & Ganesh, S. (2013). The SCN1A gene variants and epileptic encephalopathies. Journal of Human Genetics, 58(9), 573–580. doi.org/10.1038/jhg.2013.77

15. Escayg, A., & Goldin, A. L. (2010). Sodium channel SCN1A and epilepsy: Mutations and mechanisms. Epilepsia, 51(9), 1650–1658. doi.org/10.1111/j.1528-1167.2010.02640.x

16. Catterall, W. A., Kalume, F., & Oakley, J. C. (2010). NaV1.1 channels and epilepsy. Journal of Physiology, 588(11), 1849–1859. doi.org/10.1113/jphysiol.2010.187484

17. Creese I, Burt DR, Snyder SH (April 1976). "Dopamine receptor binding predicts clinical and pharmacological potencies of antischizophrenic drugs". Science. 192 (4238): 481–3. Bibcode:1976Sci...192..481C. doi:10.1126/science.3854. PMID 3854.

18. Seeman, P.; Lee, T.; Chau-wong, M.; Wong, K. (1976). "Antipsychotic drug doses and neuroleptic/dopamine receptors". Nature. 261 (5562): 717–719. Bibcode:1976Natur.261..717S. doi:10.1038/261717a0. PMID 945467

19. Tuominen, H. J., Tiihonen, J., & Wahlbeck, K. (2005). Glutamatergic drugs for schizophrenia : a systematic review and meta-analysis, 72, 225–234. doi.org/10.1016/j.schres.2004.05.005

20. Konradi, C., & Heckers, S. (2003). Molecular aspects of glutamate dysregulation : implications for schizophrenia and its treatment, *97*, 153–179. doi.org/10.1016/S

21. Weickert, C. S., Fung, S. J., Catts, V. S., Schofield, P. R., Allen, K. M., Moore, L. T., … Catts, S. V. (2012). Molecular evidence of N -methyl- D -aspartate receptor hypofunction in schizophrenia, *18*(11), 1185–1192. doi.org/10.1038/mp.2012.137

22. Desbonnet, L. (2016). Mouse Models of Schizophrenia : Risk Genes. BS:HBBN (Vol. 23). Elsevier. doi.org/10.1016/B978-0-12-800981-9.00016-X

23. Gonzalez-Burgos, G., Hashimoto, T., & Lewis, D. A. (2010). Alterations of cortical GABA neurons and network oscillations in schizophrenia. Current Psychiatry Reports, 12(4), 335–344. doi.org/10.1007/s11920-010-0124-8

24. Konradi, C., Yang, C. K., Zimmerman, E. I., Lohmann, K. M., Gresch, P., Pantazopoulos, H., … Heckers, S. (2011). Hippocampal interneurons are abnormal in schizophrenia. Schizophrenia Research, 131(1–3), 165–173. doi.org/10.1016/j.schres.2011.06.007

25. Chung, D. W., Fish, K. N., & Lewis, D. A. (2016). Pathological basis for deficient excitatory drive to cortical parvalbumin interneurons in schizophrenia. American Journal of Psychiatry, 173(11), 1131–1139. doi.org/10.1176/appi.ajp.2016.16010025

26. McNally, J. M., & McCarley, R. W. (2016). Gamma band oscillations: A key to understanding schizophrenia symptoms and neural circuit abnormalities. Current Opinion in Psychiatry, 29(3), 202–210. doi.org/10.1097/YCO.0000000000000244

27. Szabo, G. G., Monyer, H., & Erde, F. (2010). Parvalbumin-Containing Fast-Spiking Basket Cells Generate the Field Potential Oscillations Induced by Cholinergic Receptor Activation in the Hippocampus, 30(45), 15134–15145. doi.org/10.1523/JNEUROSCI.4104-10.2010

28. Gataullina, S., & Dulac, O. (2016). From genotype to phenotype in Dravet disease. Seizure: European Journal of Epilepsy. doi.org/10.1016/j.seizure.2016.10.014

29. Jonghe, P. D. E. (2011). Molecular genetics of Dravet syndrome, 7–10. doi.org/10.1111/j.1469-8749.2011.03965.x

30. Lossin, C. (2009). A catalog of SCN1A variants. Brain and Development, 31(2), 114–130. doi.org/10.1016/j.braindev.2008.07.011

31. Shmuely, S., Sisodiya, S. M., Gunning, W. B., Sander, J. W., & Thijs, R. D. (2016). Epilepsy & Behavior Mortality in Dravet syndrome : A review. Epilepsy & Behavior, 64, 69–74. doi.org/10.1016/j.yebeh.2016.09.007

32. Richards, K. L., Milligan, C. J., Richardson, R. J., Jancovski, N., Grunnet, M., Jacobson, L. H., … Petrou, S. (2018). Selective Na V 1.1 activation rescues Dravet syndrome mice from seizures and premature death. Proceedings of the National Academy of Sciences, 201804764. doi.org/10.1073/pnas.1804764115

33. Dale Purves, George Augustine, David Fitzpatrick, William Hall, Anthony-Samuel Lamantia, Leonard White. Neuroscience. 5th Edition (2012). Sinauer Associates, Inc.: Sunderland, MA. ISBN 978-0878936953

34. Lodish H, Berk A, Zipursky SL, et al. Molecular Cell Biology. 4th edition. New York: W. H. Freeman; 2000. Section 15.4, Intracellular Ion Environment and Membrane Electric Potential. ISBN: 9780716737063

35. Black, J. A., & Waxman, S. G. (2013). Noncanonical roles of voltage-gated sodium channels. Neuron, 80(2), 280–291. doi.org/10.1016/j.neuron.2013.09.012

36. Hiyama, T. Y., Watanabe, E., Ono, K., Inenaga, K., Tamkun, M. M., Yoshida, S., & Noda, M. (2002). Nax channel involved in CNS sodium-level sensing. Nature Neuroscience, 5(6), 511–512. doi.org/10.1038/nn856

37. Xu, W., Hong, S. J., Zhong, A., Xie, P., Jia, S., Xie, Z., … Mustoe, T. A. (2015). Sodium channel Nax is a regulator in epithelial sodium homeostasis. Science Translational Medicine, 7(312). doi.org/10.1126/scitranslmed.aad0286

38. Catterall, W. a, Goldin, A. L., & Waxman, S. G. (2005). International Union of Pharmacology. XLVII. Nomenclature and structure-function relationships of voltage-gated sodium channels. Pharmacological Reviews, 57(4), 397–409. doi.org/10.1124/pr.57.4.4

39. Catterall, W. A., Cestèle, S., Yarov-Yarovoy, V., Yu, F. H., Konoki, K., & Scheuer, T. (2007). Voltage-gated ion channels and gating modifier toxins. Toxicon, 49(2), 124–141. doi.org/10.1016/j.toxicon.2006.09.022

40. Brackenbury, W. J., & Isom, L. L. (2011). Na+ channel β-subunits: Overachievers of the ion channel family. Frontiers in Pharmacology, SEP(September), 1–11. doi.org/10.3389/fphar.2011.00053

41. Isom, L.L., De Jongh, K.S., Patton, D.E., Reber, B.F.X., Offord, J., Charbonneau, H., Walsh, K., Goldin, A.L., Catterall, W.A. (1992). Primary structure and functional expression of the b1 subunit of the rat brain sodium channel. Science 256, 839–842

42. Morgan, K., Stevens, E.B., Shah, B., Cox, P.J., Dixon, A.K., Lee, K., Pinnock, R.D., Hughes, J., Richardson, P.J., Mizuguchi, K., Jackson, A.P. (2000). b3: an additional auxiliary subunit of the voltage-sensitive sodium channel that modulates channel gating with distinct kinetics. Proc. Natl. Acad. Sci. USA 97, 2308–2313. DOI: 10.1073/pnas.030362197

43. Yu, F.H., Westenbroek, R.E., Silos-Santiago, I., Scheuer, T., Catterall, W.A., Curtis, R. (2003). Sodium channel b4: a disulfide-linked auxiliary subunit structurally and functionally similar to b2. J. Neurosci. 23, 7577–7585. doi.org/10.1523/JNEUROSCI.23-20-07577.2003

44. West, J.W., Patton, D.E., Scheuer, T., Wang, Y., Goldin, A.L., and Catterall, W.A. (1992). A cluster of hydrophobic amino acid residues required for fast Na(+)-channel inactivation. Proc. Natl. Acad. Sci. USA 89, 10910–10914

45. Stühmer, W., Conti, F., Suzuki, H., Wang, X.D., Noda, M., Yahagi, N., Kubo, H., and Numa, S. (1989). Structural parts involved in activation and inactivation of the sodium channel. Nature 339, 597–603

46. Nicholson, G. M., Little, M. J., & Birinyi-Strachan, L. C. (2004). Structure and function of δ-atracotoxins: Lethal neurotoxins targeting the voltage-gated sodium channel. Toxicon, 43(5), 587–599. doi.org/10.1016/j.toxicon.2004.02.006

47. Little, M. J., Zappia, C., Gilles, N., Connor, M., Tyler, M. I., Martin-Eauclaire, M. F., … Nicholson, G. M. (1998). δ-Atracotoxins from Australian funnel-web spiders compete with scorpion α-toxin binding but differentially modulate alkaloid toxin activation of voltage-gated sodium channels. Journal of Biological Chemistry, 273(42), 27076–27083. doi.org/10.1074/jbc.273.42.27076

48. Fletcher, J. I., Chapman, B. E., Mackay, J. P., Howden, M. E. H., & King, G. F. (1997). The structure of versutoxin (δ-atracotoxin-Hv1) provides insights into the binding of site 3 neurotoxins to the voltage-gated sodium channel. Structure, 5(11), 1525–1535. doi.org/10.1016/S0969-2126(97)00301-8

49. Bosmans, F., & Tytgat, J. (2007). Voltage-gated sodium channel modulation by scorpion α-toxins. Toxicon, 49(2), 142–158. doi.org/10.1016/j.toxicon.2006.09.023

50. Wanke, E., Zaharenko, A. J., Redaelli, E., & Schiavon, E. (2009). Actions of sea anemone type 1 neurotoxins on voltage-gated sodium channel isoforms. Toxicon, 54(8), 1102–1111. doi.org/10.1016/j.toxicon.2009.04.018

51. genecards.org/cgi-bin/carddisp.pl?gene=SCN1A

52. Duflocq, A., Le Bras, B., Bullier, E., Couraud, F. & Davenne, M. (2008) Nav1.1 is predominantly expressed in nodes of Ranvier and axon initial segments. Mol. Cell Neurosci. 39, 180–192.

53. von Schoubye, N. L., Frederiksen, K., Kristiansen, U., Petersen, A. V., Dalby, N. O., Grunnet, M., … Perrier, J. F. (2018). The sodium channel activator Lu AE98134 normalizes the altered firing properties of fast spiking interneurons in Dlx5/6+/−mice. Neuroscience Letters, 662(October 2017), 29–35. doi.org/10.1016/j.neulet.2017.10.004

54. genecards.org/cgi-bin/carddisp.pl?gene=SCN4A

55. Wang, S-Y., Wang, GK. (1998) Point mutations in segment I-S6 render voltage-gated Na channels resistant to batrachotoxin. *Proc Natl Acad Sci USA* **95**:2653–2658.

56. Kimura, T., Yamaoka, K., Kinoshita, E., Maejima, H., Yuki, T., Yakehiro, M., & Seyama, I. (2001) Novel site on sodium channel -subunit responsible for the differential sensitivity of grayanotoxin in skeletal and cardiac muscle. Mol Pharmacol 60:865–872

57. Cestèle, S., Scheuer, T., Mantegazza, M., Rochat, H., Catterall, W.A., 2001. Neutralization of gating charges in domain II of the sodium channel a subunit enhances voltage sensor trapping by a b-scorpion toxin. J. Gen. Physiol. 118, 291–302.

58. Cestèle, S., Yarov-Yarovoy, V., Qu, Y., Sampieri, F., Scheuer, T., Catterall, W.A., 2006. Structure and function of the voltage sensor of sodium channels probed by a b-scorpion toxin. J. Biol. Chem. 282, 21332–21344

59. Safo P, Rosenbaum T, Shcherbatko A, Choi D-Y, Han E, Toledo-Aral J, Olivera BM, Brehm P, and Mandel G (2000) Distinction among neuronal subtypes of voltage-activated sodium channels by -conotoxin PIIIA. *J Neurosci* **20:**76–80

60. Chandy, KG. & Gutman, GA. (1993) Nomenclature for mammalian potassium chan- nel genes. Trends Pharmacol Sci 14:434

61. Rudy, B., Maffie, J., Amarillo, Y., Clark, B., Goldberg, E. M., Jeong, H. Y., … Zagha, E. (2010). Voltage Gated Potassium Channels: Structure and Function of Kv1 to Kv9 Subfamilies. Encyclopedia of Neuroscience, 7, 397–425. doi.org/10.1016/B978-008045046-9.01630-2

62. In, T., Shaw, T., & Shaker, T. (1999). letters Zn 2 + -binding and molecular determinants of tetramerization in voltage- gated K + channels, 6(1).

63. Roger N. Rosenberg, Juan M. Pascual. Rosenberg's Molecular And Genetic Basis Of Neurological And Psychiatric Disease. 5th Edition (2015). 84. – 986. Elsevier, Ltd..: Waltham, MA. ISBN 978-0-12-410529-4

64. genecards.org/cgi-bin/carddisp.pl?gene=KCNB1

65. Misonou, H., Mohapatra, D. P., & Trimmer, J. S. (2005). Kv2.1: A voltage-gated K+channel critical to dynamic control of neuronal excitability. NeuroToxicology, 26(5), 743–752. doi.org/10.1016/j.neuro.2005.02.003

66. Torkamani, A., Bersell, K., Jorge, B. S., Bjork, R. L., Friedman, J. R., Bloss, C. S., … Kearney, J. A. (2014). De Novo KCNB1 Mutations in Epileptic Encephalopathy, 529–540. doi.org/10.1002/ana.24263

67. Zhang, F., Xu, X., Li, T., & Liu, Z. (2013). Shellfish Toxins Targeting Voltage-Gated Sodium Channels, 4698–4723. doi.org/10.3390/md11124698

68. Kamiyama, D., Sekine, S., Barsi-Rhyne, B., Hu, J., Chen, B., Gilbert, L. A., … Huang, B. (2016). Versatile protein tagging in cells with split fluorescent protein. Nature Communications, 7, 1–9. doi.org/10.1038/ncomms11046

69. Jensen, C. S., Watanabe, S., Stas, J. I., Klaphaak, J., Yamane, A., Schmitt, N., … Misonou, H. (2017). Trafficking of Kv2.1 Channels to the Axon Initial Segment by a Novel Non-Conventional Secretory Pathway. The Journal of Neuroscience, 37(48), 3510–3516. doi.org/10.1523/JNEUROSCI.3510-16.2017

70. Fox, P. D., Loftus, R. J., & Tamkun, M. M. (2013). Regulation of Kv2.1 K+ Conductance by Cell Surface Channel Density. Journal of Neuroscience, 33(3), 1259–1270. doi.org/10.1523/JNEUROSCI.3008-12.2013

71. Trapani, J. G., Andalib, P., Consiglio, J. F., & Korn, S. J. (2006). Control of Single Channel Conductance in the Outer Vestibule of the Kv2.1 Potassium Channel. The Journal of General Physiology, 128(2), 231–246. doi.org/10.1085/jgp.200509465

72. Jensen, C. S., Rasmussen, H. B., & Misonou, H. (2011). Neuronal trafficking of voltage-gated potassium channels. Molecular and Cellular Neuroscience, 48(4), 288–297. doi.org/10.1016/j.mcn.2011.05.007

73. Misonou, H., Mohapatra, D. P., & Trimmer, J. S. (2005). Kv2.1: A voltage-gated K+channel critical to dynamic control of neuronal excitability. NeuroToxicology, 26(5), 743–752. doi.org/10.1016/j.neuro.2005.02.003

74. Gasser, A., Ho, T. S., Cheng, X., Chang, K., Waxman, S. G., Rasband, M. N., & Dib-hajj, S. D. (2012). An AnkyrinG-Binding Motif Is Necessary and Sufficient for Targeting Na v 1 . 6 Sodium Channels to Axon Initial Segments and Nodes of Ranvier, 32(21), 7232–7243. doi.org/10.1523/JNEUROSCI.5434-11.2012

75. plan.core-apps.com/asgct2018/abstract/20763d8c-aad6-4275-bec6-d5e013622d51

76. He, B., & Soderlund, D. M. (2011). Human Embryonic Kidney (HEK293) Cells Express Endogenous Voltage-Gated Sodium Currents and Nav 1.7 Sodium Channels. Neuroscience Letters, 469(2). doi.org/10.1016/j.neulet.2009.12.012.Human

77. Cells, P.-H.-, Pelucchi, B., Aguiari, G., Pignatelli, A., Manzati, E., Witzgall, R., … Belluzzi, O. (2006). Nonspecific Cation Current Associated with Native. doi.org/10.1681/ASN.2004121146

78. Deuis, J. R., Wingerd, J. S., Winter, Z., Durek, T., Dekan, Z., Sousa, S. R., … Vetter, I. (2016). Analgesic effects of GpTx-1, PF-04856264 and CNV1014802 in a mouse model of NaV1.7-Mediated pain. Toxins, 8(3). doi.org/10.3390/toxins8030078

79. Weiss, M. M., Dineen, T. A., Marx, I. E., Altmann, S., Boezio, A., Bregman, H., … Fremeau, R. T. (2017). Sulfonamides as Selective Na. doi.org/10.1021/acs.jmedchem.6b01851

80. Storer, R. I., Pike, A., Swain, N. A., Alexandrou, A. J., Bechle, B. M., Blakemore, D. C., … Warmus, J. S. (2017). Bioorganic & Medicinal Chemistry Letters Highly potent and selective Na V 1 . 7 inhibitors for use as intravenous agents and chemical probes. Bioorganic & Medicinal Chemistry Letters, 27(21), 4805–4811. doi.org/10.1016/j.bmcl.2017.09.056

81. Theile, J. W., Fuller, M. D., & Chapman, M. L. (2016). The selective Na v 1.7 inhibitor , PF-05089771 , interacts equivalently with fast and slow inactivated Na v 1 . 7 channels. doi.org/10.1124/mol.116.105437

82. Friedman, J. I., Temporini, H., & Davis, K. L. (1999). Pharmacologic strategies for augmenting cognitive performance in schizophrenia. Biological Psychiatry, 45(1), 1–16. doi.org/10.1016/S0006-3223(98)00287-X

83. Naheed M, Green B (2001). "Focus on clozapine". Current Medical Research and Opinion. 17 (3): 223–9. doi:10.1185/0300799039117069

84. Shafti, S. S., & Khoei, A. A. (2016). Effectiveness of rivastigmine on positive , negative , and cognitive symptoms of schizophrenia : a double-blind clinical trial, 308–316. doi.org/10.1177/2045125316656334

85. Craig Risch, S & Horner, Michael & Mcgurk, Susan & Palecko, Simmy & Markowitz, John & Nahas, Ziad & Devane, C. (2006). Donepezil effects on mood in patients with schizophrenia and schizoaffective disorder. The international journal of neuropsychopharmacology / official scientific journal of the Collegium Internationale Neuropsychopharmacologicum (CINP). 9. 603-5. 10.1017/S1461145705006115

86. Yohn, S. E., & Conn, P. J. (2017). Positive allosteric modulation of M1and M4muscarinic receptors as potential therapeutic treatments for schizophrenia. Neuropharmacology, 1–11. doi.org/10.1016/j.neuropharm.2017.09.012

87. Dhindsa, R. S., Lowenstein, D. H., & Goldstein, D. B. (2016). Molecular Architecture and Neurobiology of the Epilepsies. Genomics, Circuits, and Pathways in Clinical Neuropsychiatry. Elsevier Inc. doi.org/10.1016/B978-0-12-800105-9.00037-8

88. Feng, S., Sekine, S., Pessino, V., Li, H., Leonetti, M. D., & Huang, B. (2017). Improved split fluorescent proteins for endogenous protein labeling. Nature Communications, 8(1). doi.org/10.1038/s41467-017-00494-8

89. Medsker, B., Forno, E., Simhan, H., Juan, C., & Sciences, R. (2016). HHS Public Access, 70(12), 773–779. doi.org/10.1097/OGX.0000000000000256.Prenatal

90. Vassilev, P. M., Scheuer, T., & Catterall, W. A. (1988). Identification of an intracellular peptide segment involved in sodium channel inactivation. Science, 241(4873), 1658–1661. doi.org/10.1126/science.2458625

91. Yan, Z., Zhou, Q., Wang, L., Wu, J., Zhao, Y., Huang, G., … Yan, N. (2017). Structure of the Nav1.4-β1 Complex from Electric Eel. Cell, 170(3), 470–482.e11. doi.org/10.1016/j.cell.2017.06.039

9. MATERIALS AND METHODS

Genetics

PCR

Two µL of the DNA templates in a stock concentration of 50 ng/µL were mixed in a PCR reaction containing 1.25 µL of 10 pM forward and reverse primers (Eurofins Genomics, Ebersberg, Germany, synthetized according to our choice), 0.5 µL of 100 nM dNTPs, 1 µL of Herculase polymerase, and 10 µL of polymerase buffer (all from Agilent Technologies, Glostrup, Denmark). The thermocycler was programmed for 31 synthesis cycles in a standard PCR; elongation times varied from 30 seconds to 60 or 90 s, depending on the length of the DNA templates. The PCR products were lastly checked by gel electrophoresis.

Restriction digests

Two separate restriction reactions were performed differing on whether the DNA sample was the PCR-amplified insert or the vector. The insert reaction contained 13 µL of the PCR-synthetized DNA, 0,5 µL of 2 different restriction enzymes allowed for double digest, 2 µL of enzyme buffer 10x, 2 µL of 10x purified BSA (all from New England Biolabs, MA, USA), and 2 µL of MilliQ water in a final volume of 20 µL. The vector reaction contained 1 µL of the vector of choice (1 µg/ µL), 0,5 µL of the same enzymes, 2 µL of 10x enzyme buffer and BSA 10x, 1 µL of CIP ligase, and 14 µL of MilliQ water in 20 µL total volume. Digestions were performed at 37ºC for 2 hours with agitation.

Gel electrophoresis

Agarose gels were all prepared at 1% with 1 g of D-agarose (Sigma-Aldrich) per 100 mL of 0,5 x TBE buffer (Panreac), boiled and dissolved completely, after which 4 µL of ethidium bromide were added per 100 mL of gel prepared. Gels were run at 100 V for small- and 90 V for larger-sized DNA, at 400 mA, during 30, 60, 90, or 120 min depending on the DNA's length likewise.

UV visualization and gel purification

Visualization of gels was carried out in an automated Azure c600 UV device (Azure Biosystems, CA, USA) at 365 nm wavelength with automatic exposure. Upon confirmation of the presence of the desired insert and vector DNA bands by size, the gel bands were further visualized under UV light with a manual UV device, and cut with clean scalpels. Purification of the TBE-embedded DNA bands was done employing column purification by Illustra GFX extraction kits (GE Healthcare) and according to the manufacturer's instructions. The purified DNA from the gel slices was retained in the Illustra GFX columns and eluted into 50 µL of TE buffer (10 mM Tris-HCl, 0.1 mM EDTA, buffered at pH 8.0; supplied in the Illustra GFX kit) or into a lower volume (30 µL) if the DNA needed to be concentrated from low-intensity bands observed on the gel.

Ligation

Ligation of both digested inserts and vectors into a construct was carried out with 8 µL of insert DNA and 1 µL of vector DNA, 8 µL of MilliQ H_2O, 2 µL of T4 ligase buffer, and 1 µL of T4 ligase (New England Biolabs), in a final volume of 20 µL. A control reaction mix was alongside prepared without insert DNA

replaced by 16 µL of MilliQ H_2O, and 1 µL of T4 ligase. The ligation reaction was performed at 12ºC overnight (16-20 h) for a maximum efficacy of the ligase activity.

Bacterial transformation

OneShot TOP10 competent cells (DH5α strain, ThermoFisher) were thawed from -79ºC and allocated into 25 µL inoculums for each DNA sample to be transformed (ligated constructs + control vectors without insert), by addition of 7-8 µL of DNA, mixed gently and incubated on ice for 30 minutes. A quick heat shock at 42ºC was applied for 30-45 seconds, and immediately after incubated back on ice for 3 minutes. Up to 300 µL of S.O.C. media (Invitrogen) was added per sample and incubated at 37ºC for 1-2 hours with agitation, until some turbidity was observed. The inoculums were subsequently plated into LB agar plates with ampicillin and incubated overnight (18-20 h) at 37ºC. A successful transformation was achieved if the control plate featured less colonies than the plate with construct, after which several individual colonies containing the construct were picked to inoculate larger culture volumes.

Bacterial cultures

Up to 3 mL of LB media or CircleGrow (MPBiomedicals) were inoculated with each of the selected colonies and incubated overnight at 37ºC with agitation.

If enough cells were harvested after, 1.5 mL of cells from each colony were aliquoted to have its DNA plasmids extracted by Miniprep, to be later checked by agarose gel electrophoresis and sequenced thus guaranteeing the correct insert sequence within the constructs.

If the sequence verifications were already performed, an inoculation of 1 mL of the selected transformant was made into a 100 mL LB or Circlegrow culture media for a Maxiprep extraction, and incubated at 37ºC overnight in a dry rotatory incubator.

DNA extraction by MiniPrep

A Miniprep extraction kit (Qiagen) was employed for the isolation of the construct plasmids of interest from up to 1.5 mL of bacterial transformants. Following the Miniprep kit's instructions, the plasmids were eluted into 50 µL of buffer EB (10 mM Tris-Cl, pH 8.5, supplied by the Qiagen extraction kit) or 30 µL for a concentration of the plasmid DNA.

DNA gel verification

A 2-hour restriction digest of the purified DNA plasmids was performed with the restriction enzymes the constructs were cloned with, prior to an agarose gel electrophoresis of the resulting digested vectors and inserts for each clone, for a verification of the presence of an insert band in the plasmids extracted along with their correct DNA sizes.

DNA sequencing

Upon the visualization of the correctly-sized fragments on an agarose gel, the plasmids containing an insert were sent for bi-directional sequencing (Eurofins Genomics, Ebersberg, Germany) to ensure the fidelity of the plasmid. Sequencing settings included selecting the pair of primers flanking the insert sites on the plasmid for their amplification.

The nucleotide sequences retrieved were analyzed in the CLC Main Workbench 7.6.4. software (Qiagen), where the trimmed insert fragments (.clipped files) were aligned against the insert reference sequence (.fasta sequences downloaded from NCBI), along with a BLAST search for the matching gene encoded by these fragments.

DNA extraction by MaxiPrep

A Maxiprep extraction kit protocol (Macherey-Nagel) was followed for the isolation and concentration of the interest plasmid DNA produced from 100 mL transformant cultures. The small DNA precipitate was resuspended in provided TE-EF buffer (Macherey-Nagel) in a little volume (150-300 µL) prior to the quantification of its concentration (see section below).

DNA quantification

Measurement of the DNA concentration contained in the Maxiprep precipitates was performed using a NanoDrop2000 spectrophotometer (ThermoFisher) by taking 1.5 µL aliquots of DNA. Concentration was adjusted to approximately 1 µg/µL by the addition of further TE-EF buffer (Macherey-Nagel). Blanking was done with said buffer likewise.

qPCR

Cells transfected with expression vectors were cultured for 3 days prior to RNA isolation by a Nucleo Spin RNA Plus kit (Macherey-Nagel). The extracted RNAs were dissolved into a ddH_2O solution for storage or analysis. cDNA was synthesized with the TaqMan® Reverse Transcription Reagent kit (ThermoFisher). A prepared SsoFast Eva Green Supermix (Bio-Rad) was added to the different cDNA samples with their respective primer mixes. Real-time PCR was performed in a Bio Rad CFX96 thermocycler with a standard program of 95ºC for 5 s, 60 ºC for 10 s, repeated for 39 cycles.

Cell cultures

Thawing

Cellular cryovials (NUNC, Roskilde, Denmark) containing 1 mL of cell suspension (500000 cells/mL) in 10% DMSO were snap-thawed from -146ºC or -79ºC to 37ºC, then seeded in either T-75 or T-175 polystyrene flasks (NUNC) with DMEM culture media for 24 hours, after which this culture media was removed and replaced with new DMEM for the elimination of the DMSO present.

Cell lineages employed

Two cellular types were used: a non-modified HEK293 lineage for transient transfections, and a stable $Na_v1.1$ -expressing HEK293 lineage.

Preparation of culture reagents

Manufactured DMEM culture media recipients (Gibco, Gaithersburg, MD, USA), each containing 500 mL (with GlutaMax, sodium pyruvate and 4.5 g/L of glucose), were supplemented with the addition of 10% Fetal Bovine Serum (50 mL) inactivated at 56ºC for 30 minutes, and the addition of 1% of Penicillin+Streptomycin solution (5 mL, 10000 U/mL, from Gibco), under sterile conditions.

Manufactured PBS at 1x concentration (Gibco) without $MgCl_2$ or $CaCl_2$ salts, along with manufactured Trypsin 0.05% solution with EDTA (all from Gibco) needed no further modifications.

Cell harvesting and passages

Cells were cultured in a wet static incubator at 37ºC, supplied with 5% CO_2 and 95% humidity, until an optimal confluence was observed (80% approx.). The culture flasks were brought under aseptic working conditions inside Class II laminar flow cabinets, where their culture media was removed and PBS 1x was added for wash, following its removal. Afterwards, a trypsin solution was added and incubated at 37ºC for 2 minutes (non-modified HEK293 cells) or 5 minutes ($Na_v1.1$-modified HEK cells) until a complete cell detachment. Further fresh culture media was added to inactivate the trypsin's activity and the cells were thoroughly resuspended prior to use or seeding into new vessels containing culture media. Volumes for each reagent depending on the vessel's size are provided in the table below.

Type of Vessels	Culture Area (cm^2)	Working Medium (mL)	Confluence to split	Volume of PBS (mL)	Volume of Trypsin (mL)	Volume of media inhibition (mL)
Nunclon Flask T-25	25	5	70-80%	4	0.5	4.5
Nunclon Flask T-75	75	12	70-80%	7	1	3
Nunclon Flask T-175	175	25	70-80%	10	4	6
Falcon Dish 35x10mm	9.6	2	-	-	-	-
96 well Plate	0.32	0.1	-	-	-	-
6 well Plate	9.4	2	-	-	0.2	0.3

Preparation of cells for transfection

Transfections were performed in either 96-well µ-clear plates with flat bottom (Greiner Bio-One, Kremsmüner, Germany) for visualization of expression and imaging at 10x-40x, and 96-well CellCarrier (Perkin Elmer) for imaging at 100x. 6-well plates Delta surface (NUNC) for further electrophysiological experiments of the transfected cells. Cell density ranged from 3K to 30K/well for 96-well plates with 100 µL/well of culture medium, and 150K to 300K/well for 6-well plates in 2 mL/well of medium.

An optional Poly-L-Lysine (PLL) coating of the previous plates was performed with respectively 100 µL or 2 mL of PLL solution, and incubated at 37ºC for 2 hours. The PLL was removed and the plates washed 3 times with similar volumes of PBS 1x, and used immediately for cell seeding.

Seeded cells were incubated for 24 hours at 37ºC, 5% CO_2 and 95% humidity prior to transfection.

Transfections

The transfection method employed in these experiments used Lipofectamine 2000 (L2000) (Invitrogen). For a 96-well plate, a mix of 200 ng of DNA (either a single or multiple types of plasmid expression vectors) plus 0.3 µL of L2000 into 100 µL of OptiMem (Gibco) was added to each well. For a 6-well plate, mixes of up to 3 µg of DNA in total, and 12 µL of L2000 into 300 µL of OptiMem were used per well. Culture media was removed from the cells and further OptiMem was added to the wells. The plates were incubated for 5 hours at 37ºC, 5% CO_2 and 95% humidity. OptiMem was finally removed with the

addition of fresh DMEM and subsequent incubation for 24, 48 or 72 hours for cell expression and their use in microscopy or electrophysiology experiments.

Fixation and antibody staining

Live cells were washed with 100 µL of PBS (Gibco) and fixed with 100 µL paraformaldehyde at 4% for 15 minutes at RT, after which were washed 3 times with 200 µL of PBS. A simultaneous permeabilization and blocking was done with a 2% BSA + 0.1% Triton X-100 solution in PBS ("blocking buffer") for 30 minutes. For primary incubation, 50 µL of 1:500 rabbit α-GFP (Sigma-Aldrich) and 50 µL of 1:1000 mouse α-FLAG (Sigma-Aldrich) antibodies were added for 1 hour. Following 3 PBS washes with 200 µL, the secondary incubation was carried with 50 µL of 1:1000 α-rabbit Alexa 488 and 1:1000 α-mouse Alexa 568 antibodies, along with a 1:300 dilution of Hoechst reagent in blocking buffer, for 1 hour. Wells were washed 4 times with 200 µL PBS prior to the addition of 25 of mounting medium for imaging.

The Hoechst 33342 reagent was employed for a nuclear DNA stain of fixed cells as a positive control. DNA-bound Hoechst could be observed in the blue channel with a λ = 350 nm excitation and λ = 461 nm emission.

Preparation of cells for electrophysiology

Glass coverslips of 5 x 0.1 mm, treated with detergent + 0.1 M HCl and into sterile MilliQ water, were placed over the polystyrene surface of either 6-well plates or 35x10 mm Petri dishes for cell seeding prior to electrophysiological recordings. A short 3-minute microwaving served for the attachment of the coverslips to the surface, after which the cells to be utilized for patch-clamping were trypsinized and seeded over the coverslipped plates.

Electrophysiology

Pipettes and buffers

Glass pipettes with a resistance range between 1.5-2.0 MΩ were produced from 50x1 mm glass tubes in a Universal-Electrode-Puller (Zeitz Instruments) at P10 program (400ºC, 45 s, , resulting in a 2 µM wide pipette tip. Pipettes were filled with Na^+ intracellular solution containing 10 mM NaCl, 140 mM CsF, 10 mM HEPES, 1 mM EGTA, and adjusted to pH = 7.3 with CsOH/HCl. The K^+ intracellular solution for the K_v2.1-transfected cells was prepared with 140 mM KCl, 1 mM MgCl2, 0.1 mM CaCl2, 10 mM HEPES, 1 mM ATP-Na^+ salt, 2 mM EGTA and adjusted to pH = 7.2. The extracellular solution used for both Na_v- and K_v-transfected cells was a Na^+ buffer containing 150 mM NaCl, 3 mM KCl, 1 mM MgCl2, 1 mM CaCl2, 10 mM HEPES and adjusted to pH = 7.3 with NaOH/HCl.

Microscopy observation

Cells were observed under an optical Olympus IX70 inverted microscope under 4x and 10x for positioning of the pipette and under 40x for patching. A LED light source (CoolLED pE300) at 450 nm was used when working with eGFP- and sfGFP-transfected cells.

Activator and inhibitor solutions

Solutions at 30, 10, 3, 1, and 0.3 µM AA43279 were prepared from a stock solution of at 30 mM in DMSO. An equal volume of DMSO instead of extracellular buffer was added in some experiments. A 100 nM solution of TTX was prepared from a TTX stock at 100 µM in water.

Patch-clamp settings

A whole-cell, voltage-clamp procedure was utilized for electrophysiological recordings of ion currents. A holding voltage potential of -80 mV was maintained for all experiments. Pipettes filled with intracellular solution were applied positive pressure before immersion into the extracellular solution bath. Upon contact of the pipette with the cell's membrane's surface, an increase of 0.3-0.5 MΩ was allowed by further lowering the pipette prior to applying negative pressure. Gigaseals were formed with a minimum of 1.6 GΩ, and further suction was applied to break the membrane into a whole-cell configuration.

Voltage-clamp procedure

Step protocols for a full depolarization of the cell's ion channels were automatically applied every 20 s. From a holding potential (V_h) of -80 mV, a hyperpolarizing step was applied at -120 mV for 20 ms, following by a depolarization to -10 mV for 20 ms, and holding at -80 mV for the time left. Another single protocol of 18 continuous sweeps (IV protocol) was applied manually, consisting of a 20 ms hyperpolarization at -120 mV, a variable sweep of 500 ms from -120 mV to +50 mV with Δ +10 mV difference each sweep, a 20 ms step to -10 mV, and a holding at -80 mV for the time left. V_h in between protocols was maintained at -80 mV.

Microscopy

Optical microscopy

Inverted optical microscopes (Olympus CK30) were used at a magnification of 10x for the confluence counting of cellular cultures, and a magnification of 40x for the morphological determination of physiological issues in flasks, plates and Petri dishes.

Spinning disk confocal microscopy

High resolution cell pictures were taken with a confocal fluorescent, spinning disk type Hamamatsu microscope coupled with an X-Cite 120Q excitation light source, and a series of 405 and 488 nm emission lasers. A 40x air objective and a 100x immersion oil objective were used for imaging.

Fluorescence microscopy

Epifluorescence microscopy

An inverted optical microscope (Olympus CKX41) coupled to a 405 nm emission laser (Olympus U-RFLT50) was used for a rapid observation of the expression of reporter genes in transfected cell cultures at 10x or 20x magnification.

Confocal fluorescence microscopy

A Zeiss Axio confocal microscope coupled with an X-Cite 120Q excitation light source was employed for observation and imaging. Pictures were taken with 10x and 40x air objectives. A set of 405 and 488 nm emission lasers were used for fluorescence visualizations.

Software

Electrophysiology

A Commander software for the Multi700B Amplifier device was initialized until a correct communication was established between the computer, digitizer and amplifier devices implicated. Measurement of currents and application of protocols were performed with the Clampex 10.6 software. Results were analyzed with the Clampfit 10.6 software.

Data representation

Averaged data values with ±SD values were represented and plotted using the GraphPad Prism 7.0.4 software unless specified otherwise.

Bioinformatics

A CLC Main Workbench 7.6.4 software (Qiagen) was used for the *in silico* cloning, design of primers and sequences, and representation of figures.

Molecular modeling

Homology models were created with the MOE software (Chemical Computing Group) and molecular visualization and representations were performed with PyMOL 2.2.0 (Schrodinger Inc.).